NASA Technical Memorandum 80057

NASA-TM-80057 19790021976

FOR REFERENCE

Flow Visualization Studies of a General Research Fighter Model Employing a Strake-Wing Concept at Subsonic Speeds

James M. Luckring

AUGUST 1979

NASA

NF00547

1 Report No NASA TM-80057	2 Government Accession No	3 Recipient's Catalog No
4 Title and Subtitle FLOW VISUALIZATION STUDIES OF A GENERAL RESEARCH FIGHTER MODEL EMPLOYING A STRAKE-WING CONCEPT AT SUBSONIC SPEEDS		5 Report Date August 1979
		6 Performing Organization Code
7 Author(s) James M. Luckring		8 Performing Organization Report No L-12673
9 Performing Organization Name and Address NASA Langley Research Center Hampton, VA 23665		10 Work Unit No 505-06-53-01
		11 Contract or Grant No
12 Sponsoring Agency Name and Address National Aeronautics and Space Administration Washington, DC 20546		13 Type of Report and Period Covered Technical Memorandum
		14 Sponsoring Agency Code

15 Supplementary Notes

16 Abstract

A systematic wind-tunnel study was conducted in the Langley high-speed 7- by 10-foot tunnel to document, by oil-flow photographs, the surface flow patterns for configurations incorporating strake-wing geometries indicative of current and proposed maneuvering aircraft. The configurations employed combinations of strakes with reflexed planforms having exposed spans of 10 percent, 20 percent, and 30 percent of the reference wing span and wings with trapezoidal planforms having leading-edge sweep angles of approximately 30°, 44°, and 60°. Tests were conducted at Mach numbers of 0.3 and 0.5 and at angles of attack ranging from approximately 5° to 30° in 5° increments at 0° sideslip. The configurations incorporating the strake-wing geometries exhibited more organized flow patterns with smaller asymmetries to higher angles of attack than the corresponding configurations incorporating the wing-alone geometries did.

17 Key Words (Suggested by Author(s)) Flow visualization Strake-wing Strakes Subsonic speeds Vortex flow Vortices Vortex breakdown Condensation	18 Distribution Statement Unclassified - Unlimited Subject Category 02

19 Security Classif (of this report) Unclassified	20 Security Classif (of this page) Unclassified	21 No of Pages 90	22 Price* $6.00

NASA Technical Memorandum 80057

Flow Visualization Studies of a General Research Fighter Model Employing a Strake-Wing Concept at Subsonic Speeds

James M. Luckring
Langley Research Center
Hampton, Virginia

SUMMARY

A systematic wind-tunnel study was conducted in the Langley high-speed
7- by 10-foot tunnel to document, by oil-flow photographs, the surface flow
patterns for configurations incorporating strake-wing geometries indicative of
current and proposed maneuvering aircraft. The configurations employed combi-
nations of strakes with reflexed planforms having exposed spans of 10 percent,
20 percent, and 30 percent of the reference wing span and wings with trapezoi-
dal planforms having leading-edge sweep angles of approximately 30°, 44°, and
60°. Tests were conducted at Mach numbers of 0.3 and 0.5 and at angles of
attack ranging from approximately 5° to 30° in 5° increments at 0° sideslip.
The configurations incorporating the strake-wing geometries exhibited more
organized flow patterns with smaller asymmetries to higher angles of attack
than the corresponding configurations incorporating the wing-alone geometries
did. The improved flow patterns of the strake-wing geometries were primarily
caused by the separation-induced vortex flow which was generated by the strake
and persisted over the wing.

For a fixed wing-sweep angle, an increase in strake span increased the
extent of spanwise primary vortex flow over the wing and decreased the length
of the fuselage over which body vortices were evidenced. For the 60° wing
configurations, an increase in strake span also resulted in a decrease in the
extent of secondary vortex flow over the wing. As wing sweep was increased,
the wing primary vortex was strengthened, and the angle of attack where the
strake and wing primary vortices were no longer individually distinguishable
on the wing decreased.

Naturally occurring condensation effects in the vicinity of an angle of
attack of 20° allowed the strake primary vortex cores to be observed up to
their bursting points for the configurations incorporating the large strake and
either the 30° or 44° wing. Although the surface oil-flow patterns changed as
the strake primary vortex bursting point moved from a position aft of the wing
trailing edge to the strake apex, no conclusive evidence in the surface oil
flow of the burst vortex was observed.

Though not photographically recorded in this report, both the strake and
wing unburst primary vortex cores were observed as a result of condensation.
However, at the angles of attack for which this observation was made, only one
vortex was evidenced by the surface oil flows on the wing. This suggests that
the wing primary vortex had not coalesced with the strake primary vortex at
these angles of attack, but had merely been displaced away from the wing upper
surface by the strake vortex; thus, the strake vortex was allowed to dominate
the surface flow pattern.

INTRODUCTION

The strake-wing concept has been incorporated in the designs of several current maneuvering aircraft as a means of improving their high-angle-of-attack maneuver aerodynamics. The enhanced maneuverability is primarily a result of the formation of strong vortices along the leading and side edges of the strake. In addition to producing large vortex lift increments on the strake itself, these vortices persist over the wing and provide induced effects throughout the wing flow field which can be favorable by resulting in additional lift increments. However, the persistence of the strake vortex over the wing as well as the relative proximity of the wing and strake results in a very complex flow field where the wing aerodynamics and the strake aerodynamics interact strongly and where multiple regions of separation-induced vortex flow occur. Because of the complex nature of this type of flow as well as the comparatively recent interest in strake-wing geometries, very little parametric information is available on this topic for use in future advanced configuration studies. To this end, a parametric wind-tunnel study was conducted to build a data base for both longitudinal (ref. 1) and lateral-directional (ref. 2) aerodynamic characteristics of strake-wing configurations. To complement this parametric study, the present study was conducted to document, by means of oil-flow photographs, the surface flow patterns of selected configurations from references 1 and 2. The configurations chosen for the present study incorporated reflexed strakes having exposed spans of 10 percent, 20 percent, and 30 percent of the reference wing span and trapezoidal wing planforms having leading-edge sweep angles of approximately 30°, 44°, and 60°. The tests were conducted in the Langley high-speed 7- by 10-foot tunnel at Mach numbers of 0.3 and 0.5. The angle of attack ranged from 5° to 30° in 5° increments at 0° sideslip.

SYMBOLS

The International System of Units, with the U.S. Customary Units presented in parentheses, is used for the physical quantities found in this report (ref. 3). Measurements were made in U.S. Customary Units.

A	aspect ratio
b	span, cm (in.)
$\bar{c}$	wing reference chord, 23.327 cm (9.184 in.)
c_r	root chord
c_t	tip chord
M_∞	free-stream reference Mach number
r	radius of curvature, cm (in.)
S	area, cm^2 (in^2)
x	chordwise distance, cm (in.) (see fig. 1(b))

y	spanwise distance, cm (in.) (see fig. 1(b))
α	angle of attack, deg
λ	taper ratio, c_t/c_r
Λ	leading-edge sweep angle, deg

Subscripts:

max	maximum
ref	reference
s	strake
t	tail
te	trailing edge
w	wing

MODEL DESCRIPTION

A three-view drawing of the general research model is presented in figure 1(a). This model was originally designed so that various wing and canard planforms could be tested and it has been used for a variety of parametric studies (refs. 4 to 6). Because of a slight blunting of the nose, the model forebody was 0.127 cm (0.050 in.) shorter for the present study than it had been for previous studies. (See fig. 1(a).) Figure 1(b) presents the exposed strake planforms and figure 1(c) presents the exposed wing planforms. Figure 2 presents the model mounted in the Langley high-speed 7- by 10-foot tunnel. Pertinent geometric characteristics associated with this model are presented in tables I to IV.

Three different wings were tested. The wings, referred to as 1, 2, and 3, had leading-edge sweep angles Λ_w of approximately 30°, 44°, and 60°, respectively. (The more exact sweep angles can be found in table I.) All wings had the same area, span, and mean geometric chord. The wings had untwisted trapezoidal planforms with uncambered circular-arc airfoil sections which varied linearly in maximum thickness from 6 percent of the chord at the wing-fuselage juncture to 4 percent of the chord at the tip. The wings were mounted longitudinally so that the quarter-chord point of the wing chord at the wing-fuselage juncture coincided for all wings.

Three different strakes were tested. The strakes, referred to as 1, 2, and 3, had maximum exposed semispans in cm (in.) of 2.54 (1.00), 5.08 (2.00), and 7.62 (3.00), respectively. All strakes had the same root chord (at the strake-fuselage juncture) and had spanwise ordinates which were identical in percent maximum semispan. (See table II.) The strakes initially had a trailing-edge sweep angle equal to the greatest wing leading-edge sweep angle.

3

For all wings, the strakes were mounted longitudinally so that the trailing edge of the strake was approximately 0.051 cm (0.020 in.) from the leading edge of the wing. This gap between the strake and the wing (as well as between the forebody and afterbody) was necessitated by the dual-balance test technique of references 1 and 2 and was repeated for the present investigation. (See section "Apparatus and Tests".) To accommodate the wings having the lower sweep angles, a portion of the strake near the trailing edge was removed so that the strake trailing-edge sweep angle matched the wing leading-edge sweep angle. (These cuts are shown as the dashed lines in fig. 1(b).) Table III presents the coordinates of the intersection point of the strake leading and trailing edges, and table IV presents the exposed strake area in percent wing reference area for each strake and each value of trailing-edge sweep. The strakes were flat plates which, in accordance with the purposes of this study, had sharply beveled leading and side edges to assure the strong formation of the separation-induced vortex flows.

The vertical tail had a trapezoidal planform with symmetric circular-arc airfoil sections which varied linearly in maximum thickness from 6 percent of the chord at the tail-fuselage juncture to 4 percent of the chord at the tip.

In the discussion of the results of this study, the wings are referred to by the approximate sweep angles, and the various model configurations are identified by the approximate wing sweep and strake number. For example, the configuration incorporating the 30° wing with the large strake is configuration 30-3, and the configuration with the same wing but with the strake off is configuration 30-0.

APPARATUS AND TESTS

This investigation was conducted in the Langley high-speed 7- by 10-foot tunnel. (See refs. 7 and 8.) The surface oil-flow patterns were established by coating the model with a mixture of 90-weight oil and fluorescent powder which radiated light in the yellow-green portion of the spectrum. The flow patterns were illuminated with an ultraviolet strobe lighting system and were photographically recorded with a camera filtered to highlight the visibly radiating portion of the spectrum.

Because of the dual-balance test technique of references 1 and 2, a small metric break was maintained between the fuselage segments, between the strake and the wing, and between the strake and the afterbody. The bleed flow through this gap was found in reference 1 to have no measurable effect on the aerodynamic forces and moments for the configurations incorporating the 60° wing. However, subsequent tests for the configurations incorporating the 50° wing indicated that the bleed flow was precipitating breakdown of the strake vortex over the wing. As a consequence, all force tests of reference 1 for configurations incorporating wings with sweep angles of 50° or less were conducted with noninterfering wiper seals which blocked the bleed flow to assure proper vortex-breakdown characteristics. Accordingly, the surface flow visualization studies were conducted with the strake-wing gap sealed for configurations incorporating either the 30° or 44° wings and with the strake-wing gap unsealed for the configurations incorporating the 60° wing. Additional studies were conducted for

4

the configurations incorporating the 44° wing with the gap unsealed to determine the extent to which the gap bleed flow might affect the surface flow patterns. The gap between the two fuselage segments was sealed for all surface oil-flow studies to prevent oil from entering the forward balance chamber.

Tests were conducted at free-stream Mach numbers of 0.3 and 0.5 which correspond to free-stream Reynolds numbers of 1.3×10^6 and 2.1×10^6 based on the mean geometric chord of 23.327 cm (9.184 in.). The model was tested at angles of attack which ranged from approximately 5° to 30° in 5° increments at a sideslip angle of 0°. All tests were conducted with boundary-layer transition fixed on the model by means of strips of No. 120 carborundum grit which were 0.16 cm (0.063 in.) wide. They were situated in the streamwise direction 2.54 cm (1.00 in.) aft of the leading edge of the wing and vertical tail as well as 2.54 cm (1.00 in.) aft of the nose of the fuselage as outlined in reference 9. Transition strips of the same grit and width were situated on the strakes at a distance 0.76 cm (0.30 in.) normal to the leading edge. This position corresponded to the intersection of the leading-edge bevel with the upper or lower surface.

PRESENTATION OF RESULTS

The general characteristics of the surface flow patterns are presented in figures 3 and 4. Surface flow patterns for the present configurations are presented in figures 5 to 16. An outline of the contents of these figures follows:

Λ_w, deg	Strake	α_{max}, deg	M_∞	Wing-strake gap	Figure
30	Off	30	0.3		5
30	1	30	.3	Sealed	6
30	2	30	.3	Sealed	7
30	3	30	.3	Sealed	8
44	Off	30	.3		9
44	3	30	.3	Sealed	10
44	3	30	.3	Open	11
60	Off	30	.3		12
60	1	20	.3	Open	13
60	2	25	.3	Open	14
60	3	20	.3	Open	15
60	1	20	.5	Open	16

DISCUSSION OF RESULTS

Figures 3 and 4 present representative oil-flow photographs with accompanying sketches (configurations 60-3 and 60-0, $\alpha = 10°$) and serve to identify the major regions of interest and basic effects in these and subsequent photographs. The wing primary and secondary vortices are clearly evidenced for the configuration without the strake, and the region of attached flow aft of the primary vortex can also be seen (fig. 3(a)). The corresponding flow sketch

5

(fig. 3(b)) illustrates the wing primary and secondary vortices and identifies, in the cross-sectional view, points along the primary separation line, primary reattachment line, and secondary separation line. For the configuration with the strake (fig. 4(a)), the strake primary vortex is seen to persist over the wing while the strake secondary vortex is not visibly discernible over the wing. The wing primary and secondary vortices are still evidenced for this configuration although the origin of the wing vortex systems, as would be expected, has been displaced from the wing apex to the juncture of the strake and wing leading edges. The corresponding flow sketch (fig. 4(b)) illustrates the strake and wing vortices and identifies, in the cross-sectional views, points along the various separation and reattachment lines. Details of the flow patterns pertinent to the particular geometry of figures 3 and 4 are discussed subsequently.

30° Wing Configurations

Surface oil-flow patterns for configuration 30-0 (wing 1 with no strake) are presented in figure 5. At an angle of attack of 5°, a small leading-edge vortex is evidenced. At an angle of attack of 10°, the wing appears to have begun to stall near the tips. By 15° angle of attack (fig. 5(c)), the wing flow is quite disorganized. It is of interest to note in figure 5(c) that a symmetric pair of body vortices have formed in the vicinity of the fuselage center line ahead of the wing leading edge. They are evidenced by the regions of spanwise turning flow along the top of the fuselage. These regions are distinctly bounded by secondary separation lines which terminate aft of the wing leading edge. At this angle of attack as well as the higher angles of attack (figs. 5(d) to 5(f)), the body vortices became asymmetric as they persisted over the fuselage aft of the wing leading edge. For this configuration the asymmetry of the body vortices resulted in additional spanwise flow increments on the right semispan at the higher angles of attack. The surface oil-flow patterns for configuration 30-0 did not indicate any secondary vortex effects.

The surface oil-flow patterns for configurations 30-1, 30-2, and 30-3 are presented in figures 6, 7, and 8, respectively. In general, the strake-wing geometries for the 30° wing exhibit organized flow patterns with smaller asymmetries to much higher angles of attack than were shown for the wing-alone geometry. (Compare, for example, figs. 6(f), 7(f), and 8(f) with fig. 5(f)). The enhanced flow patterns of the strake-wing geometries result primarily from the persistence of the strake vortex over the wing. Up to an angle of attack of 15° the strake vortex is individually distinguishable on the wing from the wing vortex. At the higher angles of attack, the surface oil-flow patterns fail to evidence the individual vortex systems. Comparing the three strake-wing geometries at the higher angles of attack demonstrates that an increase in strake span promoted larger regions of spanwise flow over the wing and decreased the extent of the fuselage over which the body vortices were evidenced. (The lines of secondary separation for the body vortices terminate at more forward locations with increasing strake span.) Both of these effects are related to the increase in the size of the strake vortex which occurred as the strake span was increased. Additional consideration should be given to the change in strake vortex strength which occurs with increasing strake span although this change is beyond the scope of the present investigation. It is

6

of interest to note that at angles of attack of 20° and 25°, the vortex cores for the large strake are observable as dark bands which curve outboard over the wing. (See figs. 8(d) and 8(e).) The cores were observable up to their bursting point as a result of naturally occurring condensation effects which did not take place much below an angle of attack of 20°. Only one core is visible at an angle of attack of 25° (fig. 8(e)) because the right strake vortex bursting point had moved essentially to the apex of the strake. A comparison of the surface oil-flow patterns on the right and left semispans for figure 8(e) shows no conclusive evidence of the burst vortex although the flow patterns indicate a more diffuse effect of the shed vorticity distribution on the right semispan.

Secondary vortex effects were not distinctly evidenced on the 30° wing in the presence of the various strakes. However, a high shear region can be seen on the wing where the secondary vortex would be expected to form. This region is situated near the strake-wing juncture and appears as a dark band between the leading edge and the secondary separation line of the wing. It is most observable over angles of attack ranging from 10° to 25° for configuration 30-1 and over angles of attack ranging from 10° to 15° for configurations 30-2 and 30-3. The angle-of-attack range over which this shear region was strongly evidenced decreased as strake span increased. Although these effects could be related to secondary vortices, the lack of surface flow detail prohibits such a conclusion.

Secondary vortices were evidenced on strakes 2 and 3 for all test angles of attack above 5°. The secondary vortices remained in the vicinity of the strake leading-edge bevel. Little evidence of the secondary vortex for strake 1 was observed up to an angle of attack of 30°. However, at an angle of attack of 30° (fig. 8(f)), the inboard turning streak lines on the small strake suggest that the strake surface oil flow is being dominated by counterrotating flow and that the strake primary vortex has been vertically displaced where it acts more on the side of the fuselage than on the strake itself. It is possible in this instance that secondary separation is occurring on the side of the fuselage.

44° Wing Configurations

Surface oil-flow patterns for configuration 44-0 are presented in figure 9. As would be expected, this more highly swept wing promoted a stronger vortex system which postponed the onset of stall characteristics to a higher angle than was encountered by configuration 30-0. Disorganized asymmetric flow was not evidenced to any great extent until the angle of attack reached approximately 25° (fig. 9(e)). As was the case for configuration 30-0, the flow patterns for configuration 44-0 showed substantial asymmetries at an angle of attack of 30° (fig. 9(f)) with the asymmetry in the body vortices resulting in additional spanwise flow increments on the right semispan. There was no evidence of the wing secondary vortex.

Surface oil-flow patterns for configuration 44-3 are presented in figure 10. In general, the effect of adding the large strake to this wing was comparable to the effect of adding this strake to the 30° wing; organized flow patterns with smaller asymmetries were exhibited to higher angles of attack by the strake-wing configuration compared to the wing-alone configuration.

(Compare, for example, the differences between flow patterns in figs. 9(f) and 10(f) with the differences between flow patterns in figs. 5(f) and 8(f).) Up to an angle of attack of 15°, the strake vortex is individually distinguishable on the wing from the wing vortex. (See figs. 10(a), 10(b), and 10(c).) However, the evidence of the two vortices is weaker at an angle of attack of 15° for configuration 44-3 than it was for configuration 30-3. As had occurred for configuration 30-3, the core of the strake vortex is made visible as a result of naturally occurring condensation effects at angles of attack of 20° and 25° for configuration 44-3 (figs. 10(d) and 10(e)). The surface flow patterns at these angles of attack once again failed to evidence individually both strake and wing vortices. Although these flow patterns might be interpreted as an implication that the two vortex systems had coalesced into one, additional observations of the unburst strake and wing vortex cores at these angles of attack suggest that the wing vortex had not coalesced with the strake vortex, but had merely been displaced away from the wing upper surface by the strake vortex, thus allowing the strake vortex to dominate the surface flow patterns.

Secondary vortex effects were not distinctly evidenced on the wing for configuration 44-3. However, a region of high shear was evidenced on the wing where the secondary vortex would be expected to form. As had been the case for configuration 30-3, this wing shear region was most observable at angles of attack of 10° and 15° (figs. 10(b) and 10(c)). The strake secondary vortex was evidenced in the vicinity of the strake leading-edge bevel over the angle-of-attack range of the investigation.

Surface oil-flow patterns are presented in figure 11 for configuration 44-3 with the strake-wing gap open. A comparison of figures 10 and 11 at corresponding angles of attack shows that there is little effect of unsealing the gap on the surface oil-flow patterns at this sweep angle.

60° Wing Configurations

Surface oil-flow patterns for configuration 60-0 are presented in figure 12. As would be expected, the larger sweep angle of this wing promoted a stronger wing primary vortex system than for wing-alone configurations 30-0 and 44-0. The disorganized asymmetric flow developed by configurations 30-0 and 44-0 did not occur for configuration 60-0 to any great extent over the test angle-of-attack range. The body vortices remained situated in the vicinity of the fuselage center line and showed only slight asymmetry at $\alpha = 30°$. In addition to the strong primary leading-edge vortex, configuration 60-0 exhibited a strong wing secondary vortex at angles of attack between 10° and 25°.

At an angle of attack of 5° (fig. 12(a)) there is slight evidence of a multiple, corotating leading-edge vortex system. The probable cause of this flow pattern for the sharp-edged wings of the present study is small irregularities in the leading edge. These irregularities, if small, could cause the leading-edge vortex to break into multiple vortices at low angles of attack where the shed vorticity is small. The small irregularities would be passive to the leading-edge vortex at high angles of attack where the shed vorticity has increased considerably. It should be recognized that for sufficiently swept wings with relatively blunt leading edges, this type of flow pattern is

not uncommon. The flow can still separate directly from the blunt leading edge in the form of a rolled-up vortex as a result of the spanwise variation of the upwash field. Moreover, if the flow should remain attached around the blunt leading edge, Squire, Jones, and Stanbrook (ref. 10) have observed that multiple streamwise vortices may occur due to a transverse boundary-layer shear associated with streamline curvature. However, the forced separation which results from the sharp leading edge tends to preclude these explanations which are based on partial flow attachment around the edge.

The surface oil-flow patterns for configurations 60-1, 60-2, and 60-3 are presented in figures 13, 14, and 15, respectively. The darkened forebody and wing apex region in figure 14 was probably caused by the misfiring of a portion of the lighting system used to illuminate the model. The previously observed strake effect at high angles of attack (organized flow patterns with smaller asymmetries to higher angles of attack for strake on compared to strake off) is not as evident for the present strake-wing configurations because the isolated 60° wing exhibited organized vortex flow patterns throughout the angle-of-attack range of the investigation. Up to an angle of attack of 10° (figs. 13(b), 14(b), and 15(b)), the strake and wing primary vortices are individually distinguishable on the wing, but at the higher angle of attack the surface oil-flow patterns fail to evidence the individual vortex systems. Therefore, as the wing sweep was increased, the angle of attack at which the surface oil flow failed to evidence the separate vortex systems on the wing decreased. Comparing the three strake-wing geometries at the higher angles of attack demonstrates that, as was the case for the strake-wing configurations incorporating the 30° wing, an increase in strake span promoted larger regions of spanwise flow over the wing and decreased the extent of the fuselage over which the body vortices were evidenced. No naturally occurring condensation effects were observed for configurations incorporating the 60° wing. Because the condensation was related to the tunnel ambient conditions, no conclusions can be drawn concerning the occurrence or lack of occurrence of this effect.

Stronger secondary vortex effects were evidenced for the strake-wing configurations incorporating the 60° wing than were evidenced for the previous strake-wing configurations. At an angle of attack of 10°, the wing secondary vortex is clearly evidenced for all three strake-wing geometries. (See figs. 13(b), 14(b), and 15(b).) However, it is curious to note that for all three configurations an additional separation line can be observed at this angle of attack between the wing primary and secondary vortices, and that a small region of apparently spanwise flow is evidenced between the two separation lines. For comparison, observe that a single oil ridge occurs between the wing primary and secondary vortices of the corresponding strake-off configuration (60-0) at an angle of attack of 10° (fig. 12(b)). This single oil ridge is caused by secondary separation and usually corresponds to the converging flows of the primary and secondary vortices. (See sketch (a).) The ridge is commonly observed on sharp-edged wings of sufficient sweep angle. (See refs. 11, 12, and 13.)

For the dual-ridge flow patterns observed for the strake-on configurations, the inner ridge still corresponds to the separation of the boundary layer which is generated by the primary vortex (i.e., secondary separation), while the outer ridge corresponds to the separation of the boundary layer which

9

is generated by the secondary vortex. (See sketch (b).) Although it would appear that the addition of the strake modified the relationship between the wing primary and secondary vortices in such a fashion as to result in the dual separation lines, insufficient information was generated during this study to isolate the mechanism involved.

Wing vortices   Wing vortices

Strake off   Strake on

Sketch (a)   Sketch (b)
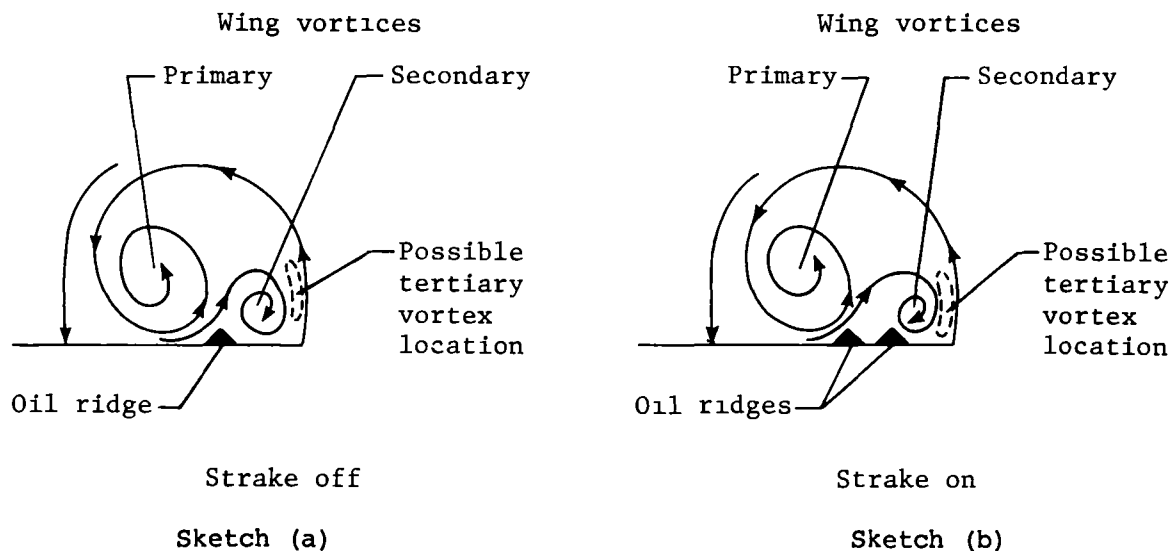
It is of additional interest to note that in figure 13(b) a region of flow roughly parallel to the wing leading edge is evidenced between the wing secondary vortex and the leading edge. Although a tertiary vortex could be expected to form in this region, the surface flow patterns fail to evidence a sufficiently helical pattern to substantiate its presence. At the higher angles of attack, the secondary vortex effects were strongly evidenced for the configuration 60-1, but were less evidenced for the configurations incorporating the larger strakes. The angle-of-attack range over which the wing secondary vortex was strongly evidenced decreased as strake span increased. Once again the secondary vortices for the various strakes tended to remain in the vicinity of the strake leading-edge bevel.

Surface flow patterns for configuration 60-1 are presented in figure 16 for a free-stream Mach number of 0.5. A comparison of figures 13 and 16 at corresponding angles of attack demonstrates that there is very little effect of the increased Mach number on the surface flow patterns.

SUMMARY OF RESULTS

A systematic wind-tunnel study was conducted in the Langley high-speed 7- by 10-foot tunnel to document by oil-flow photographs the surface flow patterns of configurations incorporating strake-wing geometries indicative of current and proposed maneuvering aircraft. The configurations employed combinations of strakes with reflexed planforms having exposed spans of 10 percent, 20 percent, and 30 percent of the reference wing span and wings with trapezoidal planforms

10

having leading-edge sweep angles of approximately 30°, 44°, and 60°. Tests were conducted at Mach numbers of 0.3 and 0.5 and at angles of attack ranging from approximately 5° to 30° in 5° increments at 0° sideslip. The configurations incorporating the strake-wing geometries exhibited more organized flow patterns with smaller asymmetries to higher angles of attack than the corresponding configurations incorporating the wing-alone geometries did. The improved flow patterns of the strake-wing geometries were primarily caused by the separation-induced vortex flow which was generated by the strake and persisted over the wing.

For a fixed wing-sweep angle, an increase in strake span increased the extent of spanwise primary vortex flow over the wing and decreased the length of the fuselage over which body vortices were evidenced. For the 60° wing configurations, an increase in strake span also resulted in a decrease in the extent of secondary vortex flow over the wing. As wing sweep was increased, the wing primary vortex was strengthened, and the angle of attack where the strake and wing primary vortices were no longer individually distinguishable on the wing decreased.

Naturally occurring condensation effects in the vicinity of an angle of attack of 20° allowed the strake primary vortex cores to be observed up to their bursting point for the configurations incorporating the large strake and either the 30° or 44° wing. Although the surface oil-flow patterns changed as the strake primary vortex bursting point moved from a position aft of the wing trailing edge to the strake apex, no conclusive evidence in the surface oil flow of the burst vortex was observed.

Though not photographically recorded in this report, both the strake and wing unburst primary vortex cores were observed as a result of condensation. However, at the angles of attack for which this observation was made, only one vortex was evidenced by the surface oil flows on the wing. This suggests that the wing primary vortex had not coalesced with the strake primary vortex at these angles of attack, but had merely been displaced away from the wing upper surface by the strake vortex; thus the strake vortex was allowed to dominate the surface flow pattern.

Langley Research Center
National Aeronautics and Space Administration
Hampton, VA 23665
July 17, 1979

REFERENCES

1. Luckring, James M.: Subsonic Longitudinal and Lateral Aerodynamic Characteristics for a Systematic Series of Strake-Wing Configurations. NASA TM-78642, 1979.

2. Fox, Charles H., Jr.: Subsonic Longitudinal and Lateral-Directional Static Stability Characteristics of a General Research Fighter Model Employing a Strake-Wing Concept. NASA TM-74071, 1978.

3. Mechtly, E. A.: The International System of Units - Physical Constants and Conversion Factors (Second Revision). NASA SP-7012, 1973.

4. Gloss, Blair B.: Effect of Canard Location and Size on Canard-Wing Interference and Aerodynamic-Center Shift Related to Maneuvering Aircraft at Transonic Speeds. NASA TN D-7505, 1974.

5. Gloss, Blair B.: The Effect of Canard Leading-Edge Sweep and Dihedral Angle on the Longitudinal and Lateral Aerodynamic Characteristics of a Close-Coupled Canard-Wing Configuration. NASA TN D-7814, 1974.

6. Gloss, Blair B.: Effect of Wing Planform and Canard Location and Geometry on the Longitudinal Aerodynamic Characteristics of a Close-Coupled Canard Wing Model at Subsonic Speeds. NASA TN D-7910, 1975.

7. Schaefer, William T., Jr.: Characteristics of Major Active Wind Tunnels at the Langley Research Center. NASA TM X-1130, 1965.

8. Fox, Charles H., Jr., and Huffman, Jarrett K.: Calibration and Test Capabilities of the Langley 7- by 10-Foot High Speed Tunnel. NASA TM X-74027, 1977.

9. Braslow, Albert L.; Hicks, Raymond M.; and Harris, Roy V., Jr.: Use of Grit-Type Boundary-Layer-Transition Trips on Wind-Tunnel Models. NASA TN D-3579, 1966.

10. Squire, L. C.; Jones, J. G.; and Stanbrook, A.: An Experimental Investigation of the Characteristics of Some Plane and Cambered 65° Delta Wings at Mach Numbers From 0.7 to 2.0. R. & M. No. 3305, British A.R.C., 1963.

11. Lee, G. H.: Note on the Flow Around Delta Wings With Sharp Leading Edges. R. & M. No. 3070, British A.R.C., 1958.

12. Gould, R. W. F.; and Cowdrey, C. F.: High Reynolds Number Tests on a 70° L.E. Sweepback Delta Wing and Body (H.P. 100) in the Compressed Air Tunnel. C.P. No. 387, British A.R.C., 1958.

13. Luckring, James M.: Theoretical and Experimental Analysis of Longitudinal and Lateral Aerodynamic Characteristics of Skewed Wings at Subsonic Speeds to High Angles of Attack. NASA TN D-8512, 1977.

TABLE I.- GEOMETRIC CHARACTERISTICS OF MODEL

Body:
```
Length, cm (in.) . . . . . . . . . . . . . . . . . . . . . . .    96.589 (38.077)
Forebody-afterbody gap, cm (in.) . . . . . . . . . . . . . . .     0.196 (0.077)
```

Wings 1, 2, and 3:
```
A . . . . . . . . . . . . . . . . . . . . . . . . . . . . . . . . . . . . . . 2.5
b/2, cm (in.) . . . . . . . . . . . . . . . . . . . . . . . . . 25.400 (10.000)
λ . . . . . . . . . . . . . . . . . . . . . . . . . . . . . . . . . . . . . . 0.2
Λ_w, deg, for -
  Wing 1 . . . . . . . . . . . . . . . . . . . . . . . . . . . . . . . . . 30.00
  Wing 2 . . . . . . . . . . . . . . . . . . . . . . . . . . . . . . . . . 44.03
  Wing 3 . . . . . . . . . . . . . . . . . . . . . . . . . . . . . . . . . 59.45
c̄, cm (in.) . . . . . . . . . . . . . . . . . . . . . . . . . . 23.327 (9.184)
Longitudinal model station of wing apex, cm (in.) . . . . . . 47.747 (18.798)
Longitudinal model station of moment reference point,
  cm (in.) . . . . . . . . . . . . . . . . . . . . . . . . . . 55.197 (21.731)
Airfoil section . . . . . . . . . . . . . . . . . . . . . . . . . Circular arc
S_ref, reference area, cm² (in²) . . . . . . . . . . . . . . . . 1032 (159.970)
Root chord at fuselage center line, cm (in.) . . . . . . . . . 33.863 (13.332)
Tip chord, cm (in.) . . . . . . . . . . . . . . . . . . . . . . 6.769 (2.665)
Chord at wing-fuselage juncture, cm (in.) . . . . . . . . . . 29.799 (11.732)
Maximum thickness, percent chord, at -
  Wing-fuselage juncture . . . . . . . . . . . . . . . . . . . . . . . . . . 6.0
  Tip . . . . . . . . . . . . . . . . . . . . . . . . . . . . . . . . . . . 4.0
```

Strakes 1, 2, and 3:
```
Basic planform . . . . . . . . . . . . . . . . . . . . . . . . . See table II
Coordinates of trailing edge at maximum semispan . . . . . . . See table III
S_s/S_ref . . . . . . . . . . . . . . . . . . . . . . . . . . . See table IV
Longitudinal model station of strake apex, cm (in.) . . . . . 15.494 (6.100)
Root chord at strake-fuselage juncture, cm (in.) . . . . . . . 32.131 (12.650)
Cross section . . . . . . . . . . . . . . . . . . . . . Sharp-edged, flat plate
Thickness, cm (in.) . . . . . . . . . . . . . . . . . . . . . . 0.318 (0.125)
Bevel semiangle, deg . . . . . . . . . . . . . . . . . . . . . . . . . . 10.85
```

Vertical tail:
```
Λ_t, deg . . . . . . . . . . . . . . . . . . . . . . . . . . . . . . . . 51.70
Exposed span, cm (in.) . . . . . . . . . . . . . . . . . . . . 13.442 (5.292)
Chord at tail-fuselage juncture, cm (in.) . . . . . . . . . . 17.917 (7.054)
Tip chord, cm (in.) . . . . . . . . . . . . . . . . . . . . . . 3.586 (1.412)
S_t, cm² (in²) . . . . . . . . . . . . . . . . . . . . . . . . 144.523 (22.401)
Longitudinal model station of apex, cm (in.) . . . . . . . . . 82.271 (32.390)
Airfoil section . . . . . . . . . . . . . . . . . . . . . . . . . Circular arc
Maximum thickness, percent chord, at -
  Tail-fuselage juncture . . . . . . . . . . . . . . . . . . . . . . . . . . 6.0
  Tip . . . . . . . . . . . . . . . . . . . . . . . . . . . . . . . . . . . 4.0
```

TABLE II.- BASIC STRAKE PLANFORM COORDINATES

| x | | y for - | | | | | |
| | | Strake 1
y_{max} = 2.540 cm
(1.000 in.) | | Strake 2
y_{max} = 5.080 cm
(2.000 in.) | | Strake 3
y_{max} = 7.620 cm
(3.000 in.) | |
cm	in.	cm	in.	cm	in.	cm	in.
0	0	0	0	0	0	0	0
19.050	7.500	1.080	.425	2.159	.850	3.239	1.275
20.320	8.000	1.163	.458	2.324	.915	3.487	1.373
21.590	8.500	1.270	.500	2.540	1.000	3.810	1.500
22.860	9.000	1.397	.550	2.794	1.100	4.191	1.650
29.210	11.500	2.045	.805	4.089	1.610	6.134	2.415
30.480	12.000	2.159	.850	4.318	1.700	6.477	2.550
33.020	13.000	2.350	.925	4.698	1.850	7.049	2.775
34.290	13.500	2.426	.955	4.851	1.910	7.277	2.865
35.560	14.000	2.484	.978	4.966	1.955	7.450	2.933
36.830	14.500	2.535	.998	5.067	1.995	7.602	2.993
38.100	15.000	2.540	1.000	5.080	2.000	7.620	3.000
46.947	18.483	2.540	1.000	5.080	2.000	7.620	3.000

TABLE III.- INTERSECTION COORDINATES OF STRAKE LEADING AND TRAILING EDGES

[Paired (x,y) coordinates with respect to axis system of figure 1(b)]

| $\Lambda_{te,s}$,
deg | Unit | Coordinates of intersection point of strake
leading and trailing edges | | |
		Strake 1 y_{max} = 2.540 cm (1.000 in.)	Strake 2 y_{max} = 5.080 cm (2.000 in.)	Strake 3 y_{max} = 7.620 cm (3.000 in.)
30.00	cm	(35.469, 2.479)	(36.962, 5.080)	(38.435, 7.620)
	in.	(13.964, 0.976)	(14.552, 2.000)	(15.132, 3.000)
44.03	cm	(36.472, 2.520)	(38.948, 5.080)	(41.402, 7.620)
	in.	(14.359, 0.992)	(15.334, 2.000)	(16.300, 3.000)
59.45	cm	(38.339, 2.540)	(42.644, 5.080)	(46.947, 7.620)
	in.	(15.094, 1.000)	(16.789, 2.000)	(18.483, 3.000)

TABLE IV.- EXPOSED STRAKE AREA IN PERCENT WING REFERENCE AREA

$$[S_{ref} = 1032 \ cm^2 \ (159.970 \ in^2)]$$

$\Lambda_{te,s}$, deg	Exposed strake area, percent wing reference area, for -		
	Strake 1 $y_{max} = 2.540$ cm (1.000 in.)	Strake 2 $y_{max} = 5.080$ cm (2.000 in.)	Strake 3 $y_{max} = 7.620$ cm (3.000 in.)
30.00	0.07444	0.15591	0.24469
44.03	.07791	.17013	.27666
59.45	.08133	.18384	.30753
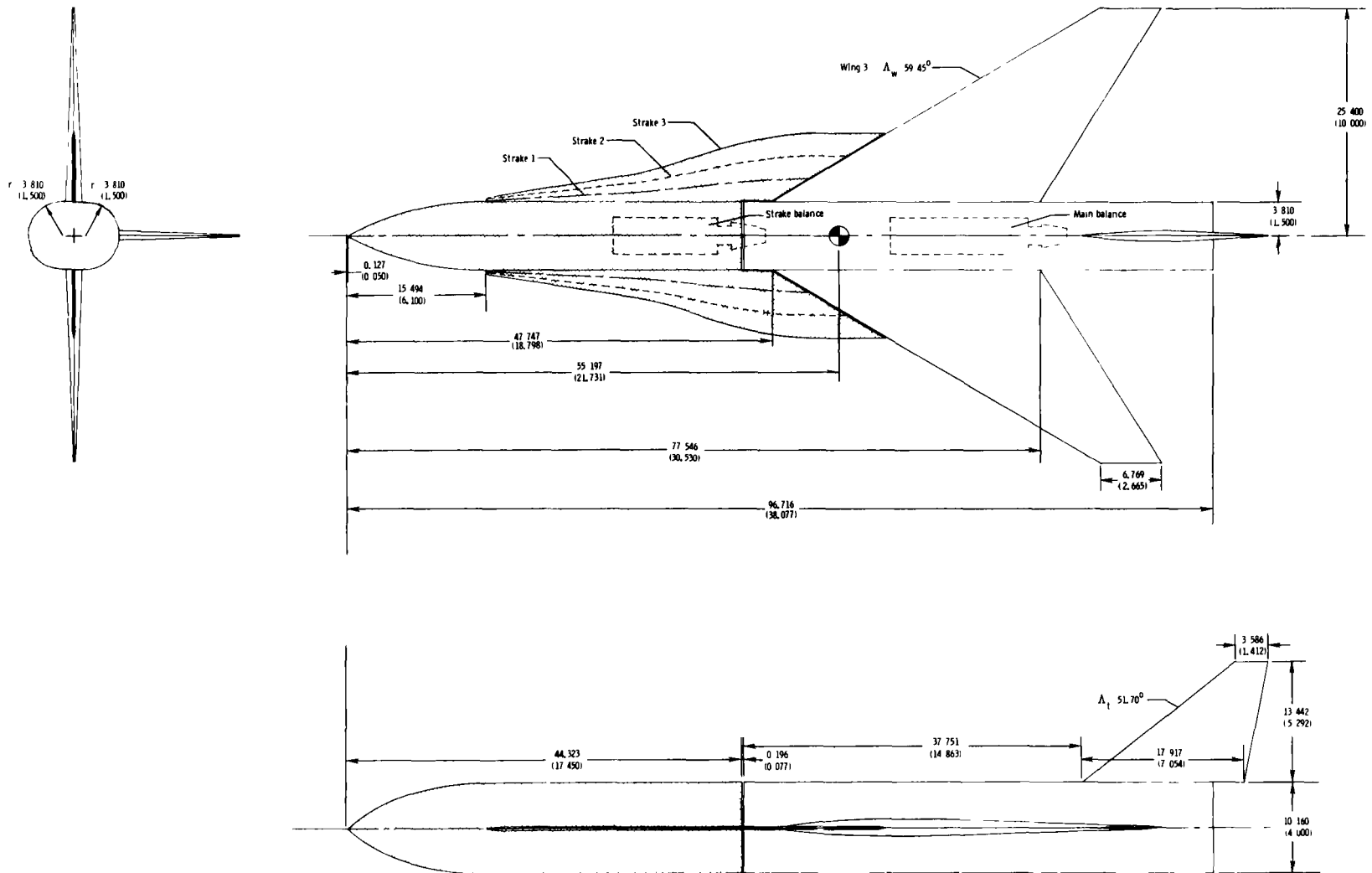
(a) Three-view drawing of complete configuration.

Figure 1.- Details of model. All linear dimensions are in centimeters (inches).
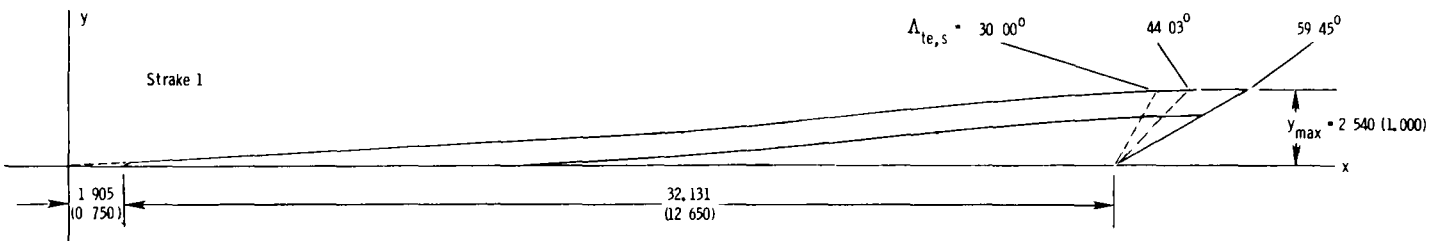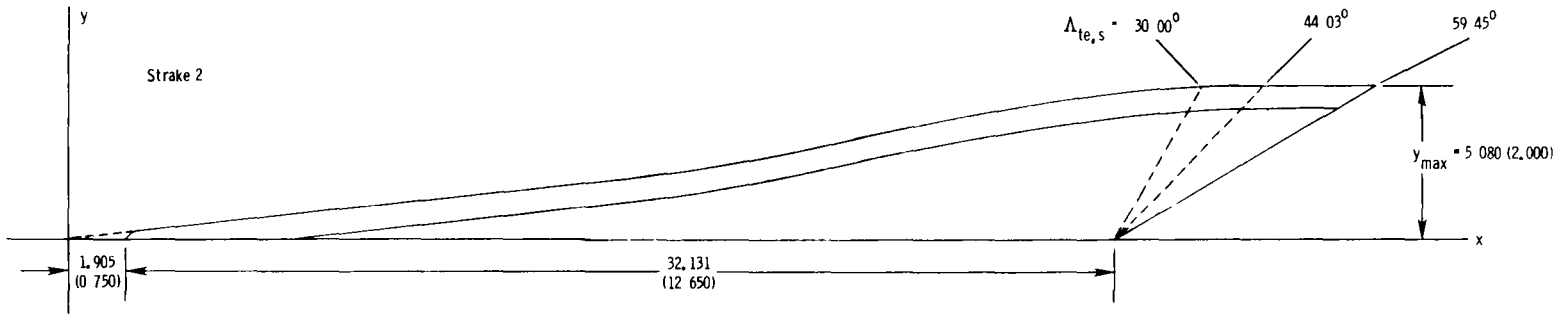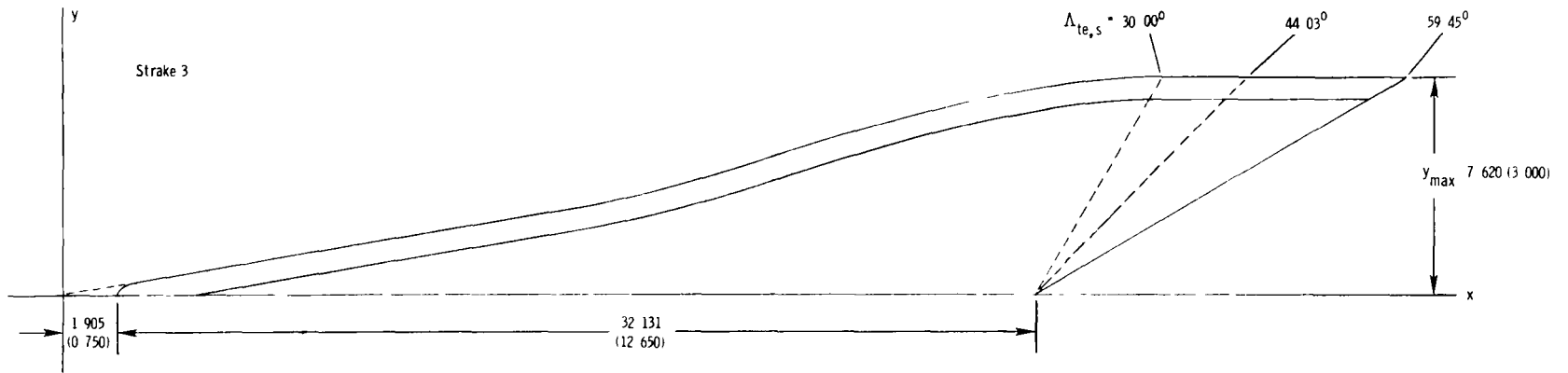
(b) Exposed strake planforms.

Figure 1.- Continued.

6.769
(2 665)

$\Lambda_W = 30\ 00^0$

21.590
(8.500)

Wing 1

29 799
(11 732)

6.769
(2.665)

$\Lambda_W = 44.03^0$

21.590
(8.500)

Wing 2

29.799
(11.732)

6.769
(2.665)

$\Lambda_W = 59.45^0$

21 590
(8 500)

Wing 3

29.799
(11.732)
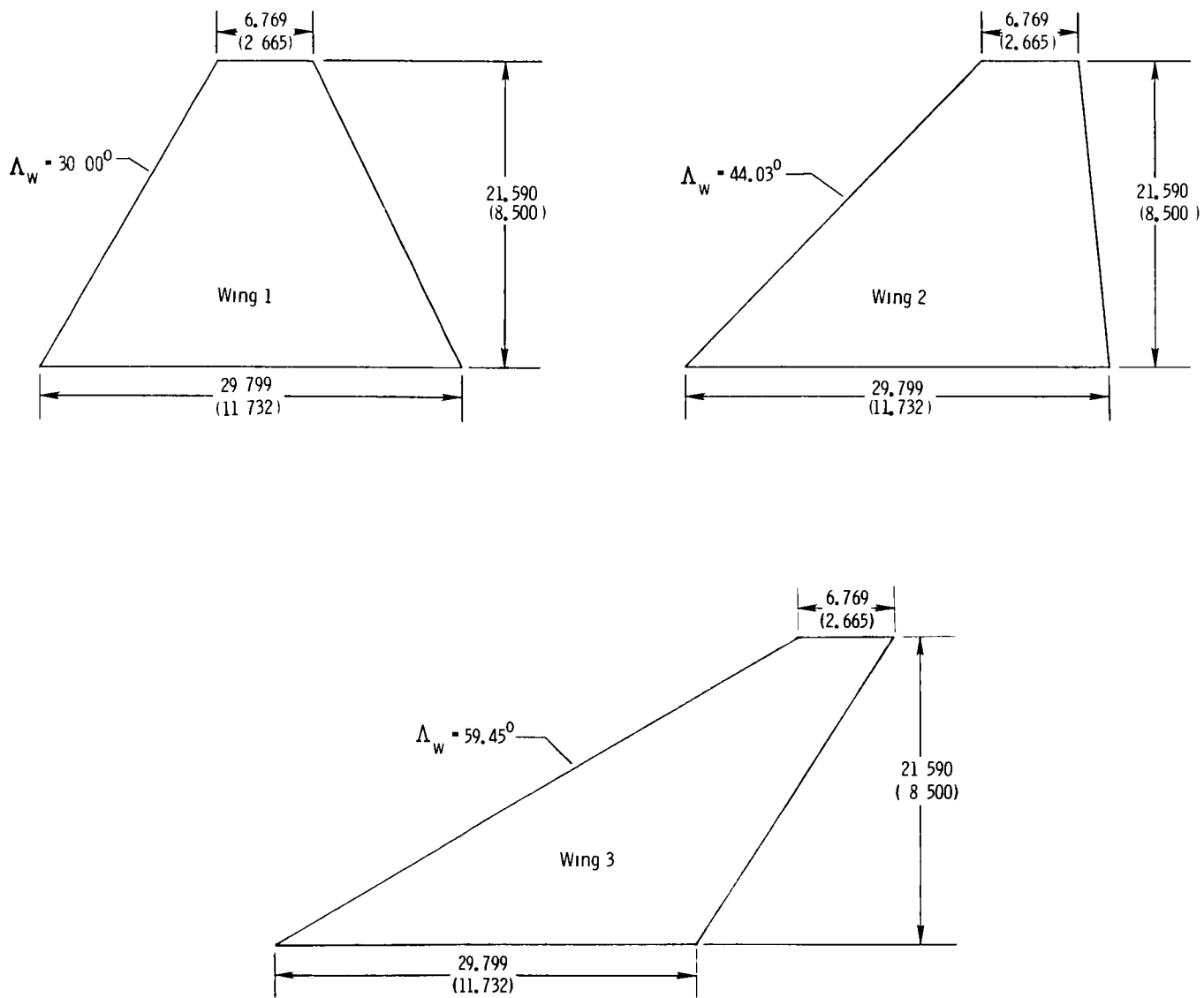
(c) Exposed wing planforms.

Figure 1.- Concluded.
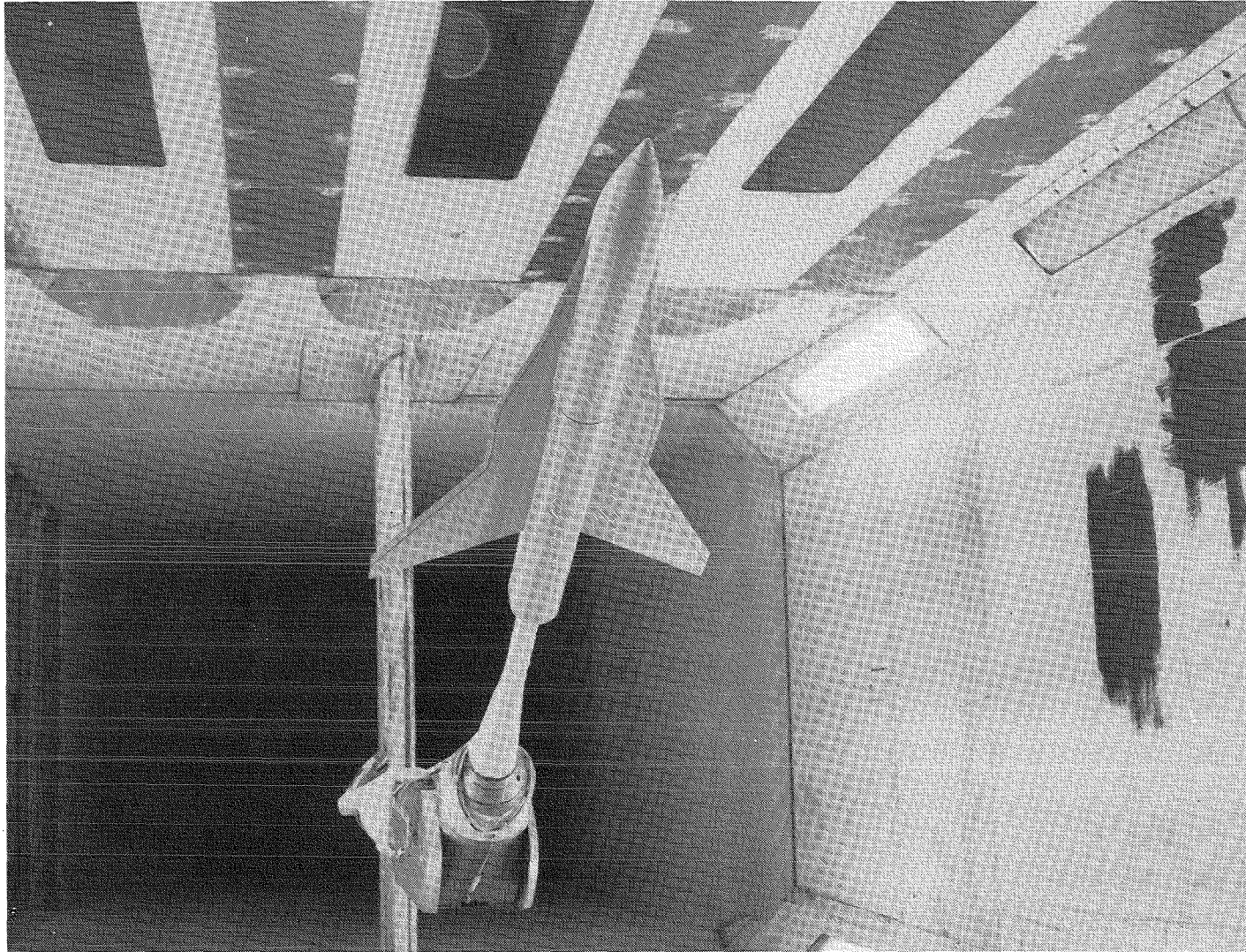
L-77-4894

(a) One-quarter front view.

Figure 2.- Photograph of model mounted in Langley high-speed 7- by 10-foot tunnel. $\Lambda_W = 59.45^O$, strake 3.

L-77-4892

(b) One-quarter rear view.

Figure 2.- Continued.
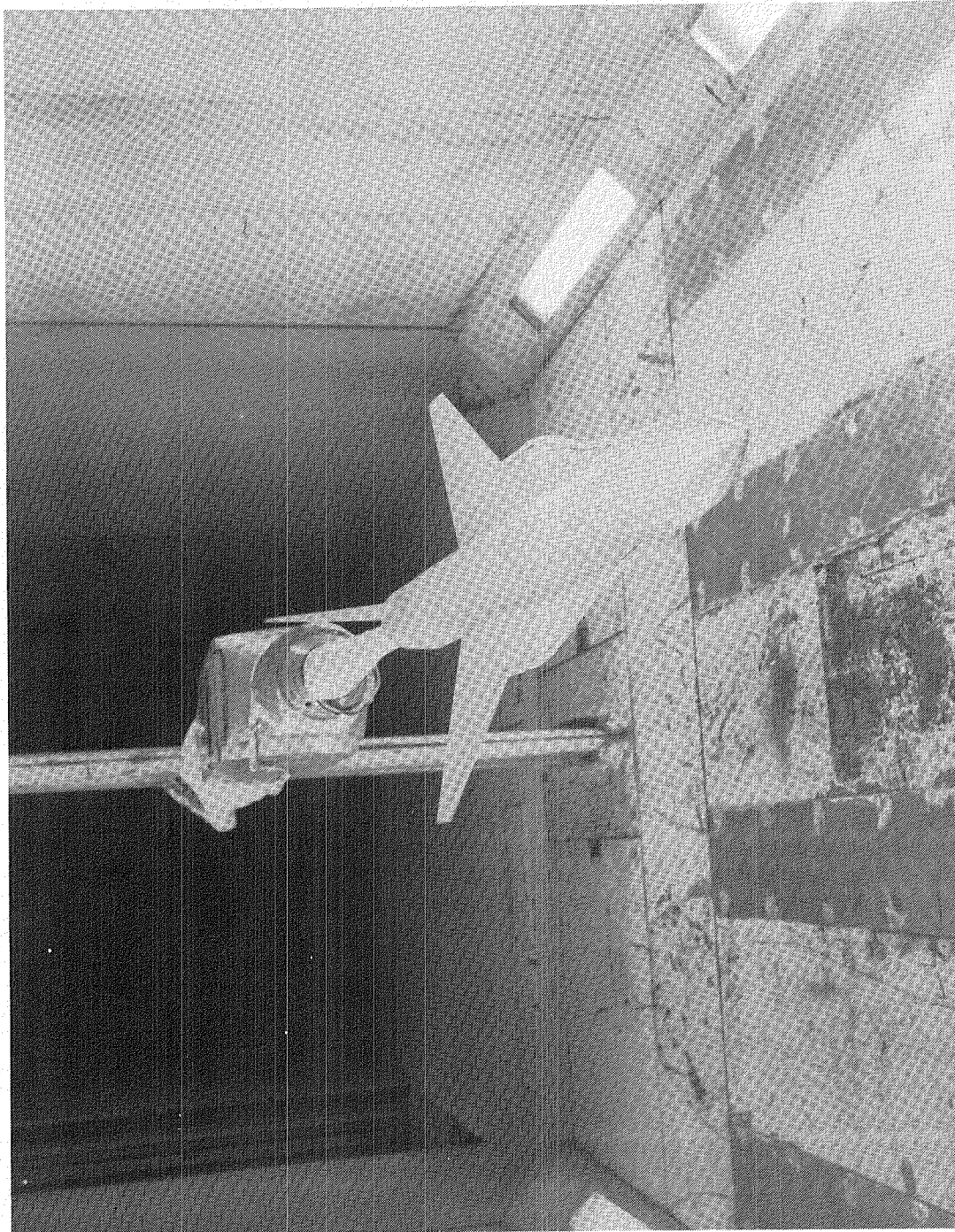
L-77-4891

(c) One-quarter front view.

Figure 2.- Concluded.
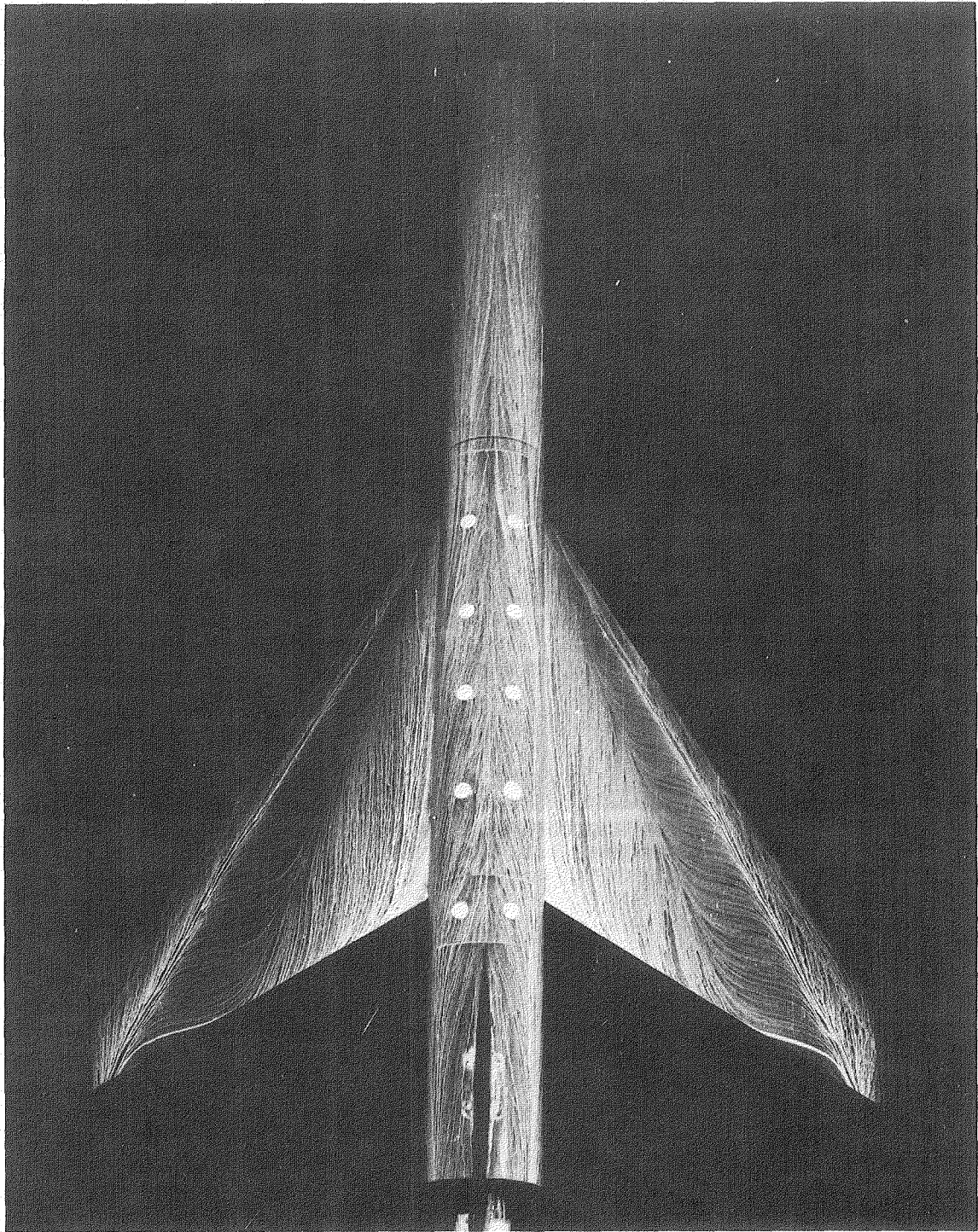
L-79-200

(a) Surface flow pattern.

Figure 3.- General characteristics of surface flow patterns for
configuration 60-0. $\alpha = 10^O$; $M_\infty = 0.3$.

22
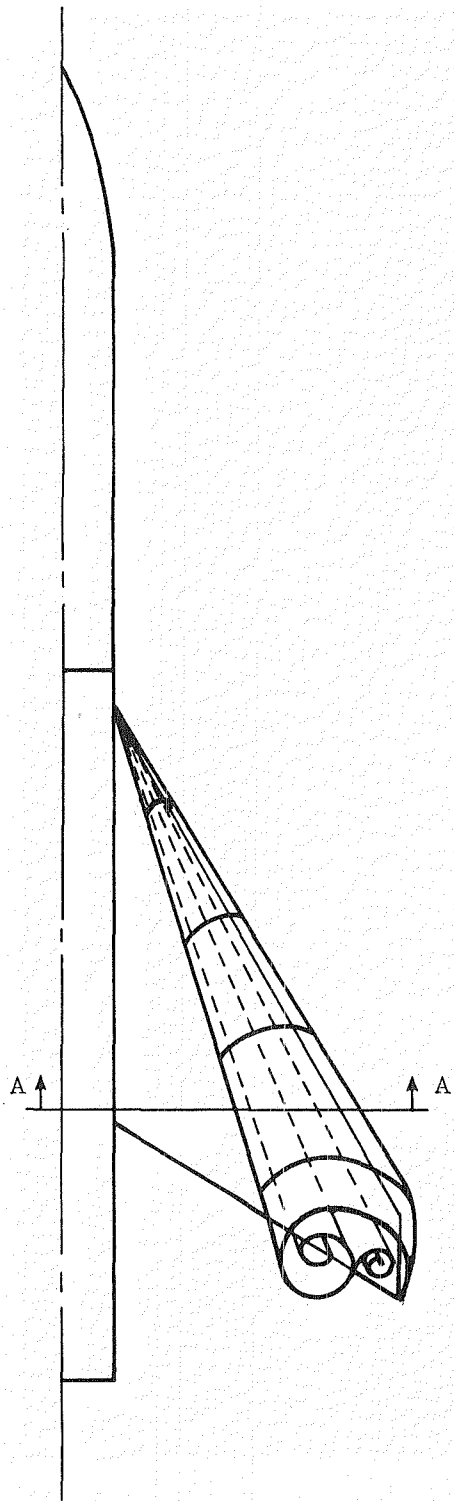
Key points

a	Primary separation
b	Primary reattachment
c	Secondary separation
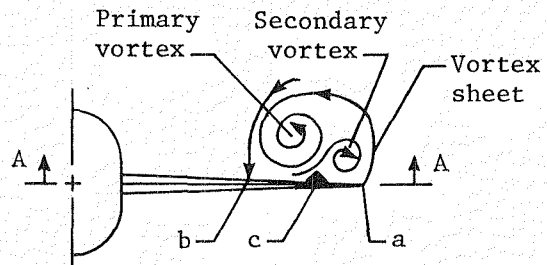
(b) Flow sketch.

Figure 3.- Concluded.
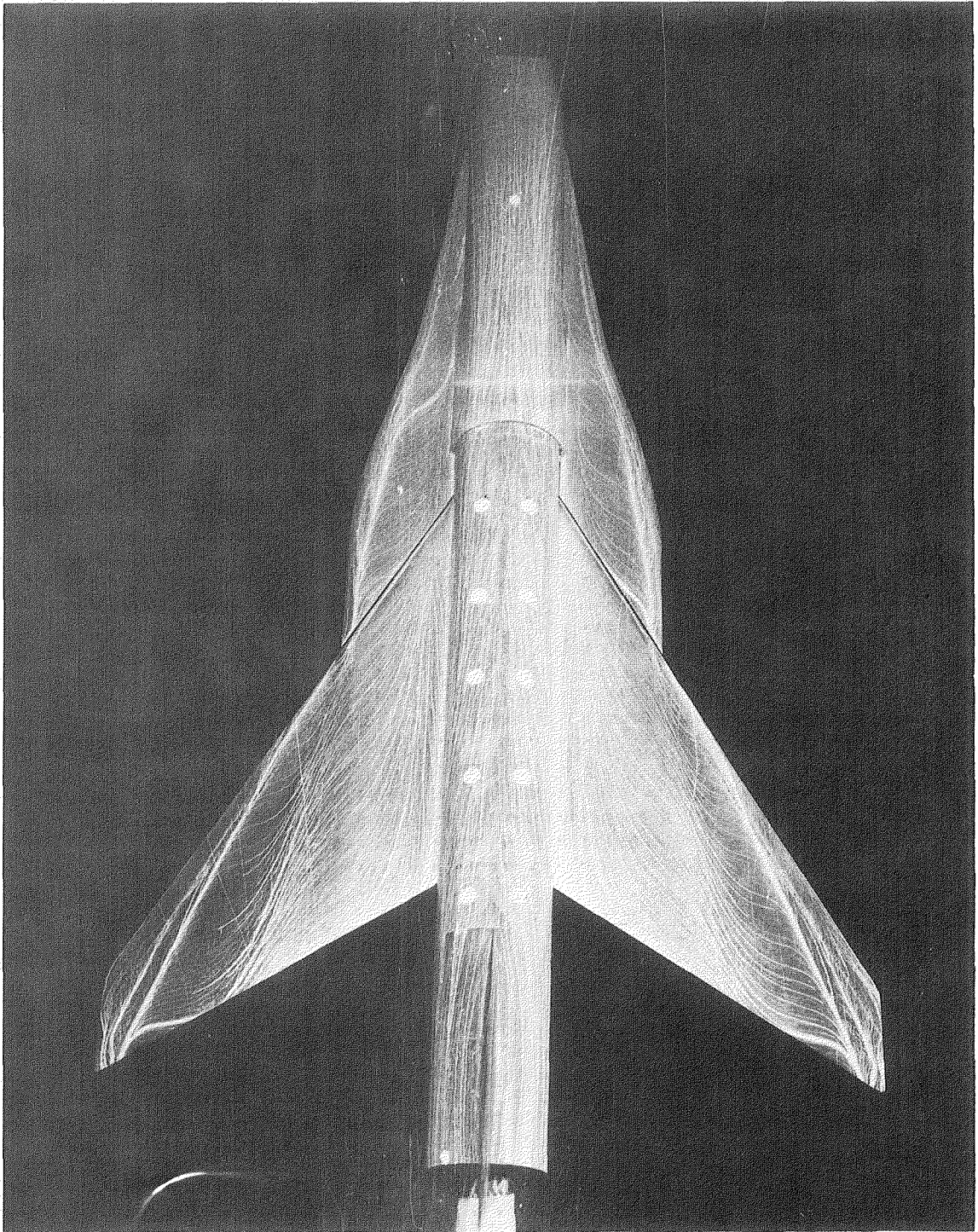
L-79-201

(a) Surface flow pattern.

Figure 4.- General characteristics of surface flow patterns for
configuration 60-3. $\alpha = 10^{\circ}$; gap open; $M_{\infty} = 0.3$.
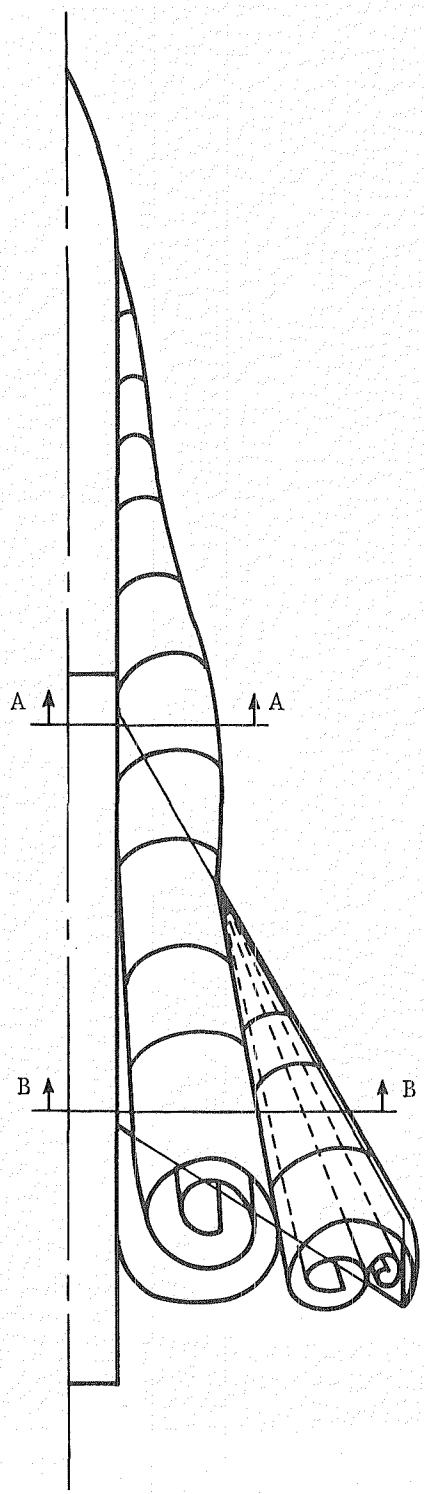
Key points

a	Primary separation
b	Primary reattachment
c	Secondary separation

Strake vortices:

Primary — Secondary

A A

b — c — a

Vortices:

Strake   Wing

Primary — Primary — Secondary

B B

b — c — a
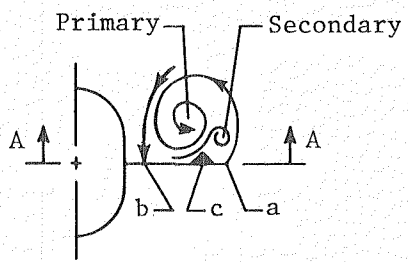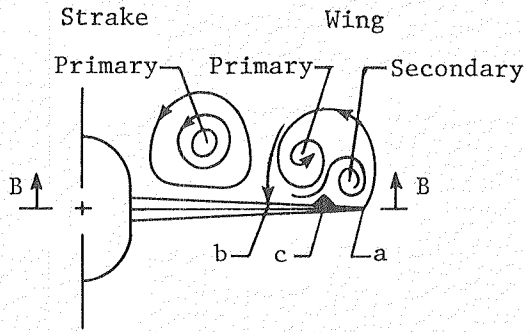
(b) Flow sketch.

Figure 4.- Concluded.

25

L-79-202

(a) $\alpha = 5^{\circ}$.
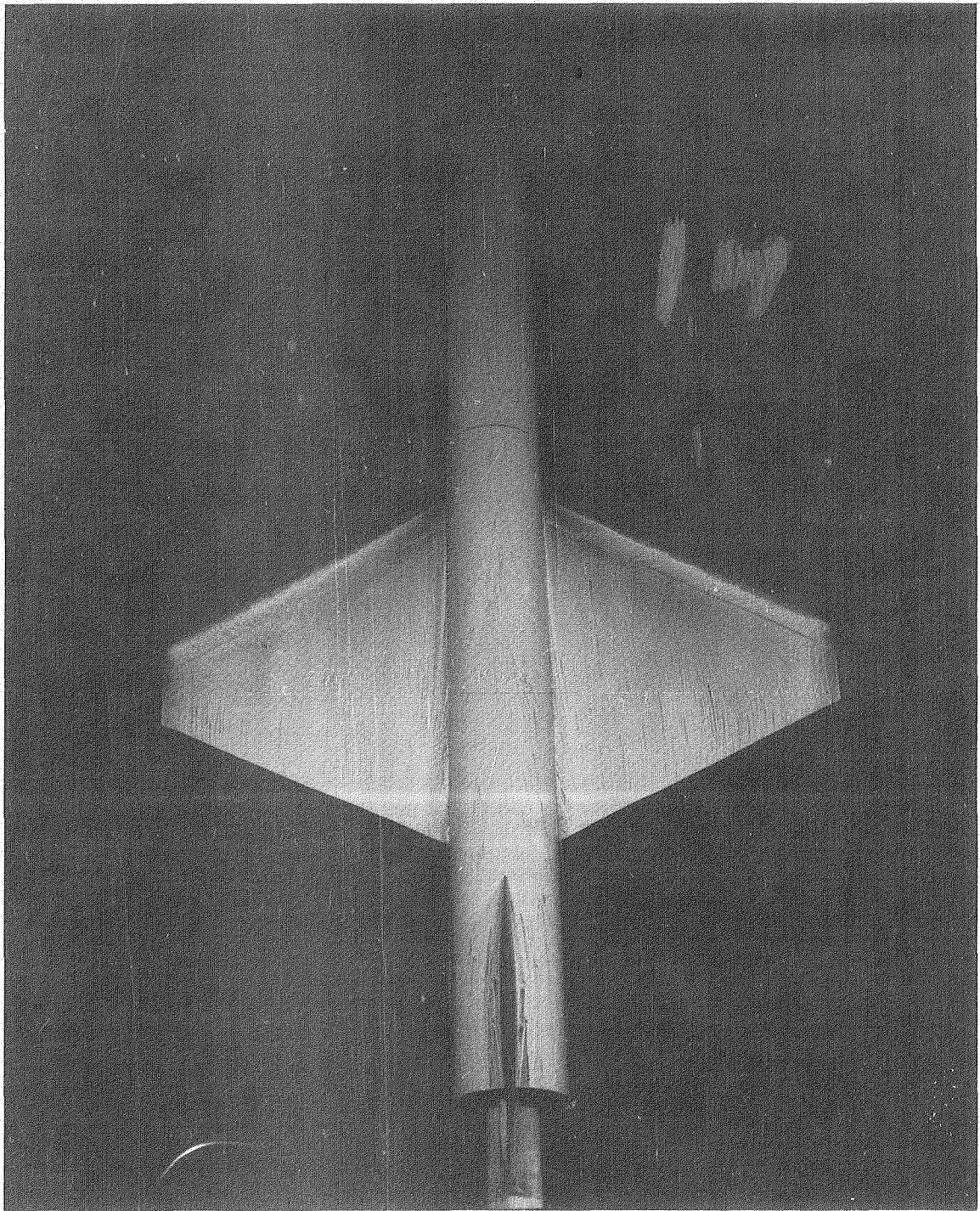
Figure 5.- Surface flow patterns for configuration 30-0 at $M_{\infty} = 0.3$.
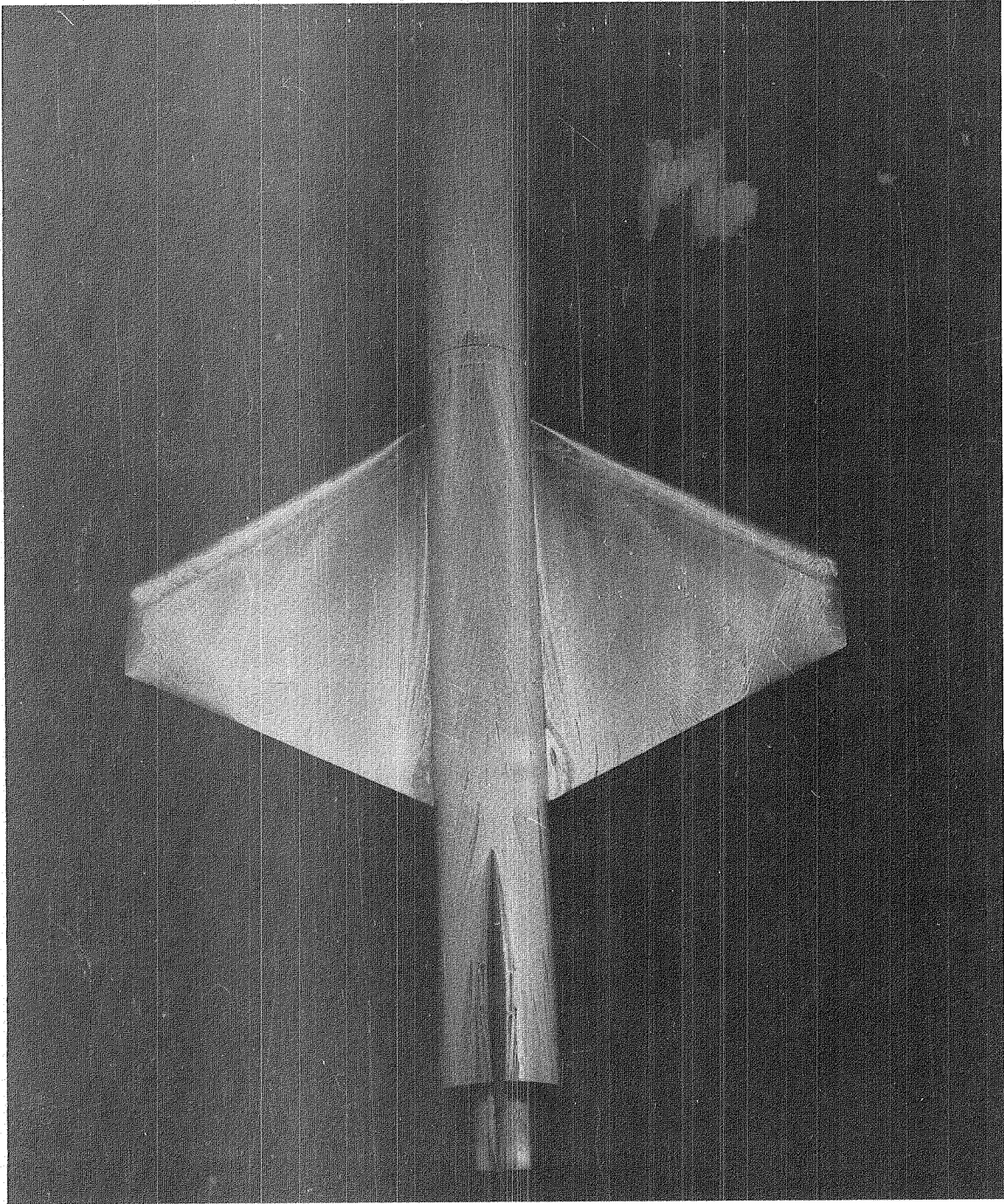
L-79-203

(b) $\alpha = 10^{\circ}$.

Figure 5.- Continued.

27

L-79-204

(c) $\alpha = 15^O$.

Figure 5.- Continued.

L-79-205

(d) $\alpha = 20^{\circ}$.

Figure 5.- Continued.

L-79-206

(e) $\alpha = 25^{\circ}$.
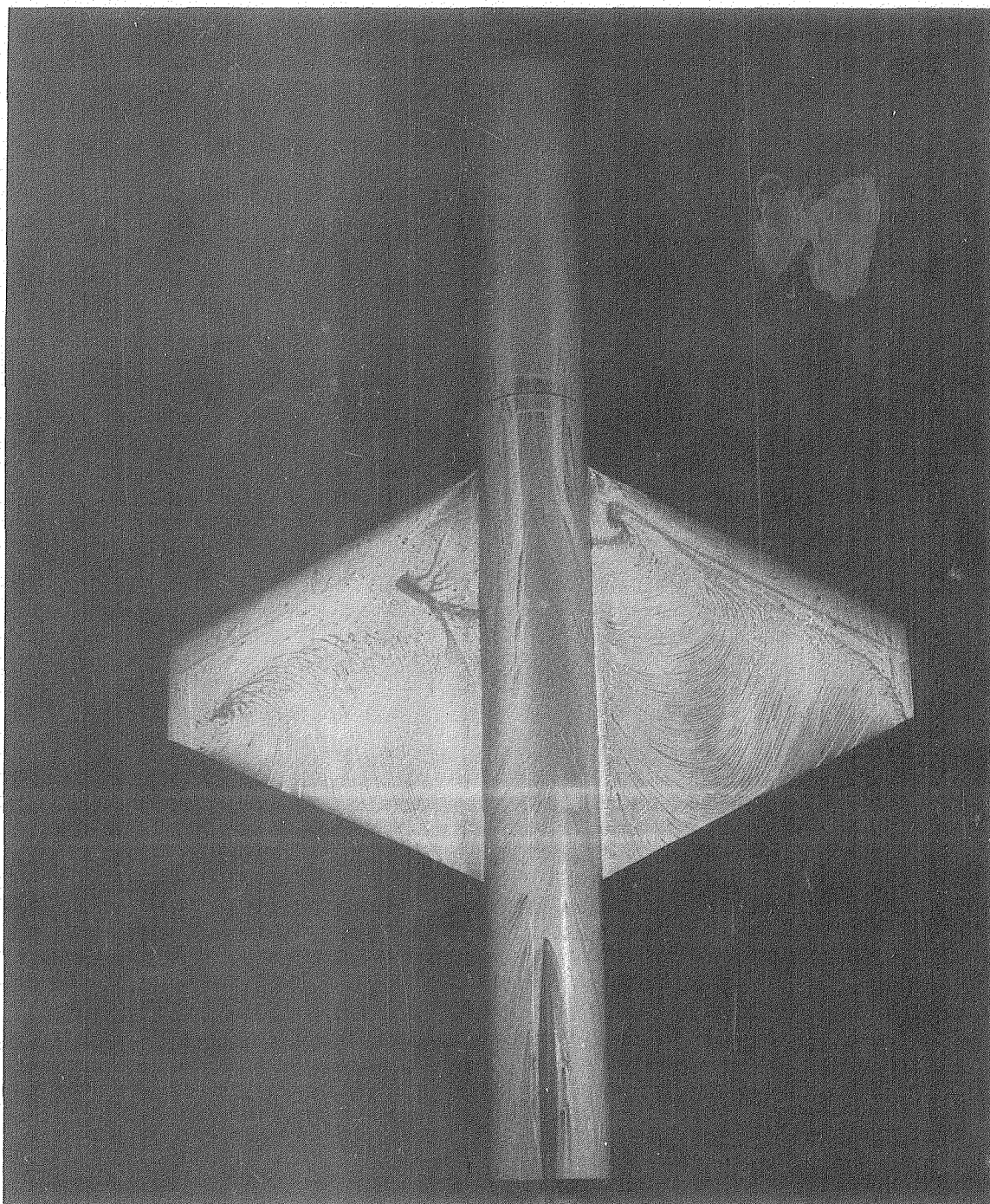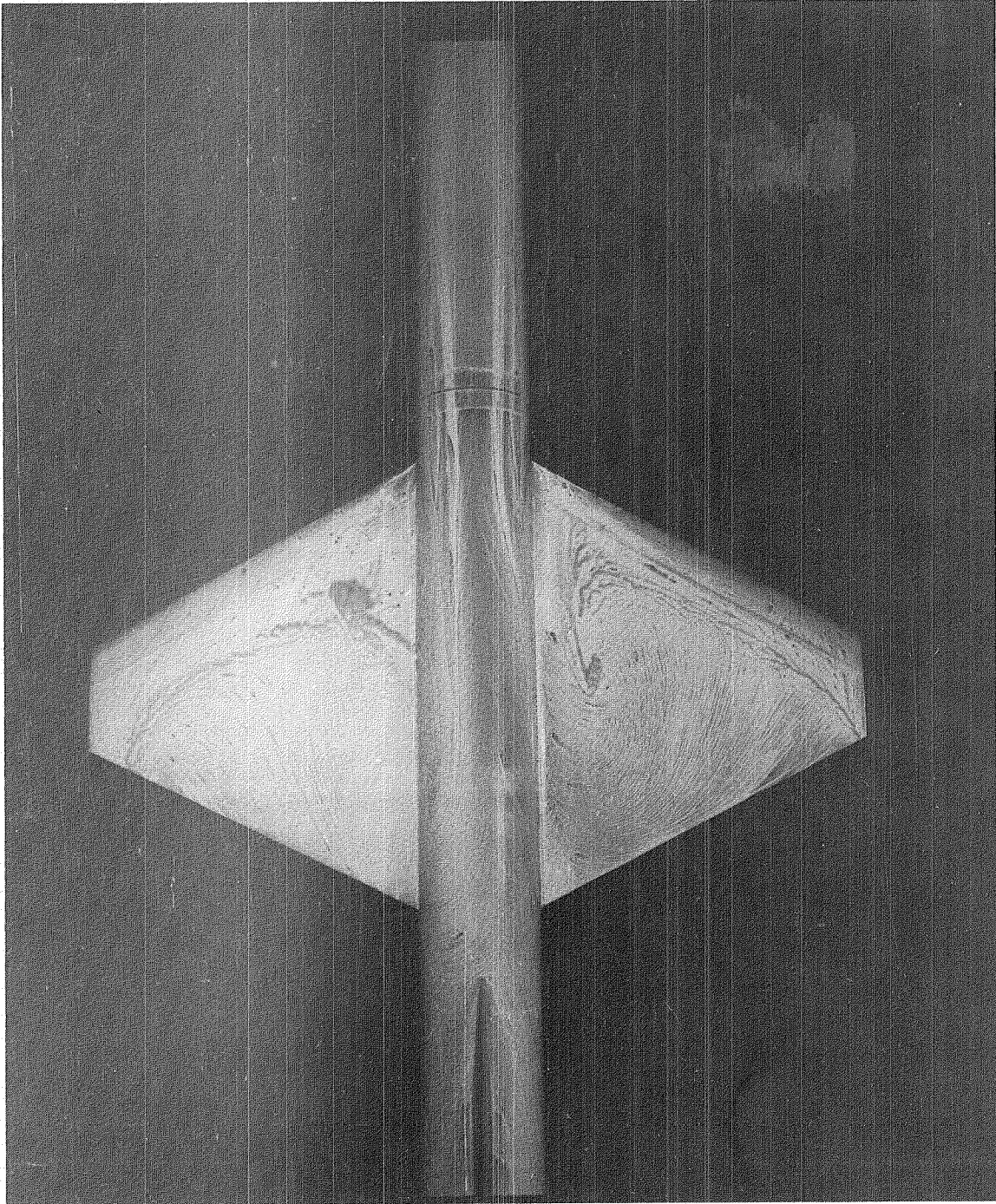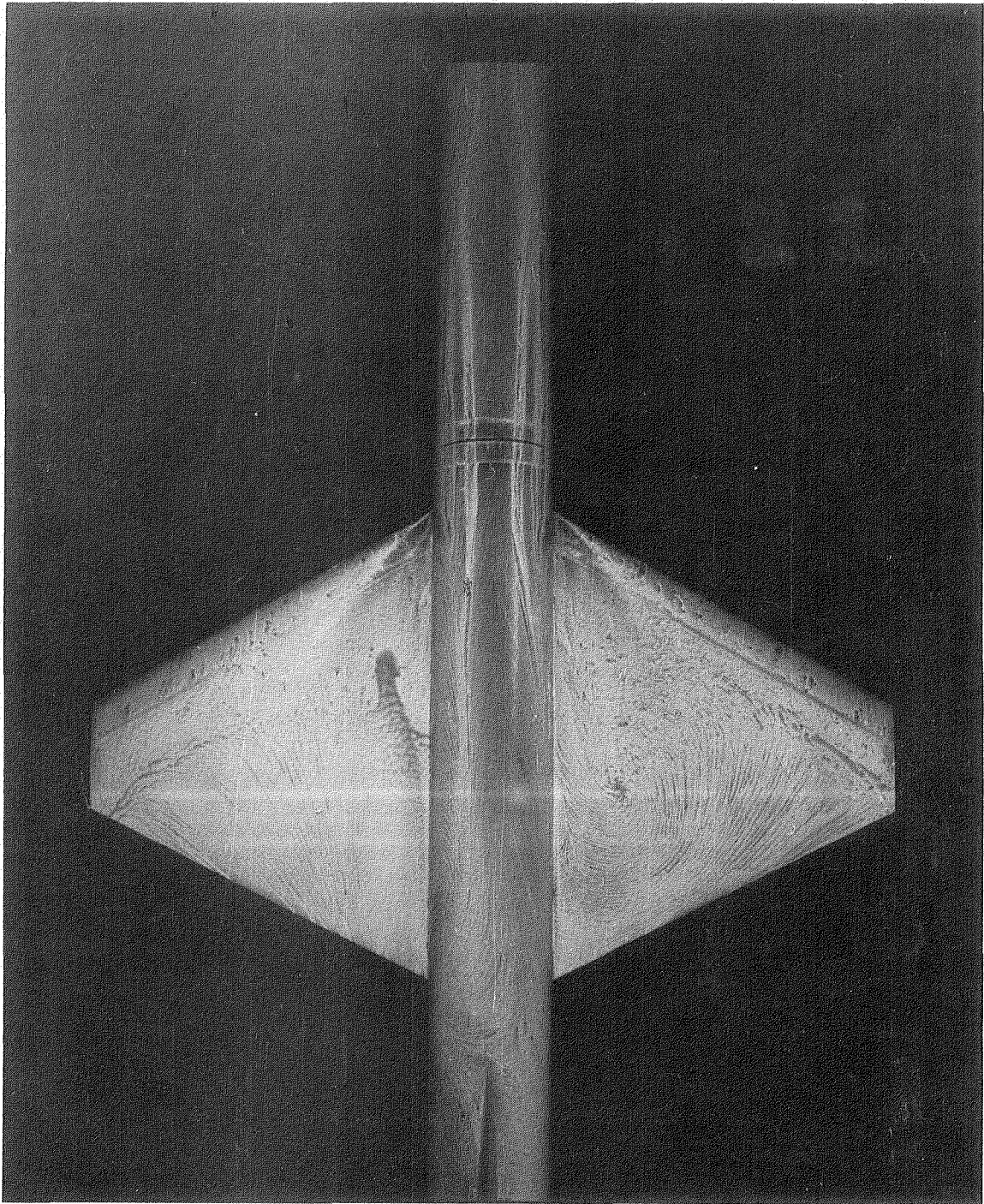
Figure 5.- Continued.

(f) $\alpha = 30^O$.
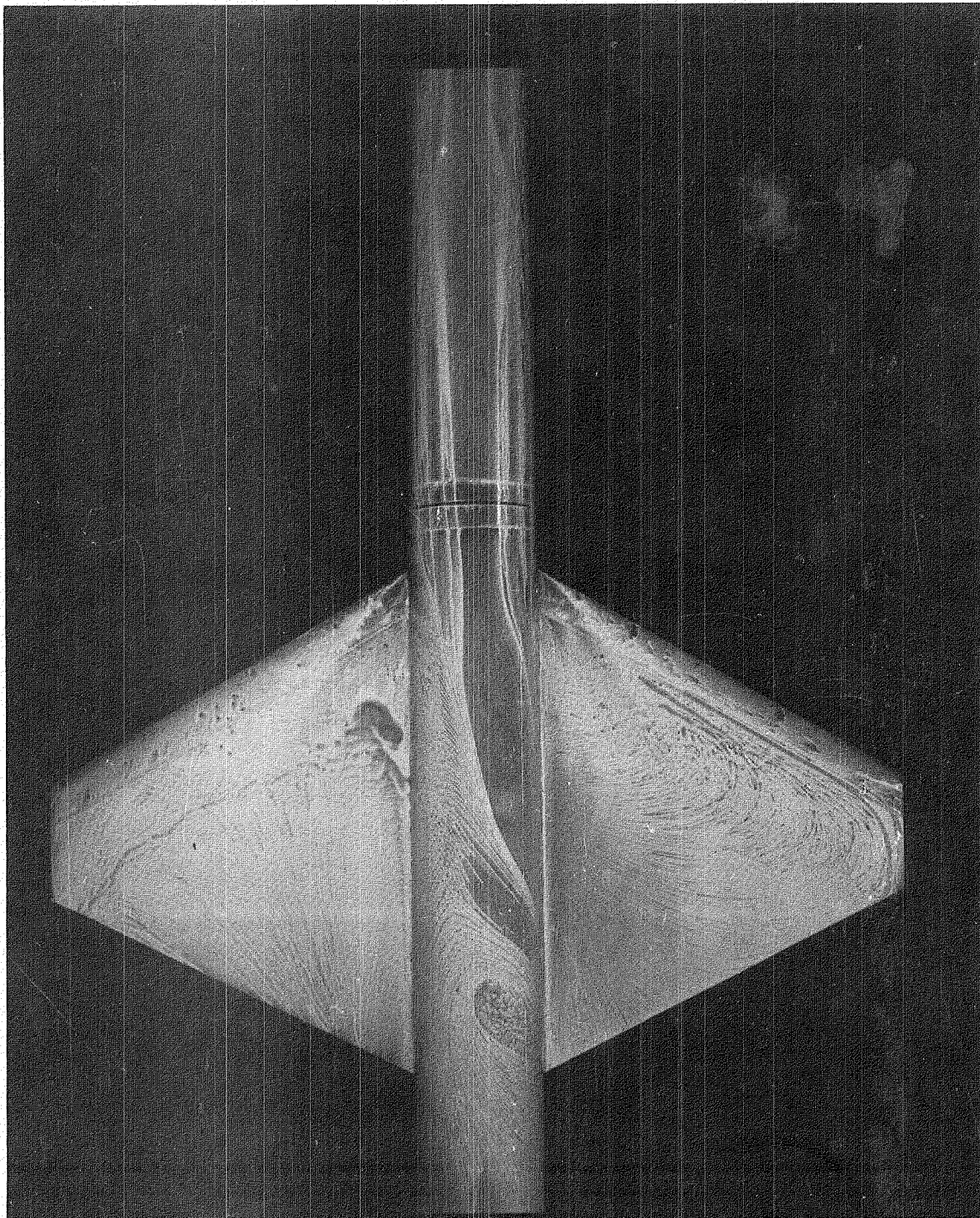
Figure 5.- Concluded.

L-79-208

(a) $\alpha = 5^{\circ}$.
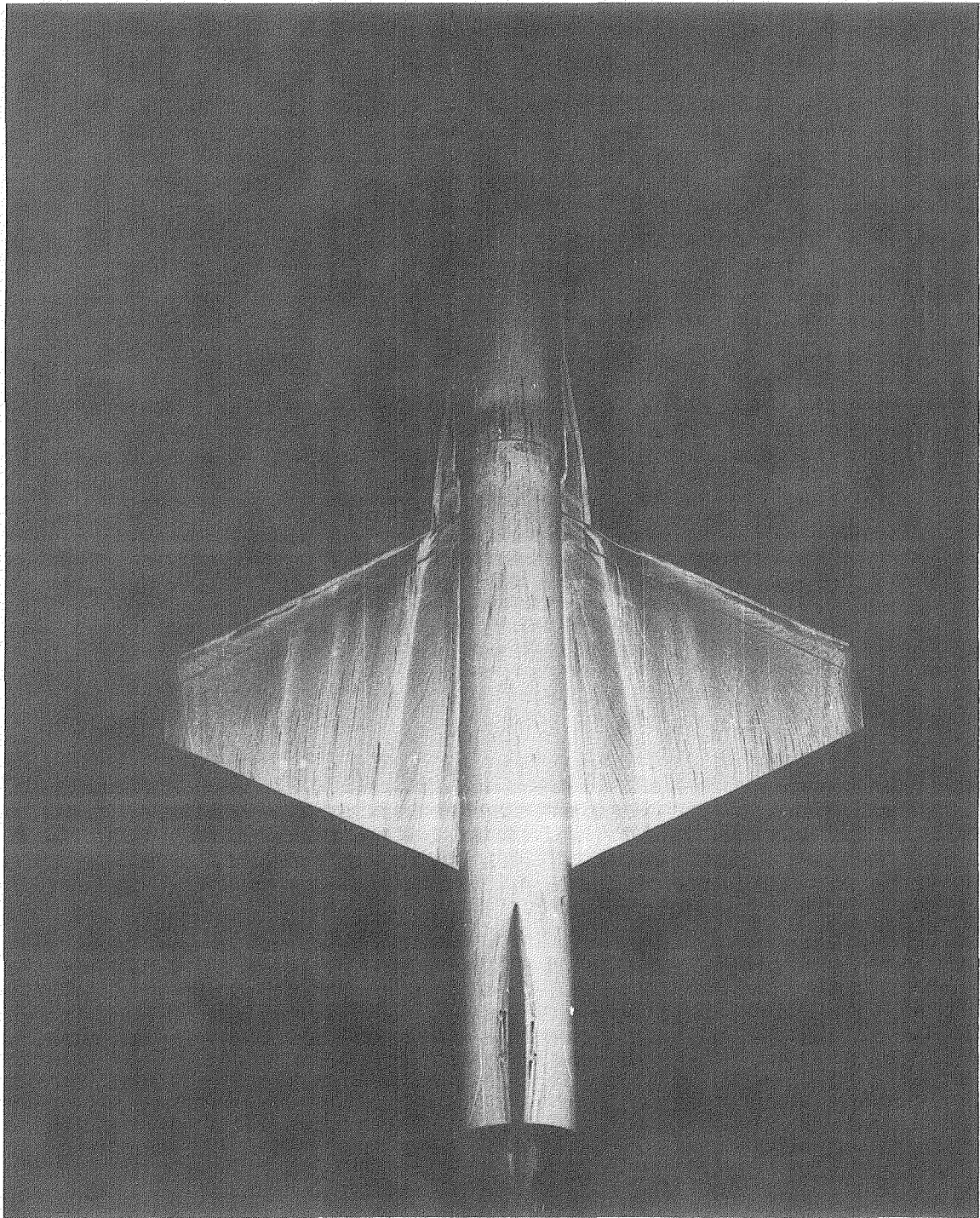
Figure 6.- Surface flow patterns for configuration 30-1, with gap sealed, at $M_{\infty} = 0.3$.
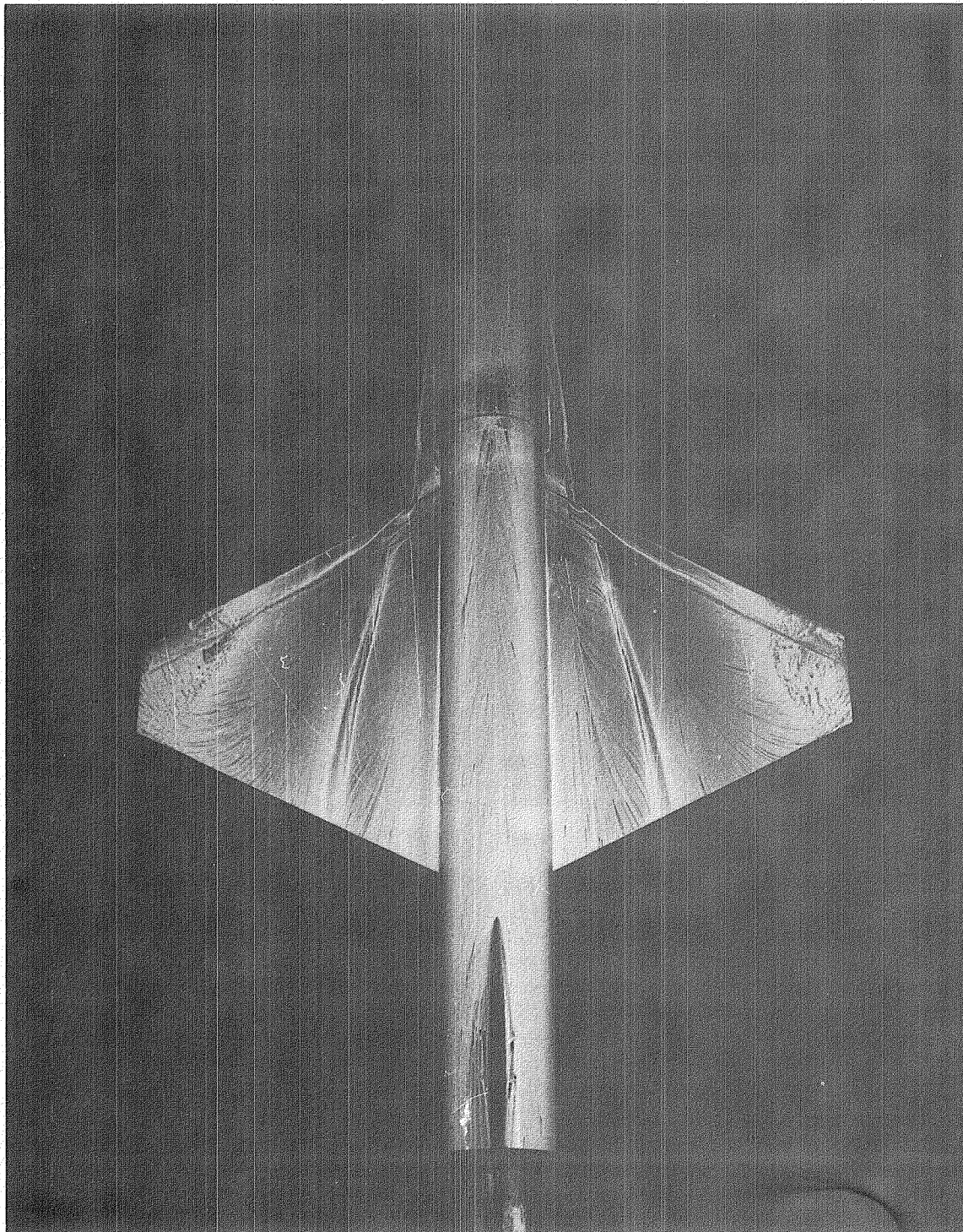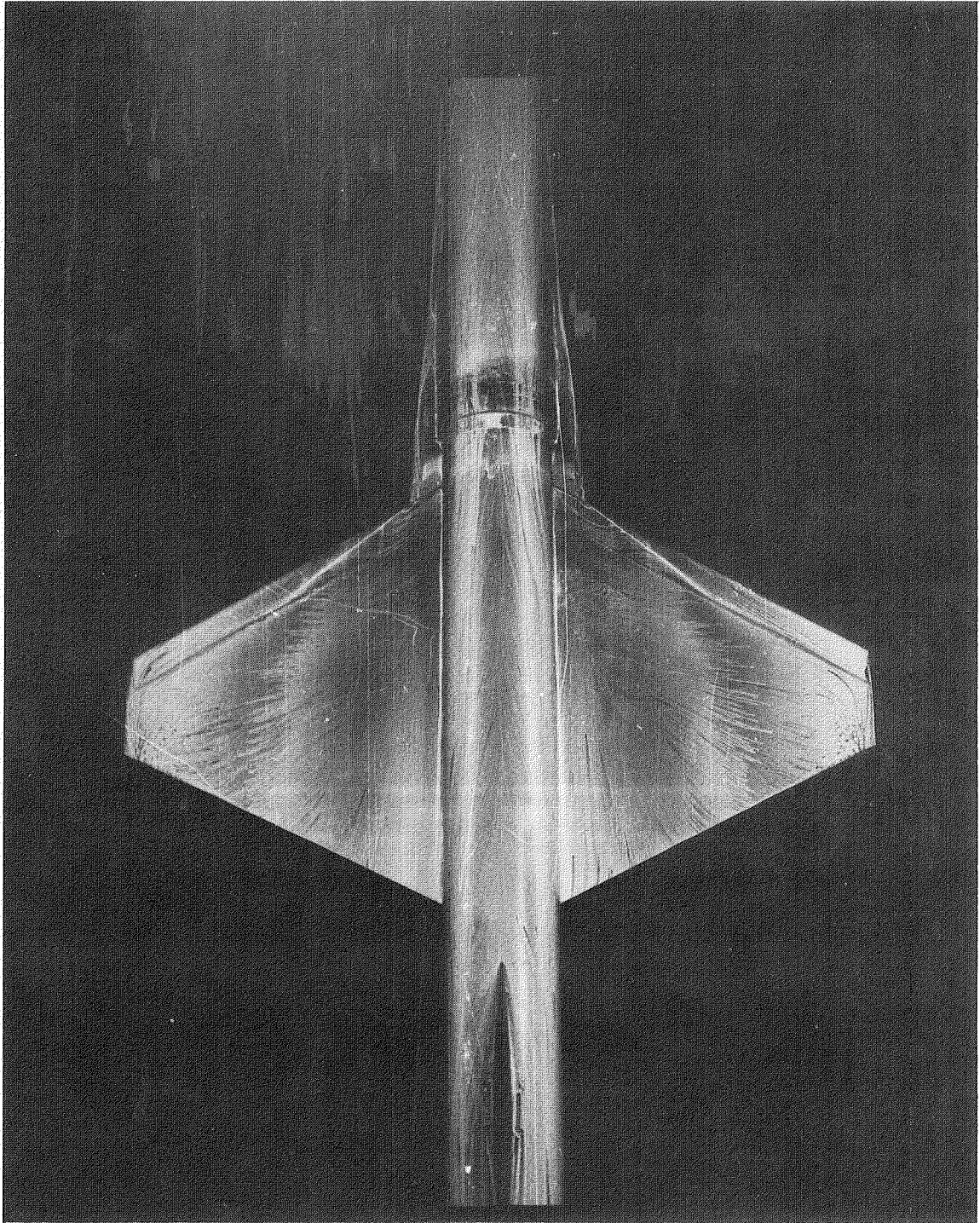
L-79-209

(b) $\alpha = 10^o$.

Figure 6.- Continued.

33

L-79-210

(c) $\alpha = 15^\circ$.

Figure 6.- Continued.

34

L-79-211

(d) $\alpha = 20°$.

Figure 6.- Continued.

L-79-212

(e) $\alpha = 25^{o}$.

Figure 6.- Continued.

L-79-213

(f) $\alpha = 30^{O}$.
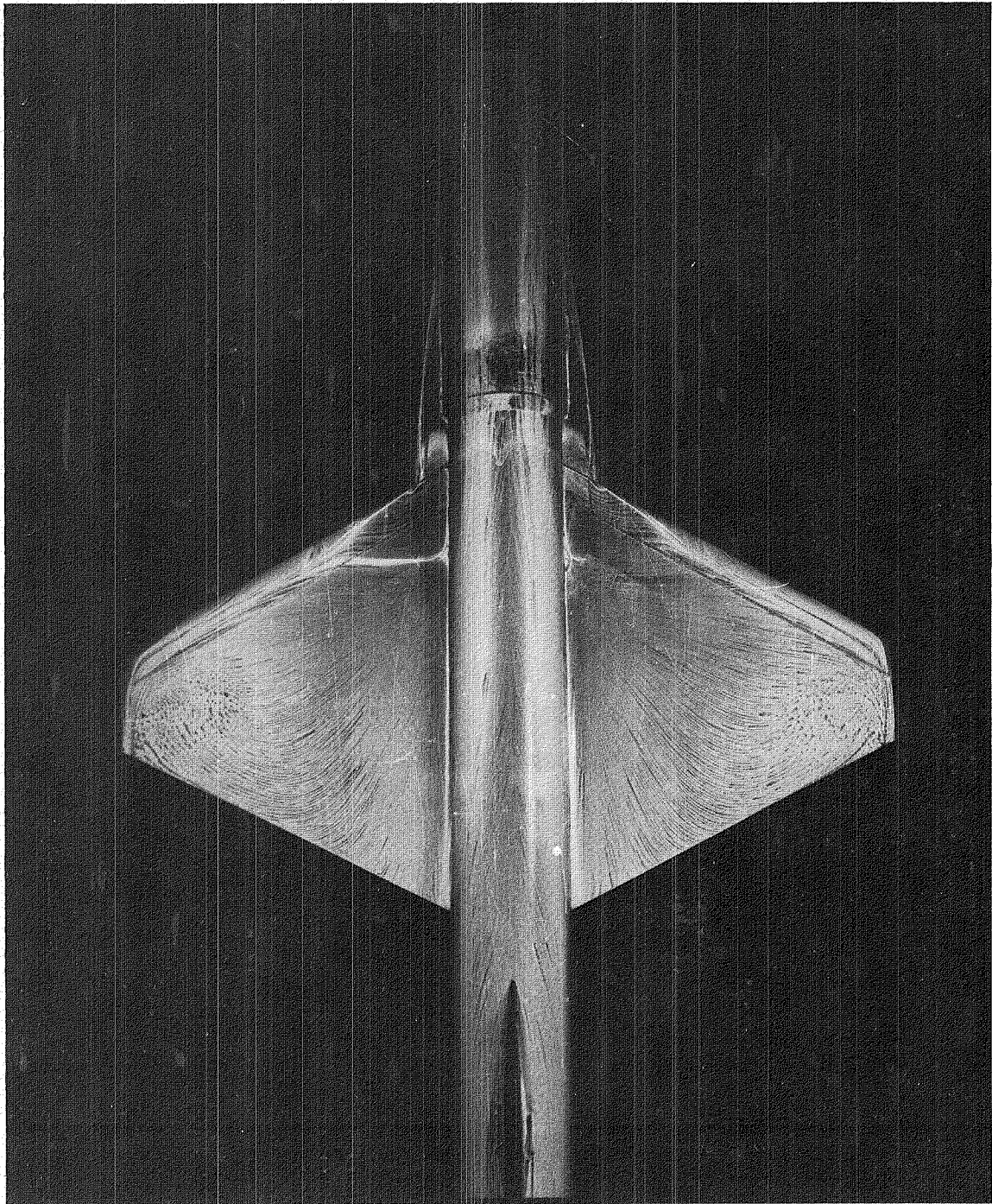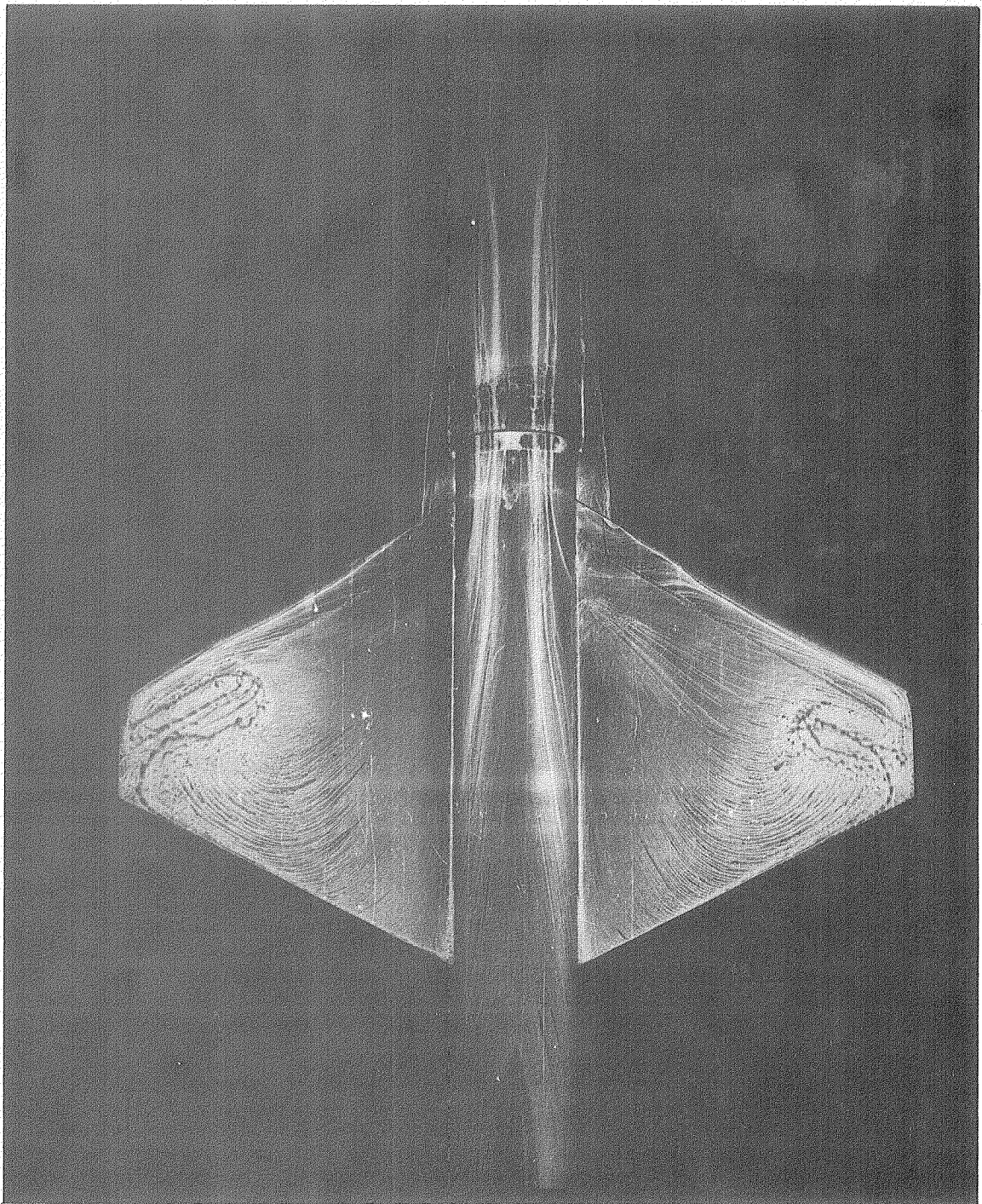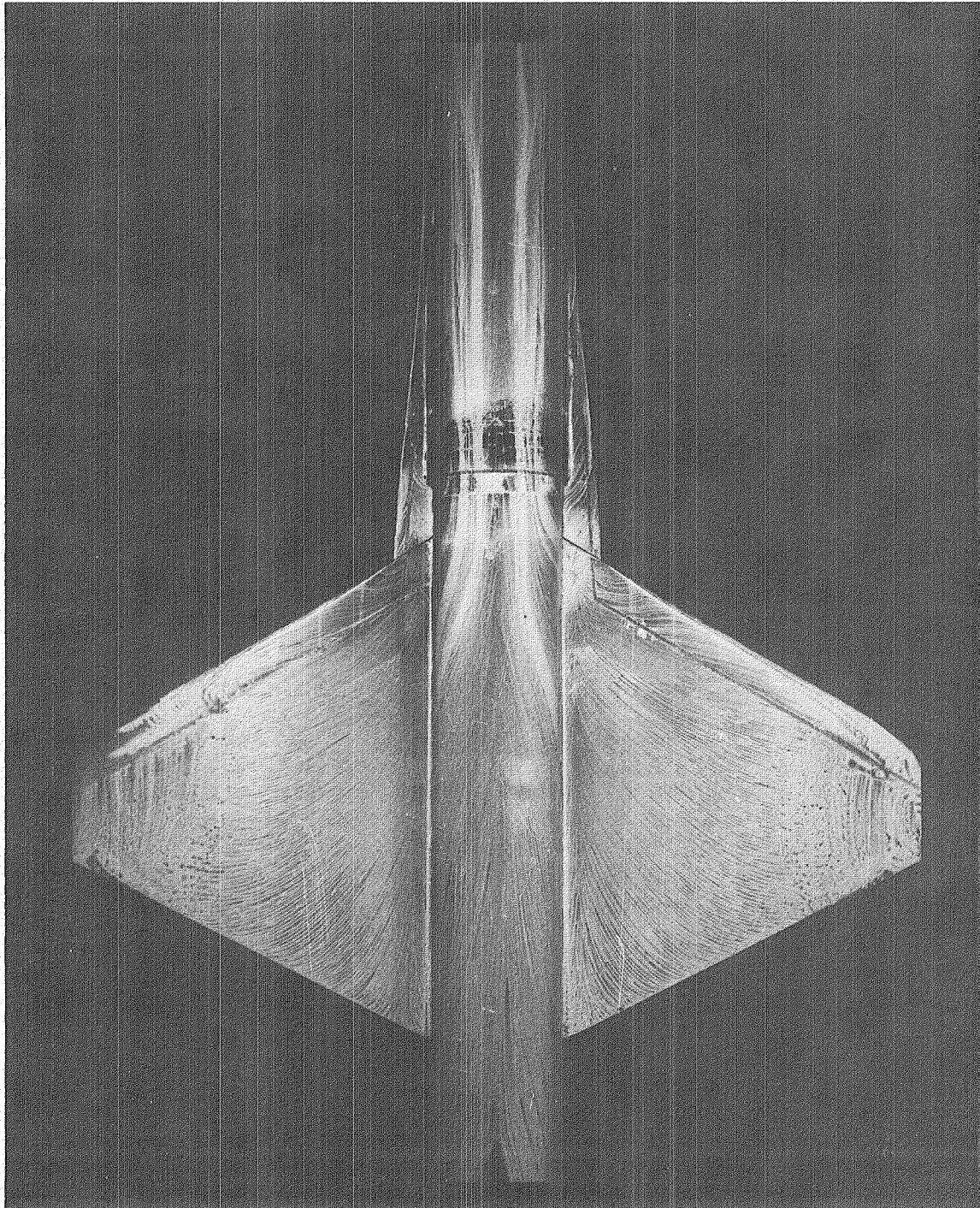
Figure 6.- Concluded.

L-79-214

(a) $\alpha = 5^o$.
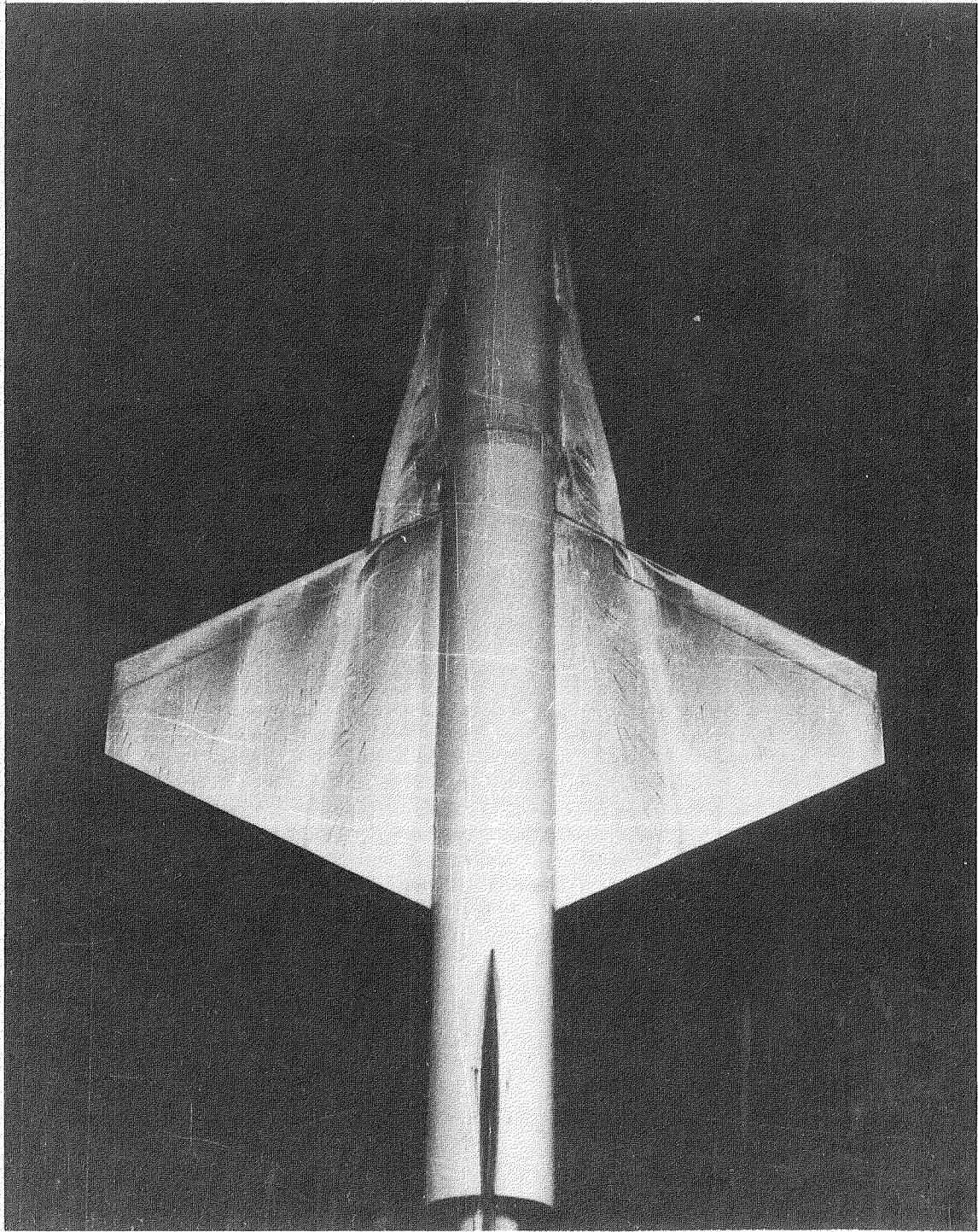
Figure 7.- Surface flow patterns for configuration 30-2, with gap sealed, at $M_\infty = 0.3$.
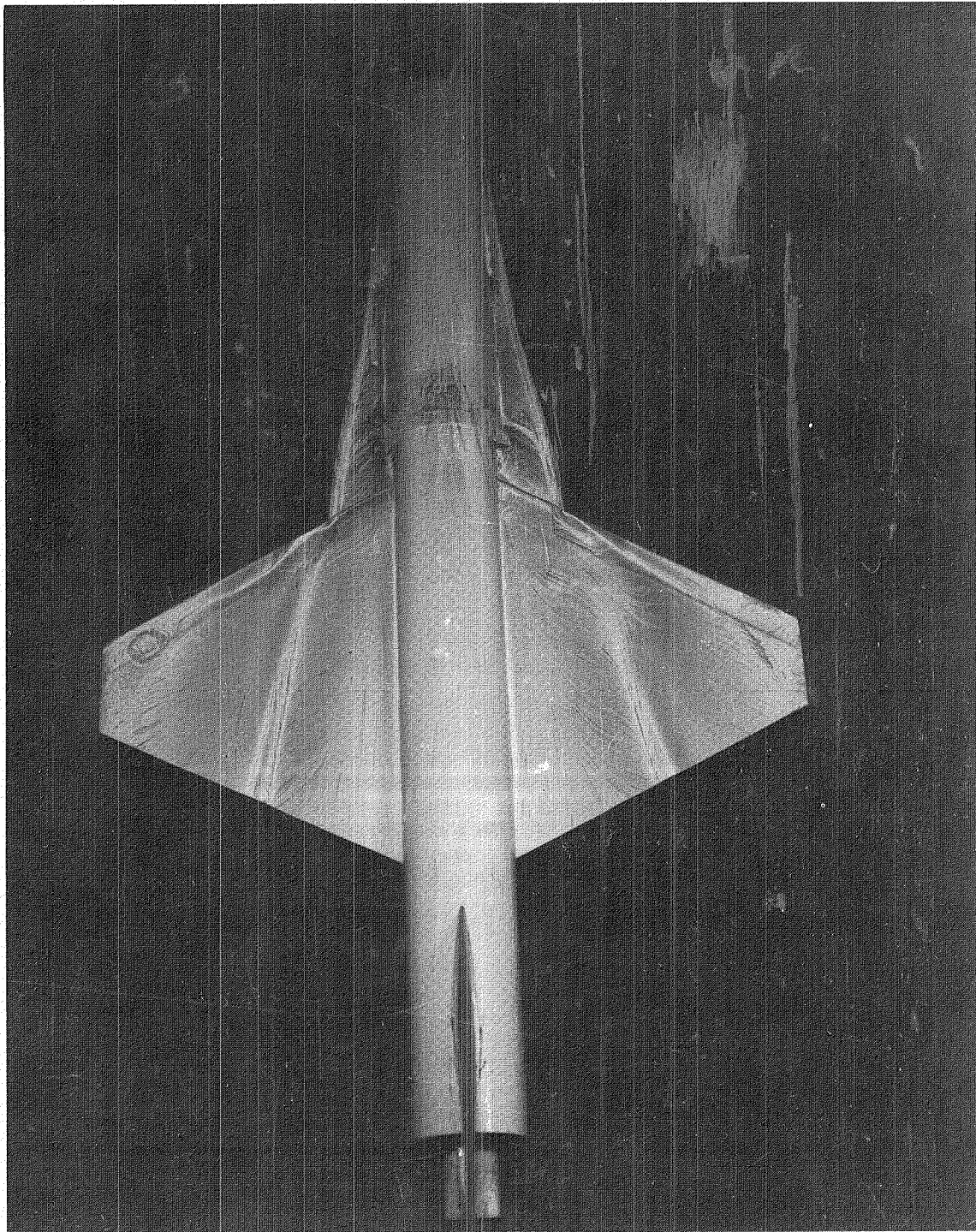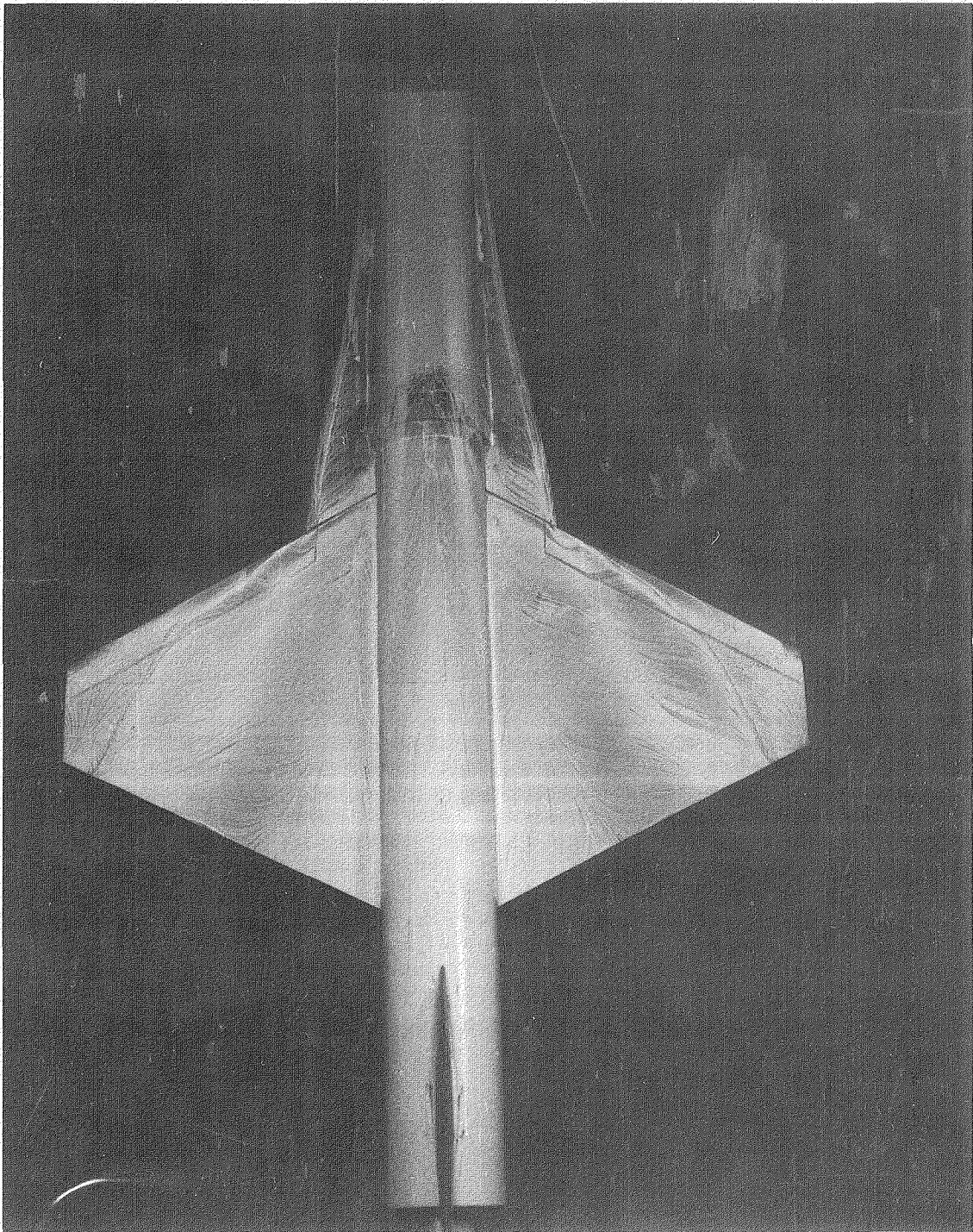
L-79-215

(b) $\alpha = 10^{o}$.

Figure 7.- Continued.

L-79-216

(c) $\alpha = 15^{o}$.

Figure 7.- Continued.

40

L-79-217

(d) $\alpha = 20^{\circ}$.

Figure 7.- Continued.

L-79-218

(e) $\alpha = 25^O$.

Figure 7.- Continued.

L-79-219

(f) $\alpha = 30^O$.
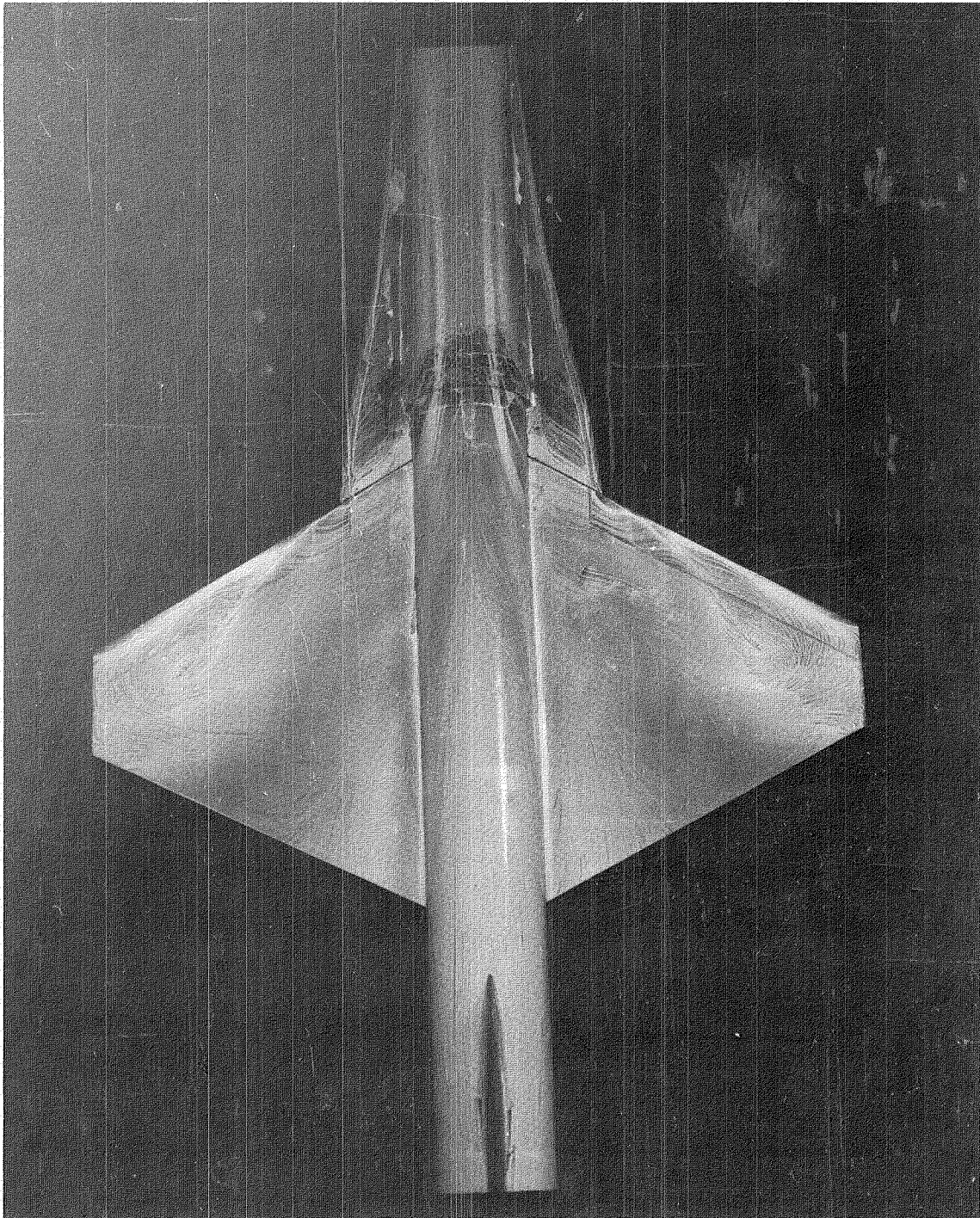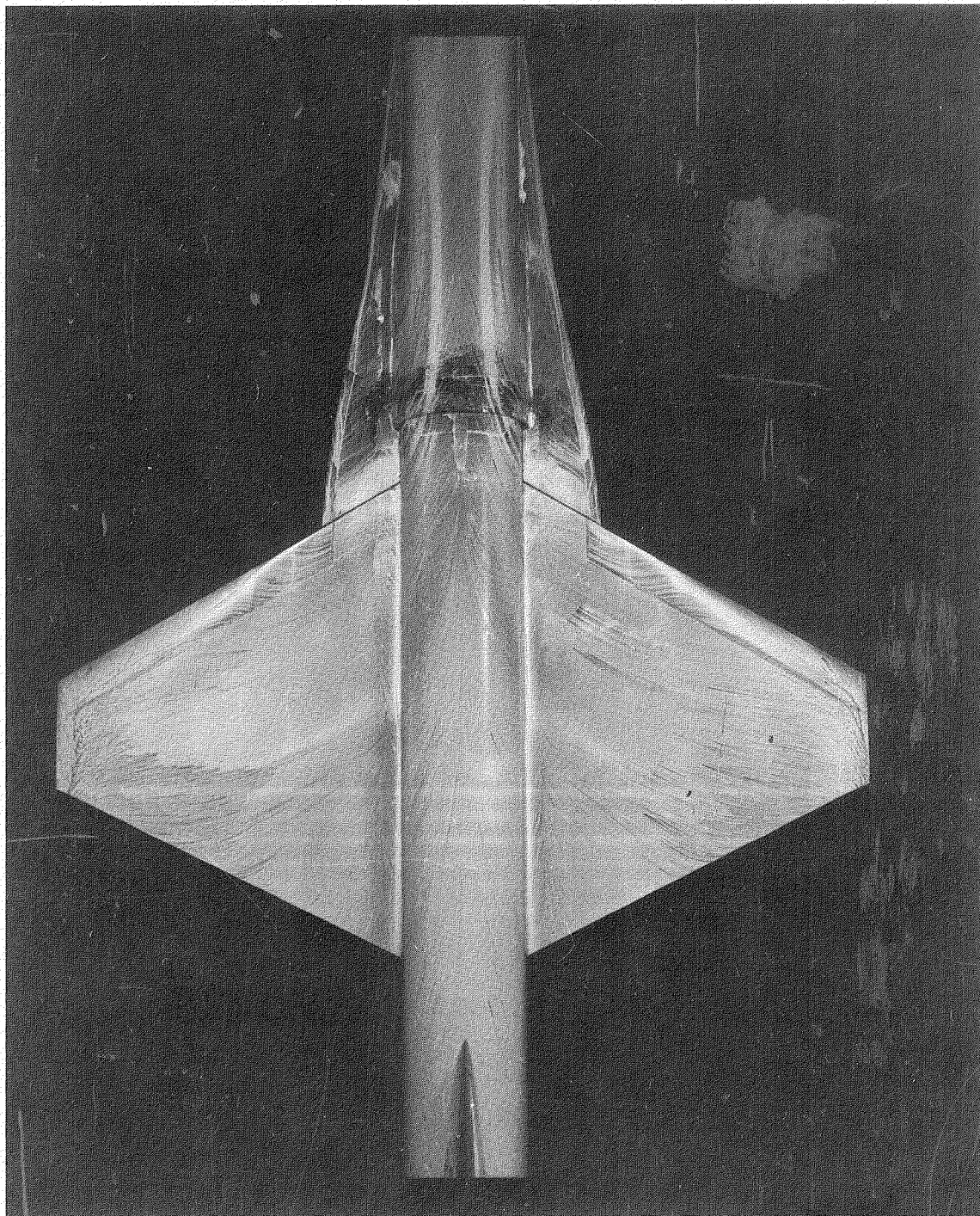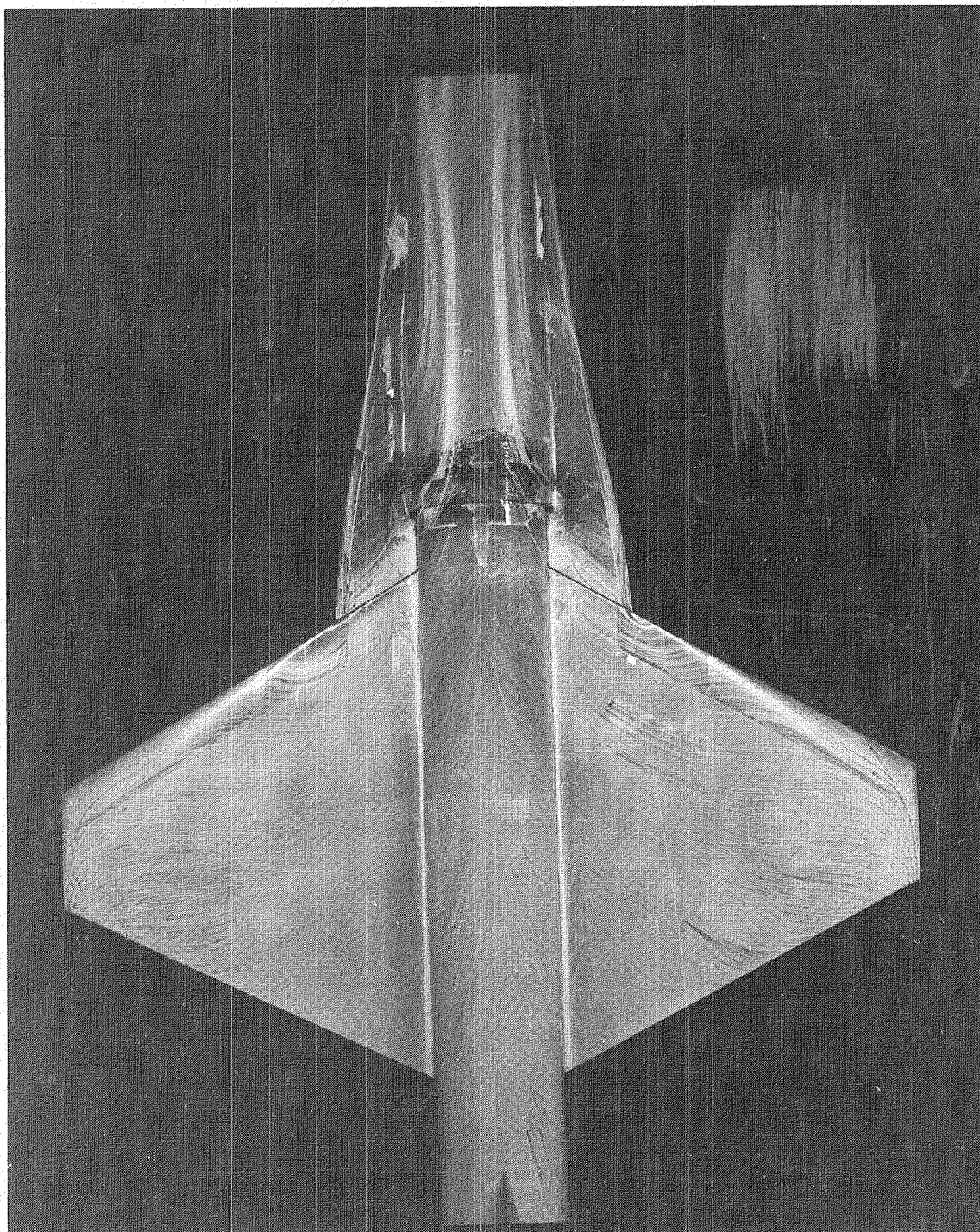
Figure 7.- Concluded.

43

L-79-220

(a) $\alpha = 5^o$.
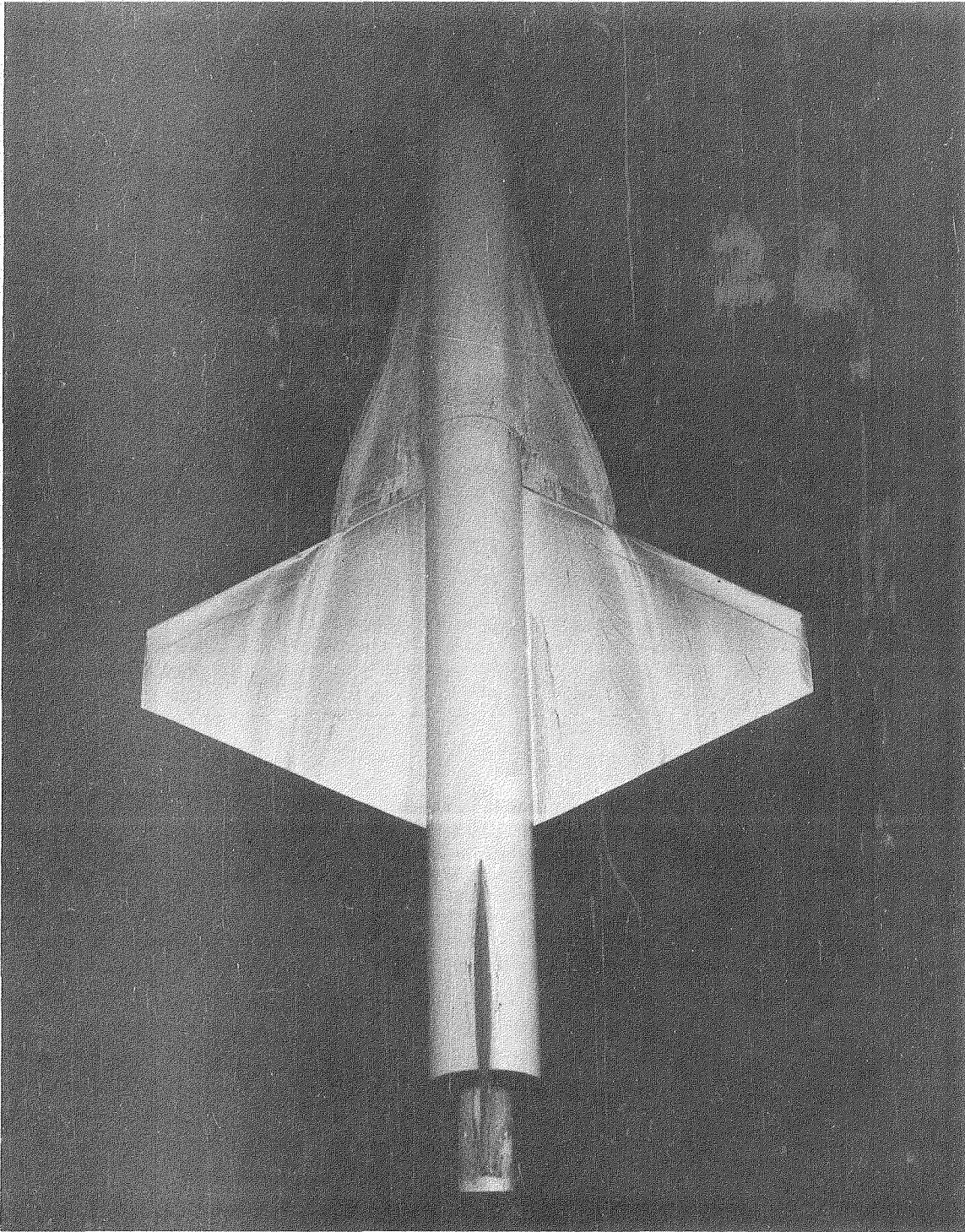
Figure 8.- Surface flow patterns for configuration 30-3, with gap sealed, at $M_\infty = 0.3$.

(b) $\alpha = 10^{\circ}$.
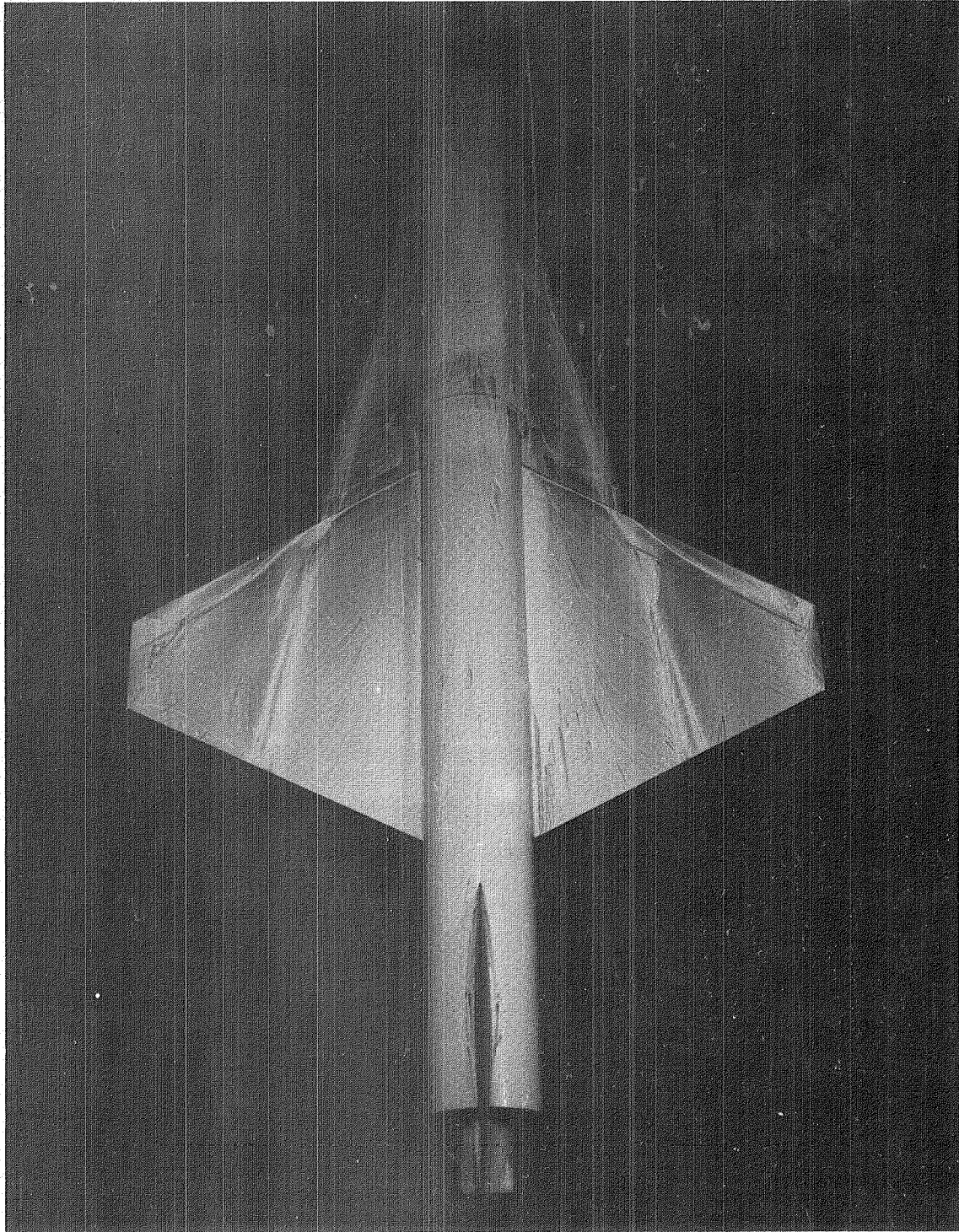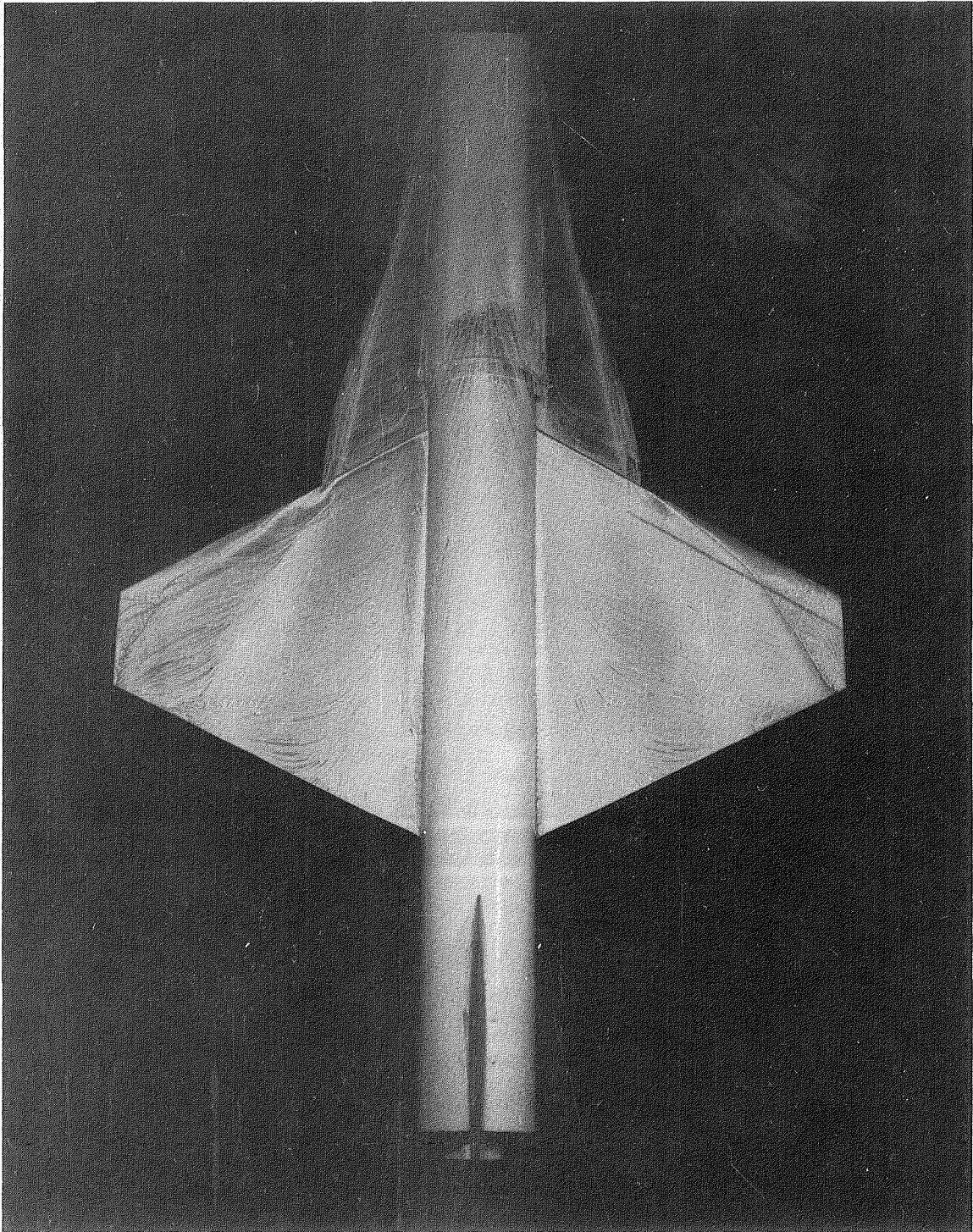
Figure 8.- Continued.

(c) $\alpha = 15^{\circ}$.

L-79-222

Figure 8.- Continued.

(d) $\alpha = 20^\circ$.
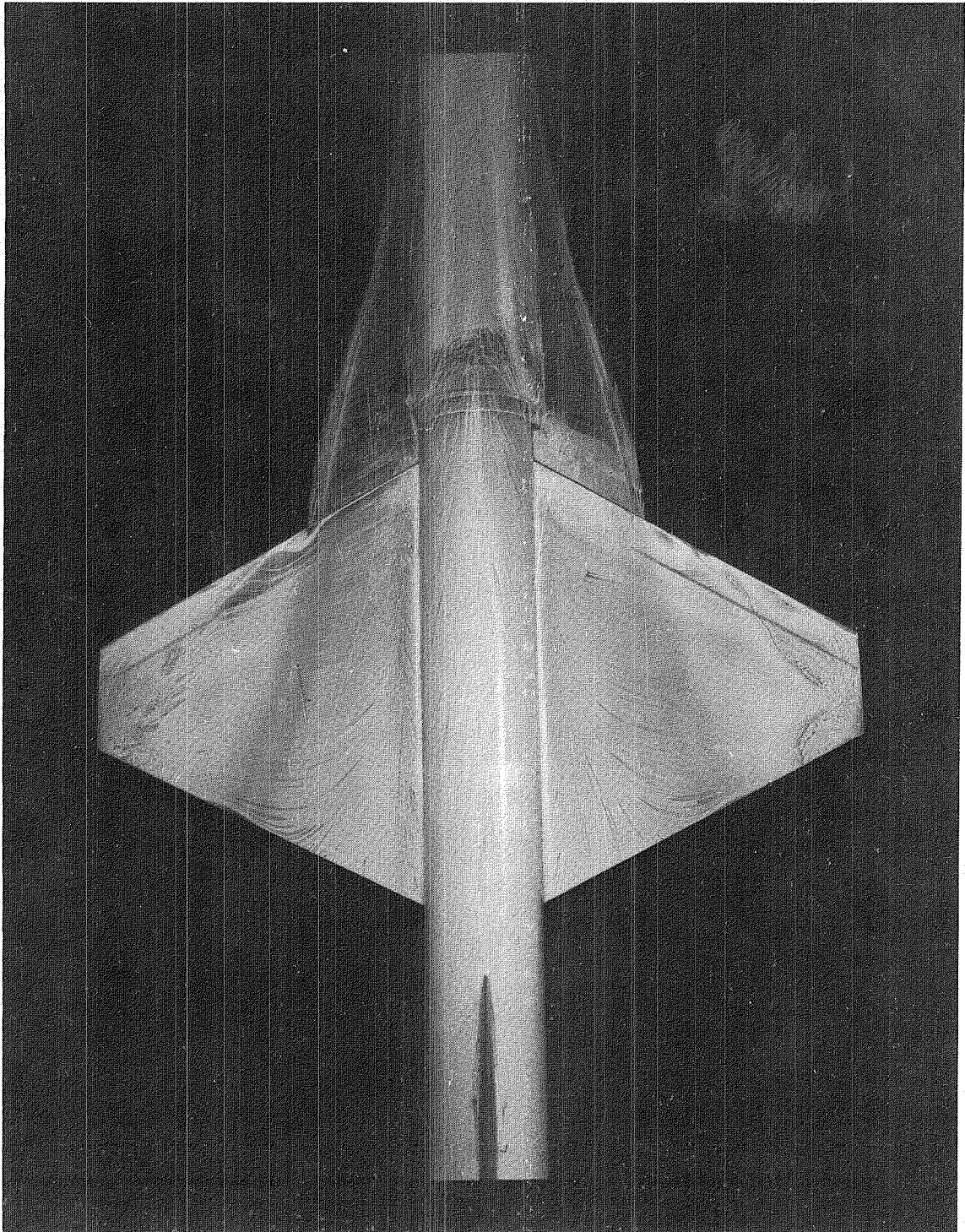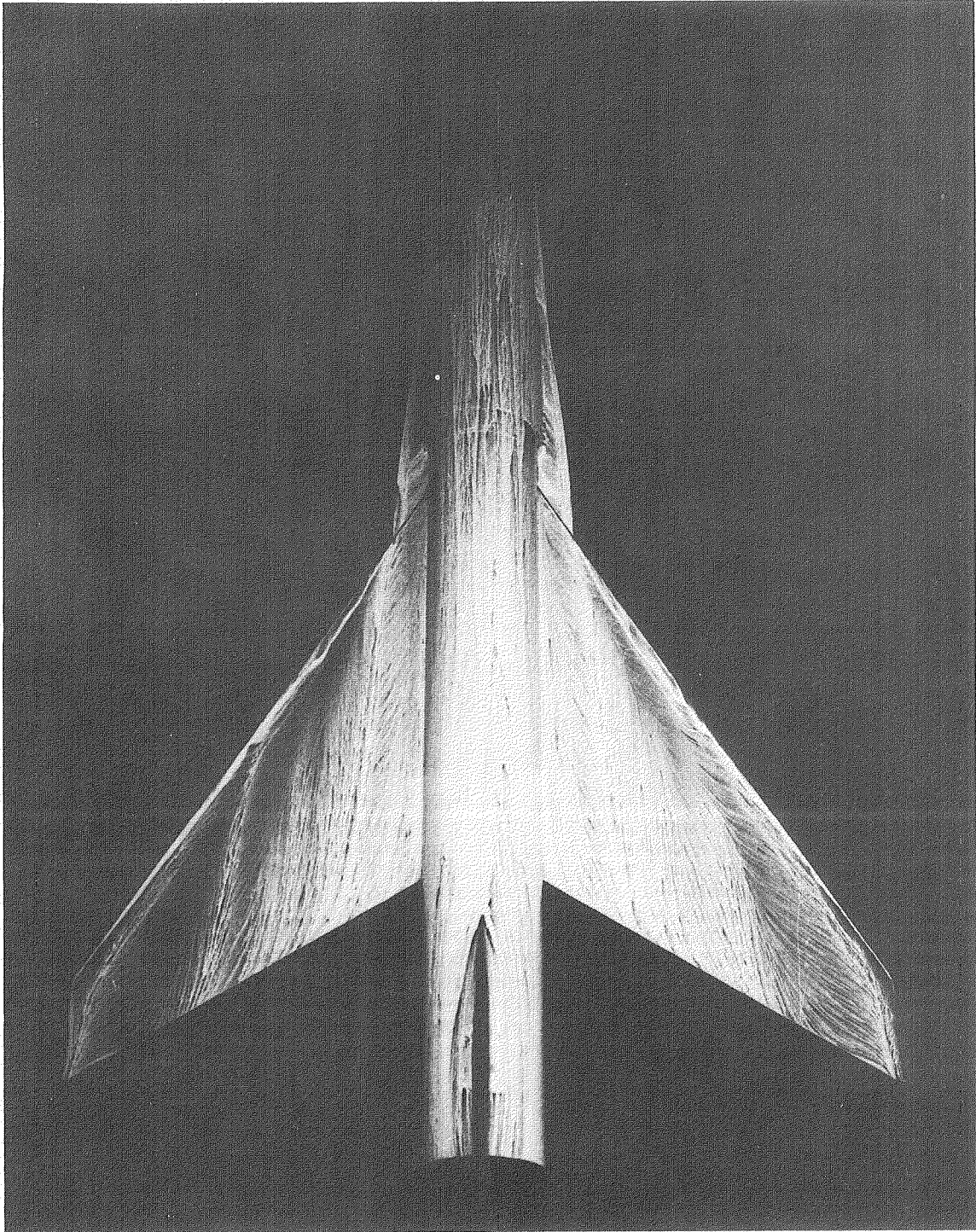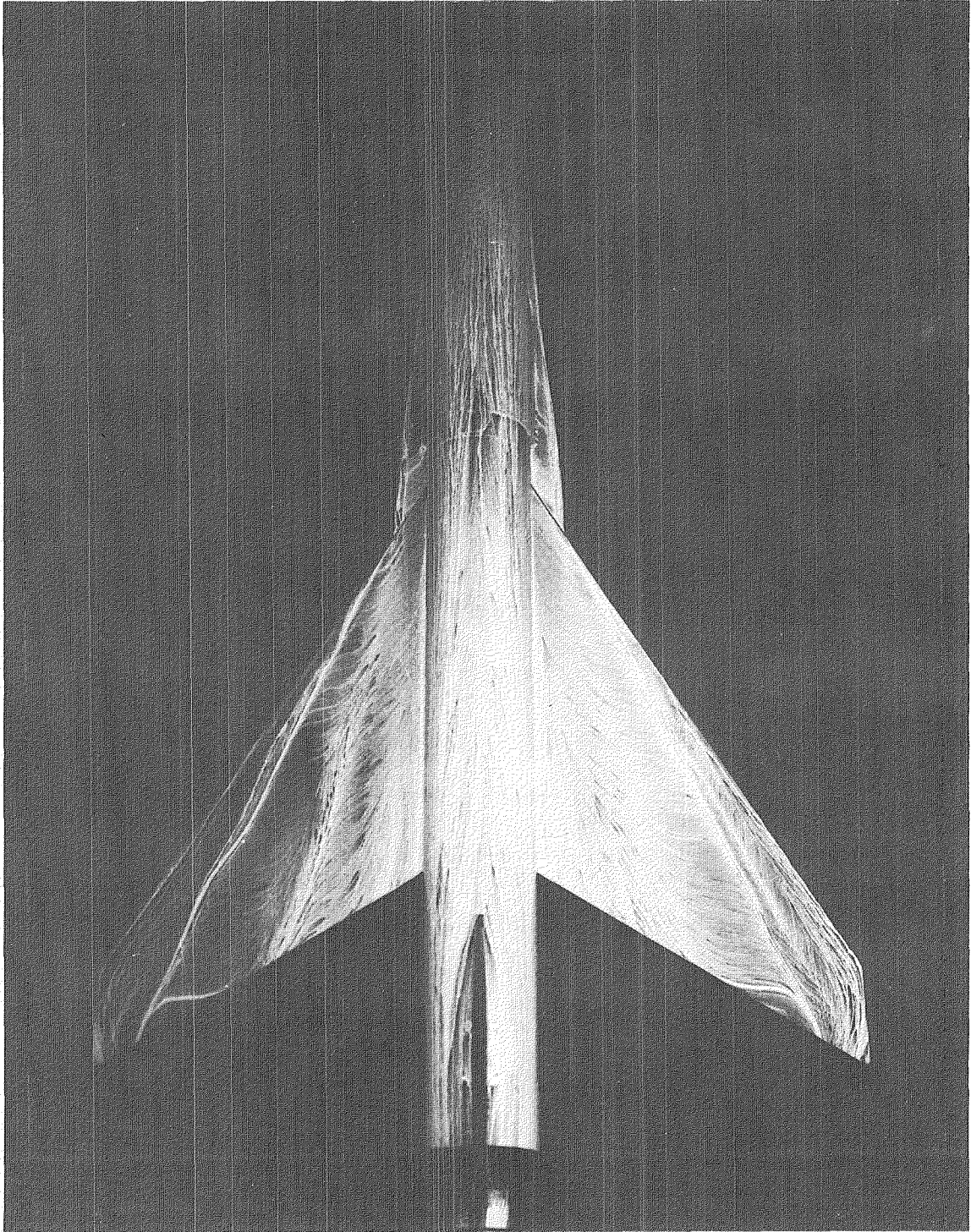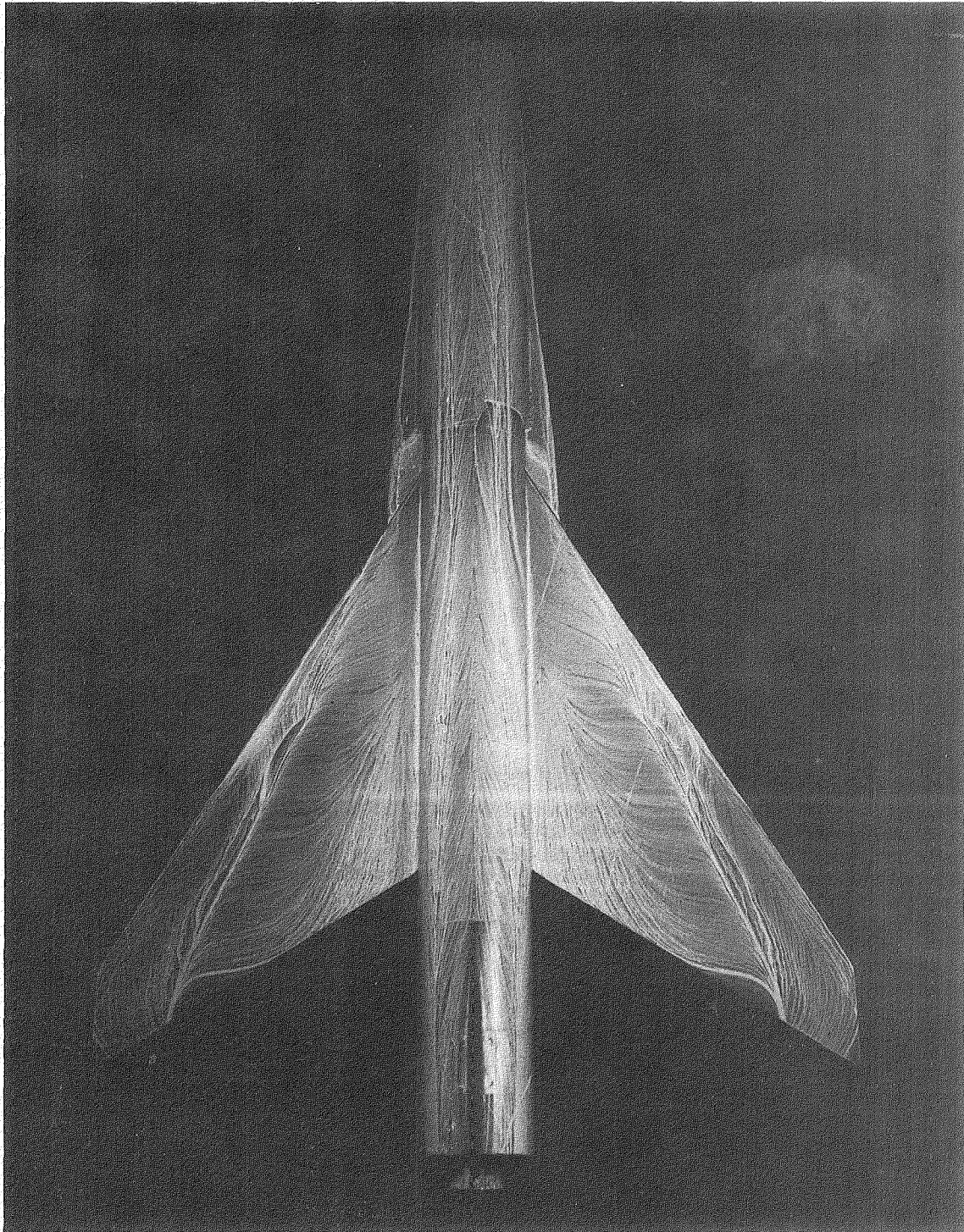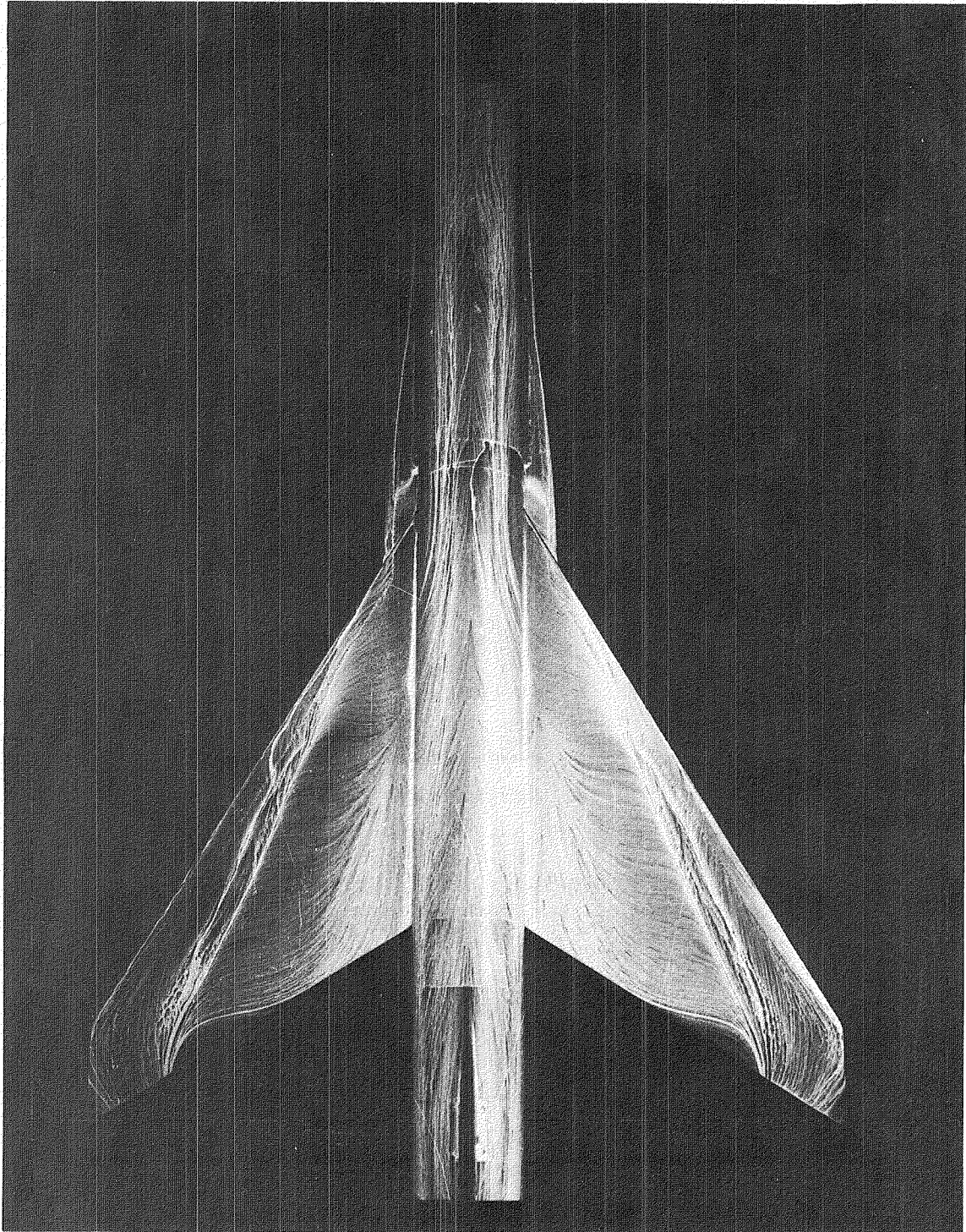
Figure 8.- Continued.

(e) $\alpha = 25^{\circ}$.
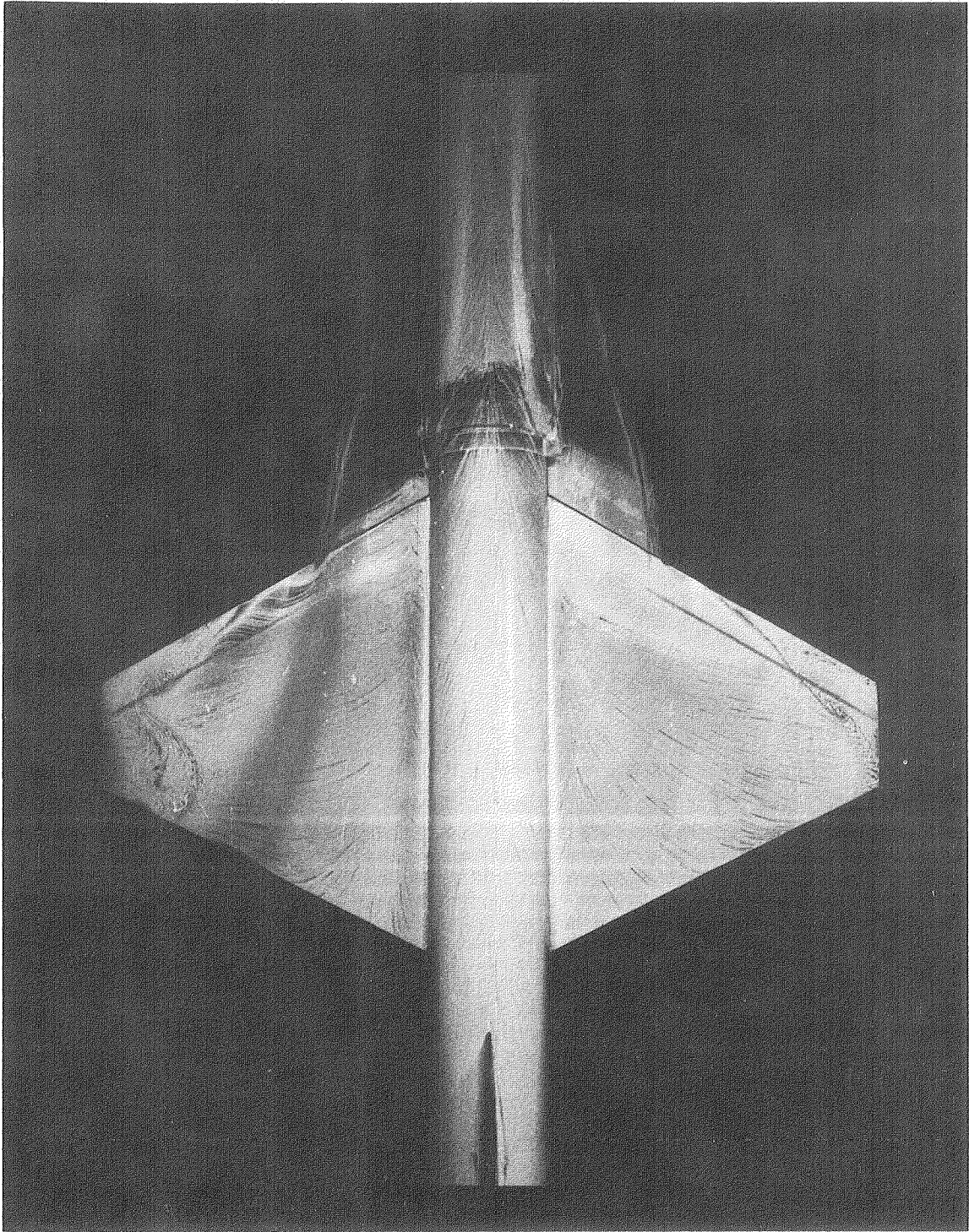
Figure 8.- Continued.

(f) $\alpha = 30°$.
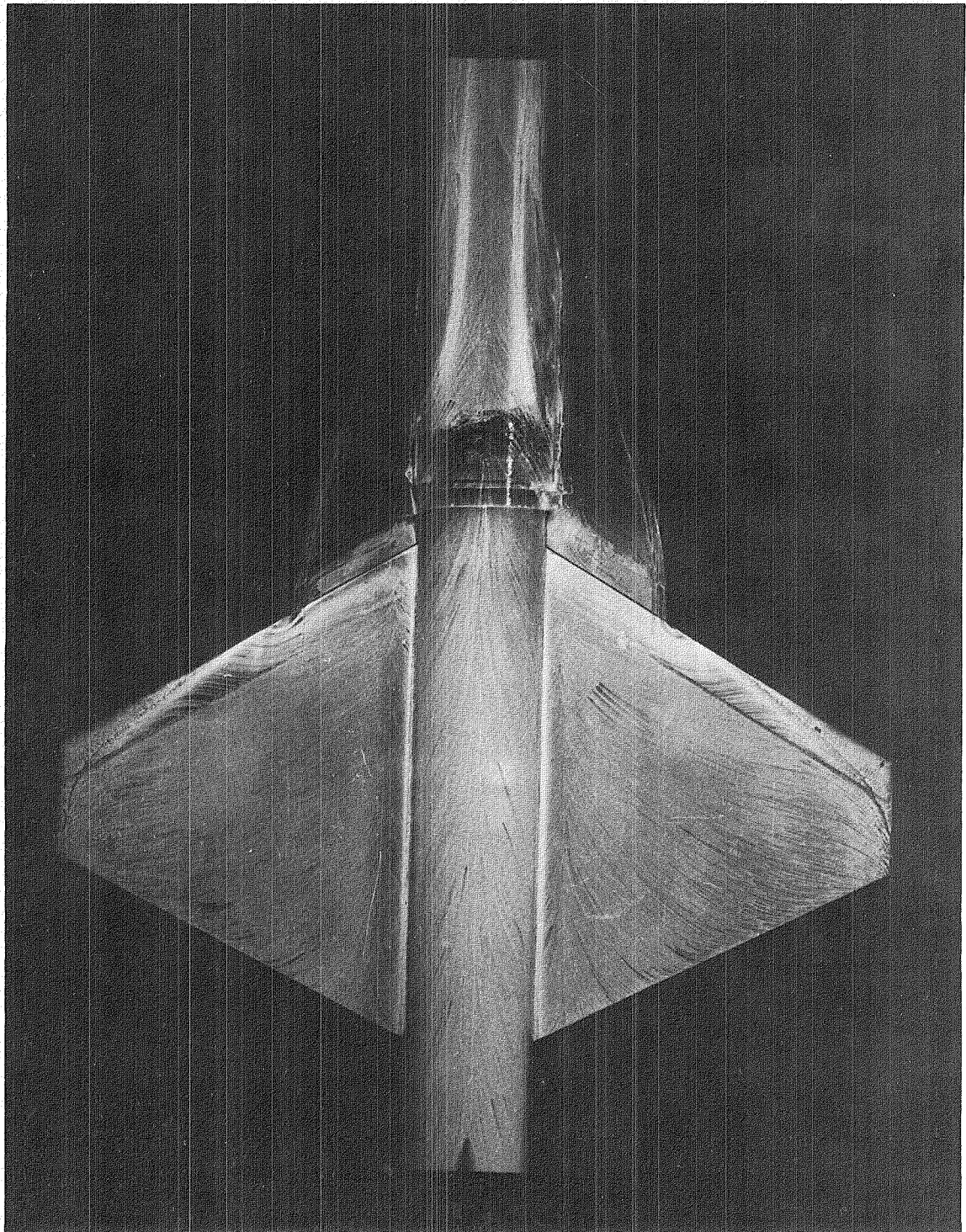
Figure 8.- Concluded.

L-79-225

L-79-226

(a) $\alpha = 5^{\circ}$.
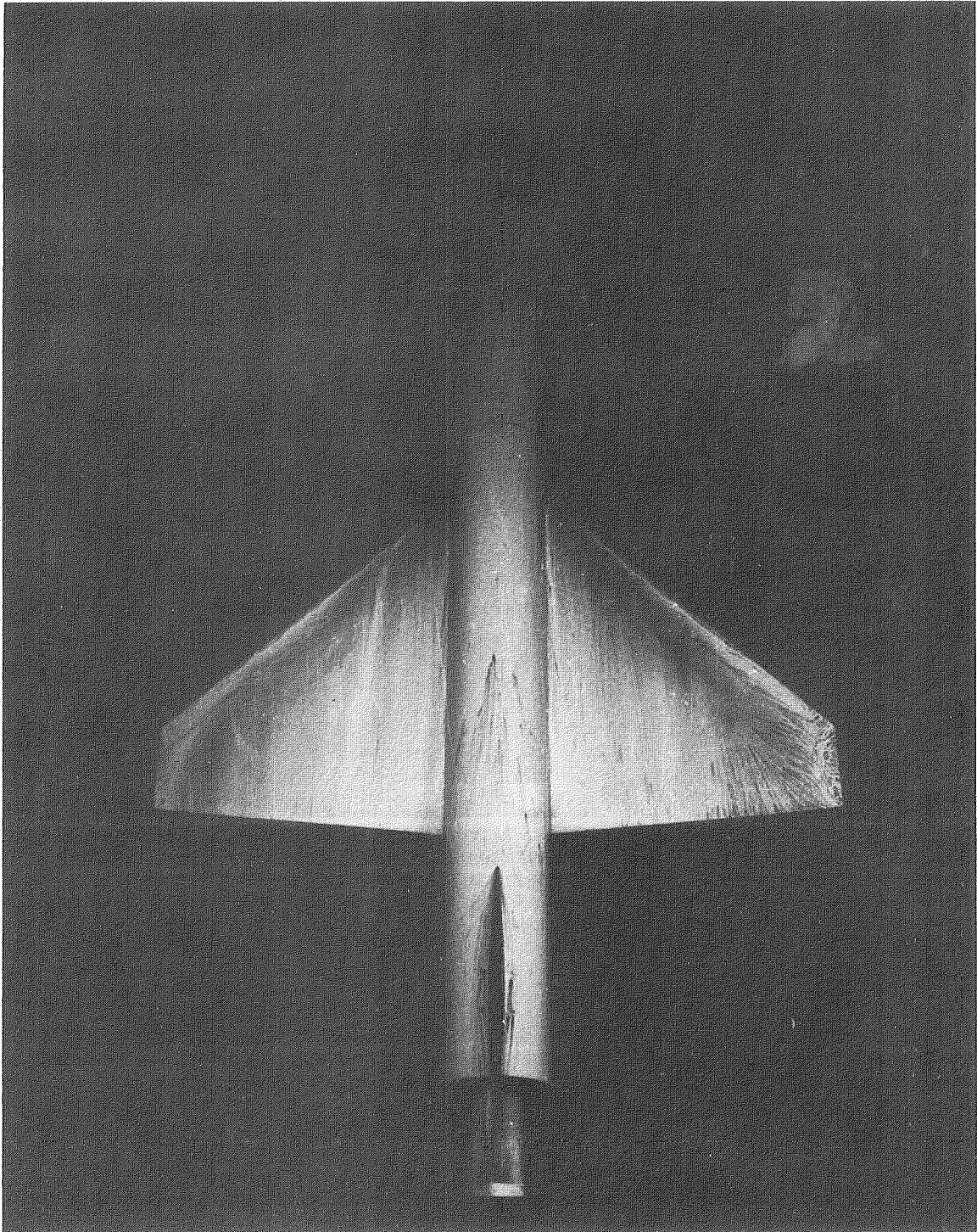
Figure 9.- Surface flow patterns for configuration 44-0 at $M_\infty = 0.3$.
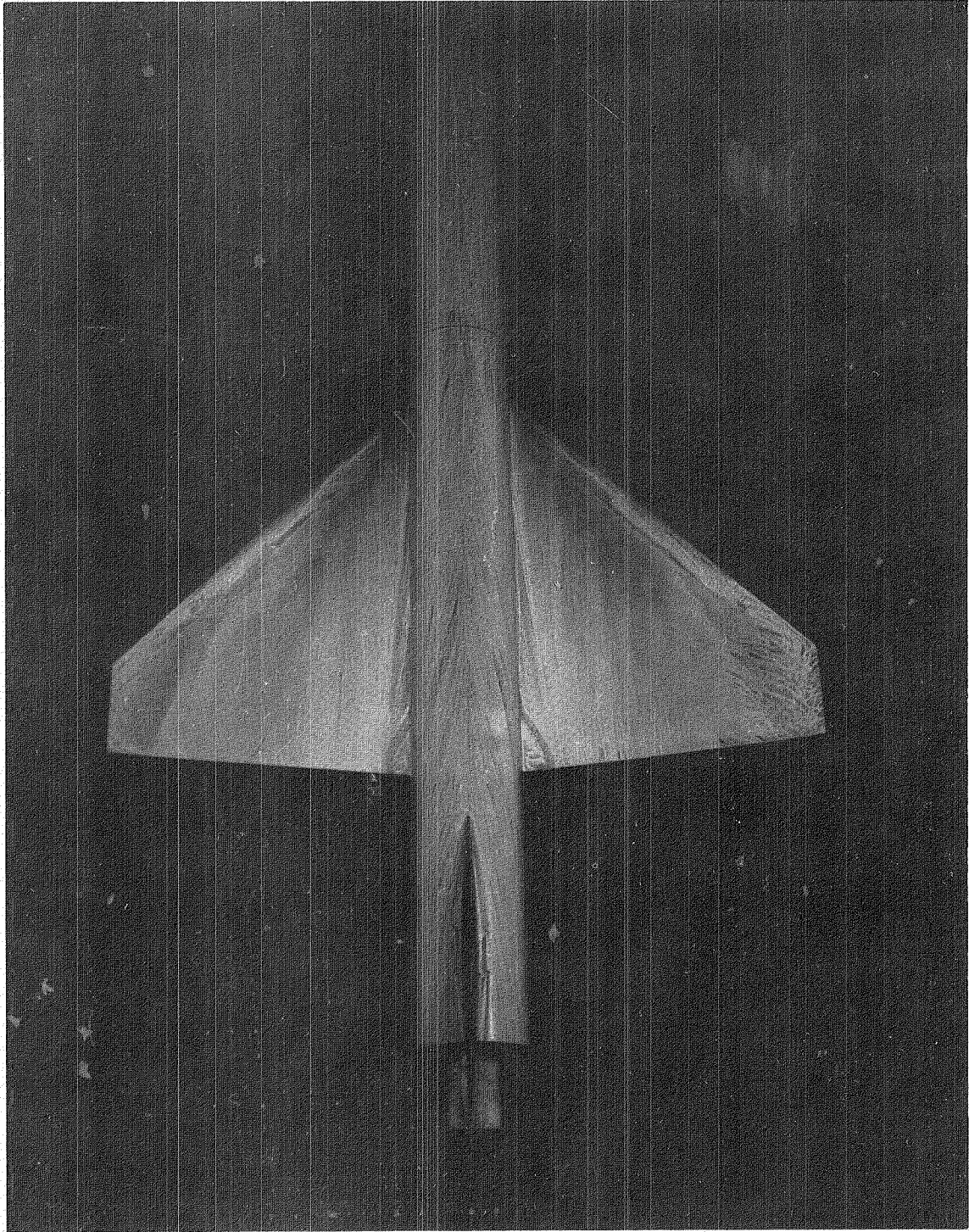
50

L-79-227

(b) $\alpha = 10^{O}$.

Figure 9.- Continued.

L-79-228

(c) $\alpha = 15^{\text{o}}$.
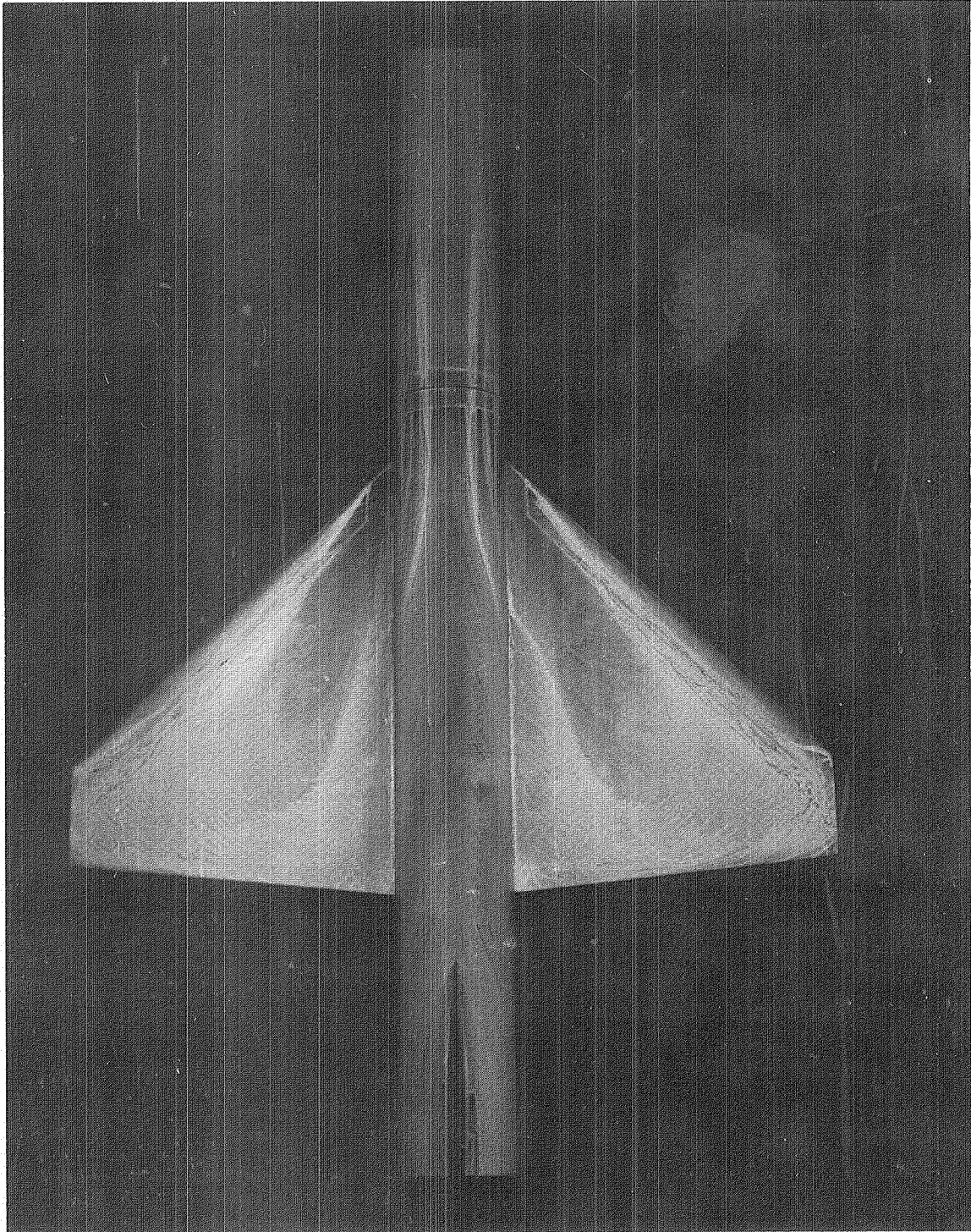
Figure 9.- Continued.

L-79-229
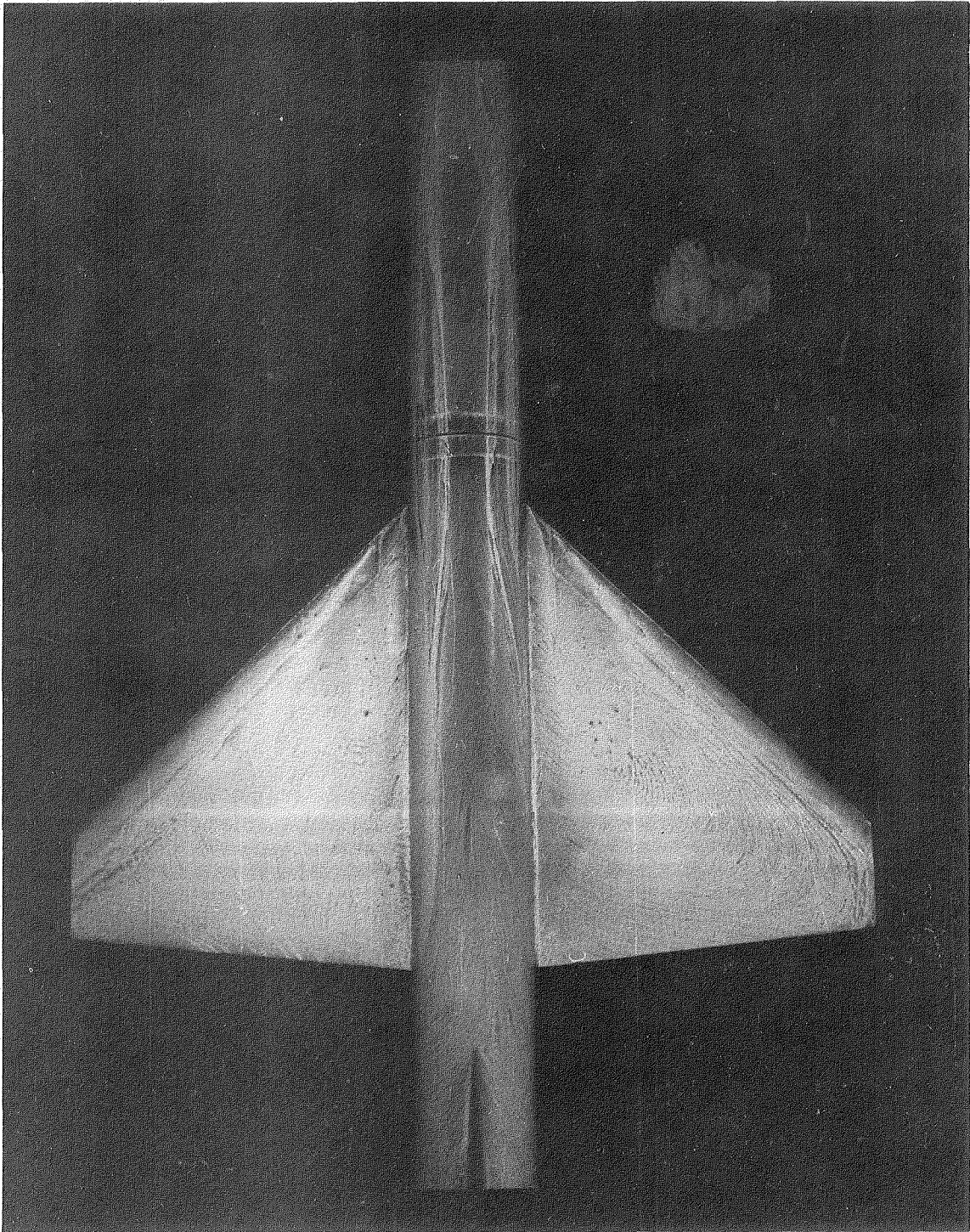
(d) $\alpha = 20^{\circ}$.

Figure 9.- Continued.

53

L-79-230

(e) $\alpha = 25^{\circ}$.

Figure 9.- Continued.

(f) $\alpha = 30^{O}$.
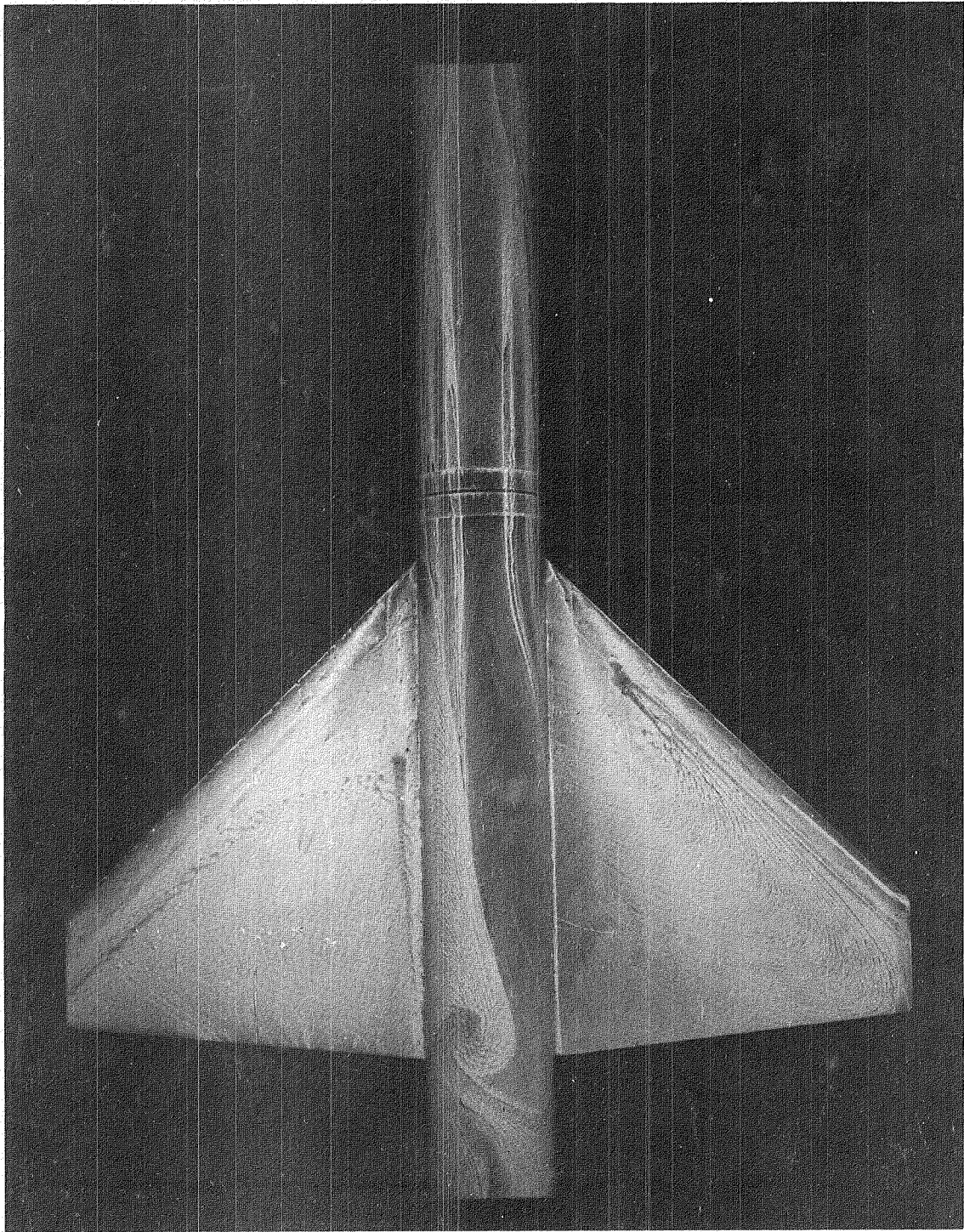
Figure 9.- Concluded.
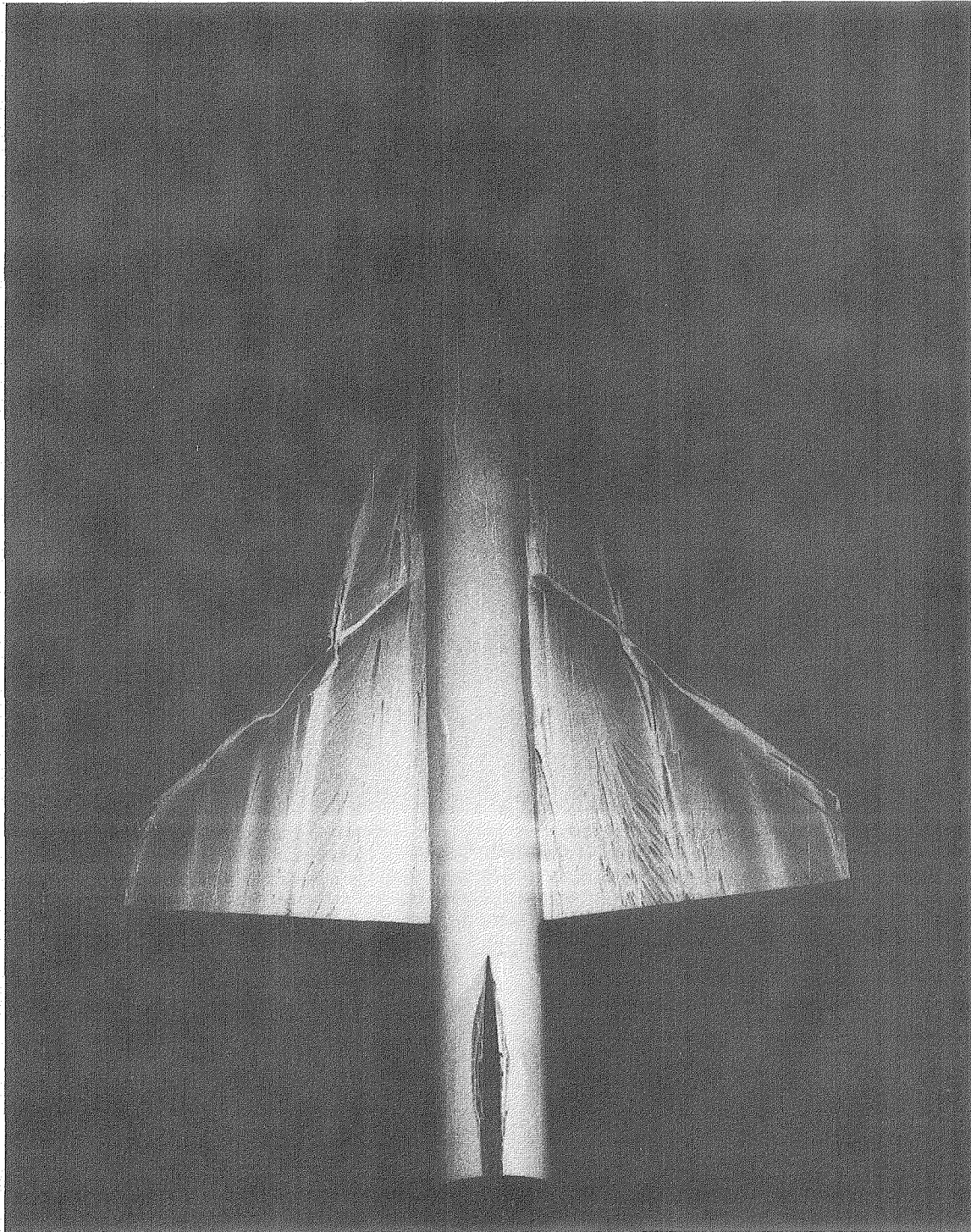
L-79-232

(a) $\alpha = 5^{\circ}$.

Figure 10.- Surface flow patterns for configuration 44-3, with gap sealed, at $M_{\infty} = 0.3$.

L-79-233

(b) $\alpha = 10^{\circ}$.

Figure 10.- Continued.

57

L-79-234

(c) $\alpha = 15^{\rm o}$.
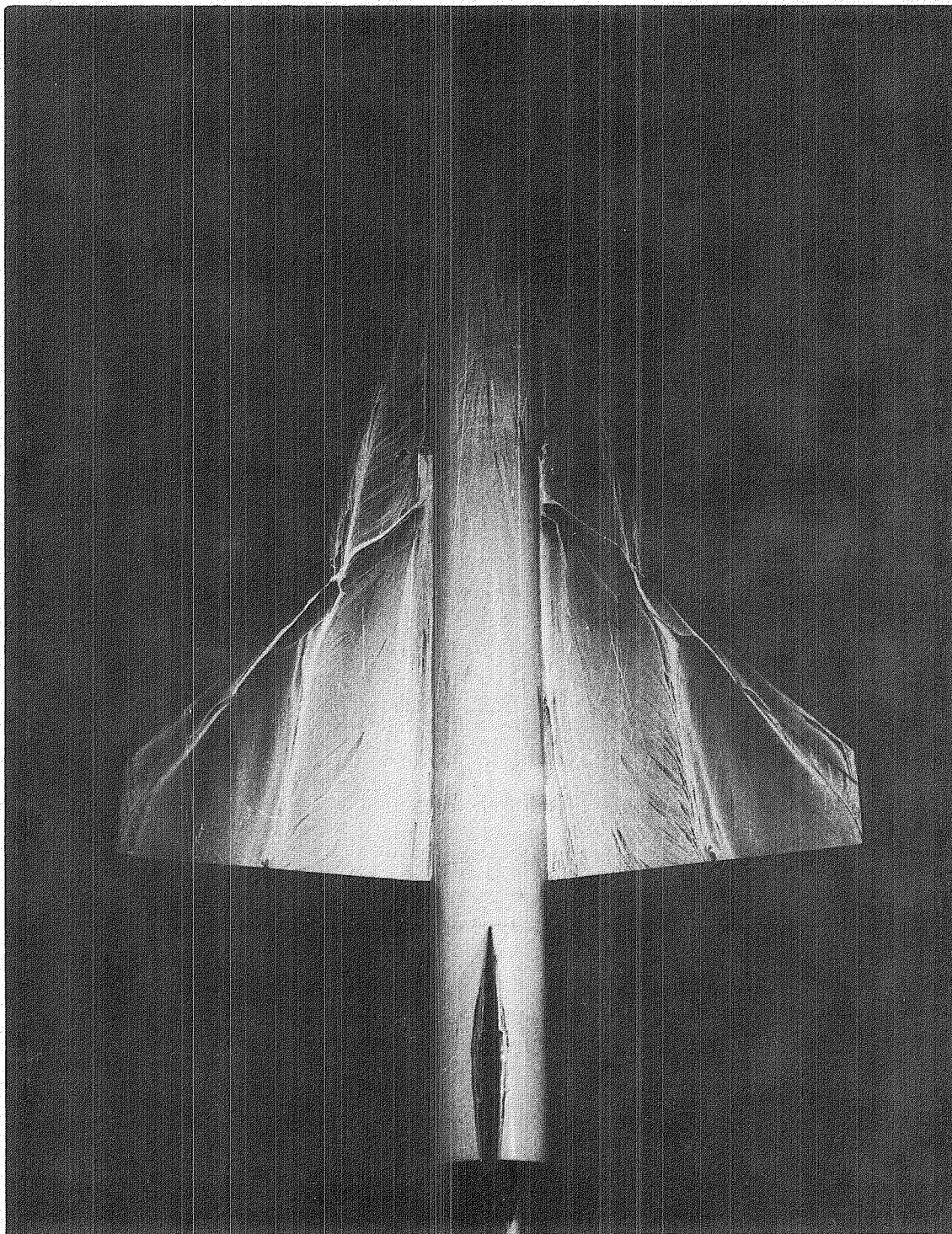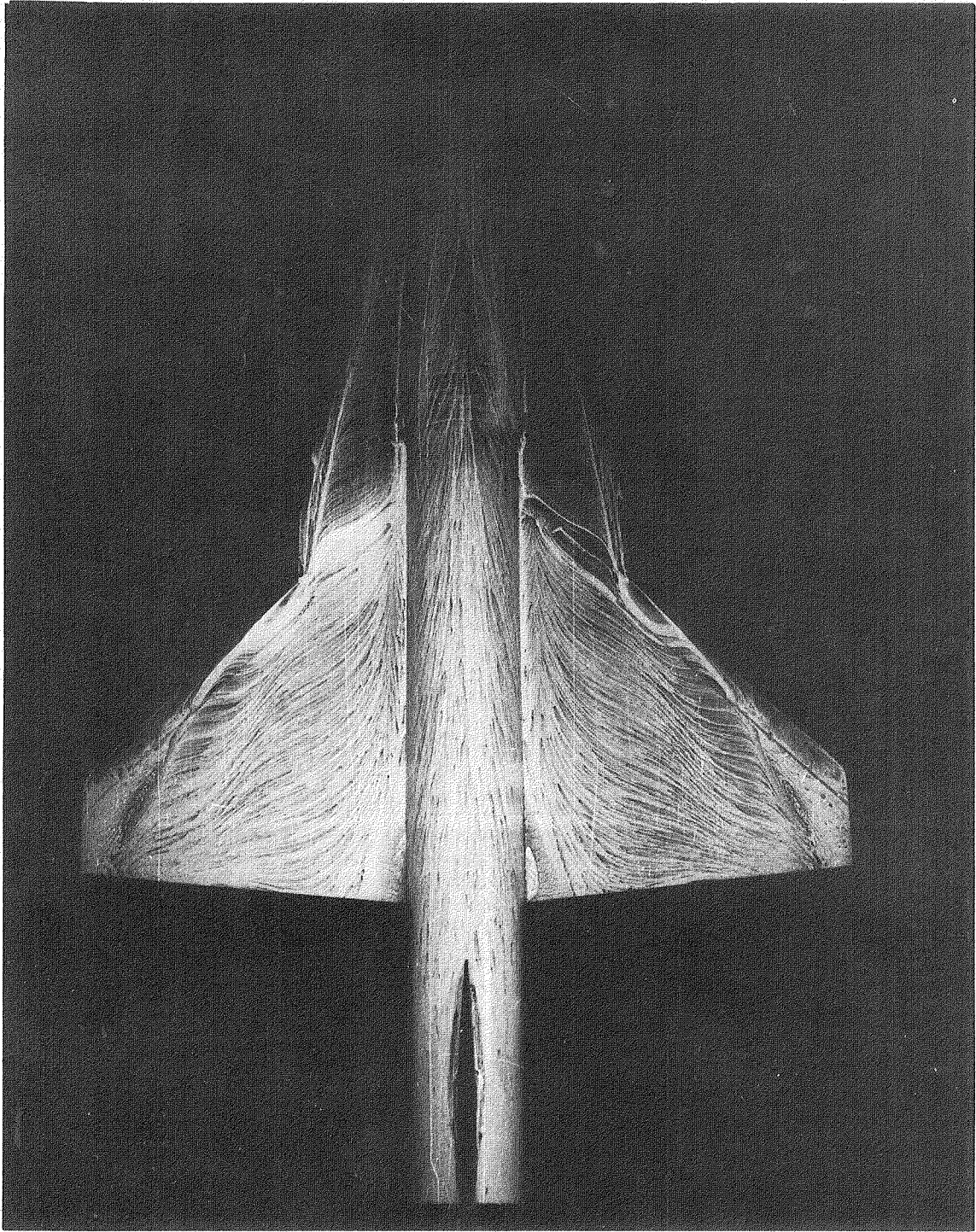
Figure 10.- Continued.

(d) $\alpha = 20°$.

Figure 10.- Continued.
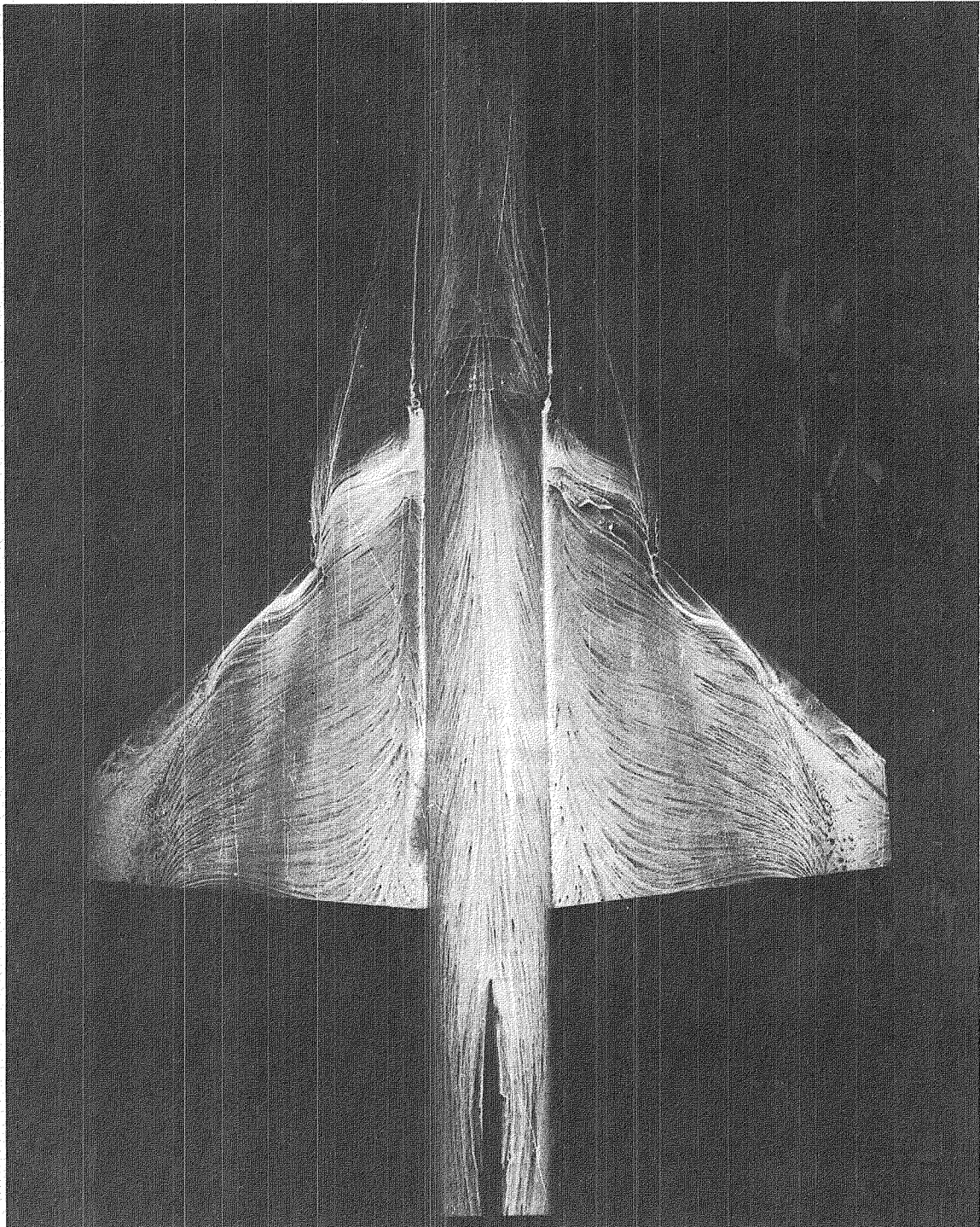
L-79-236

(e) $\alpha = 25^{\circ}$.

Figure 10.- Continued.

L-79-237

(f) $\alpha = 30^{\circ}$.
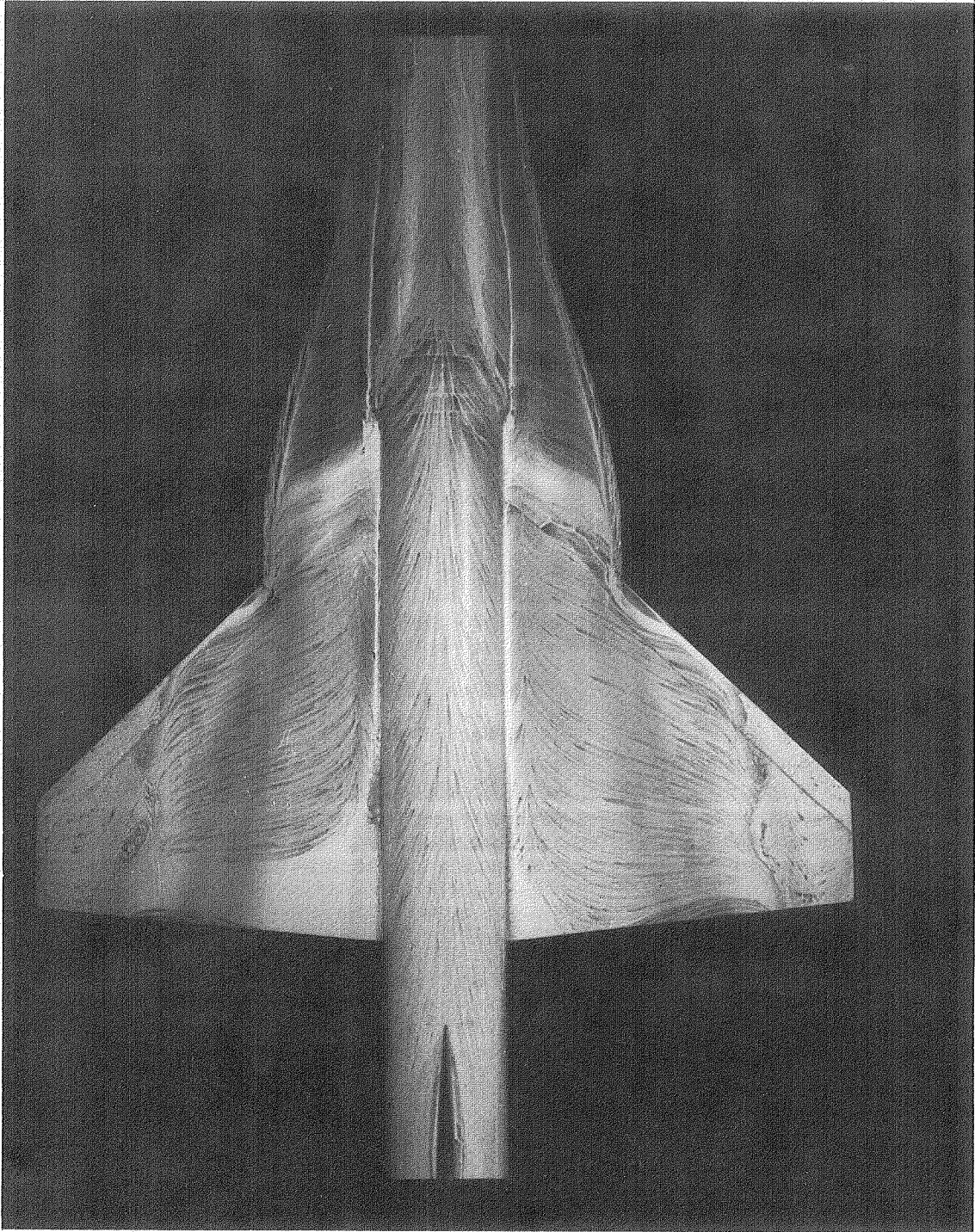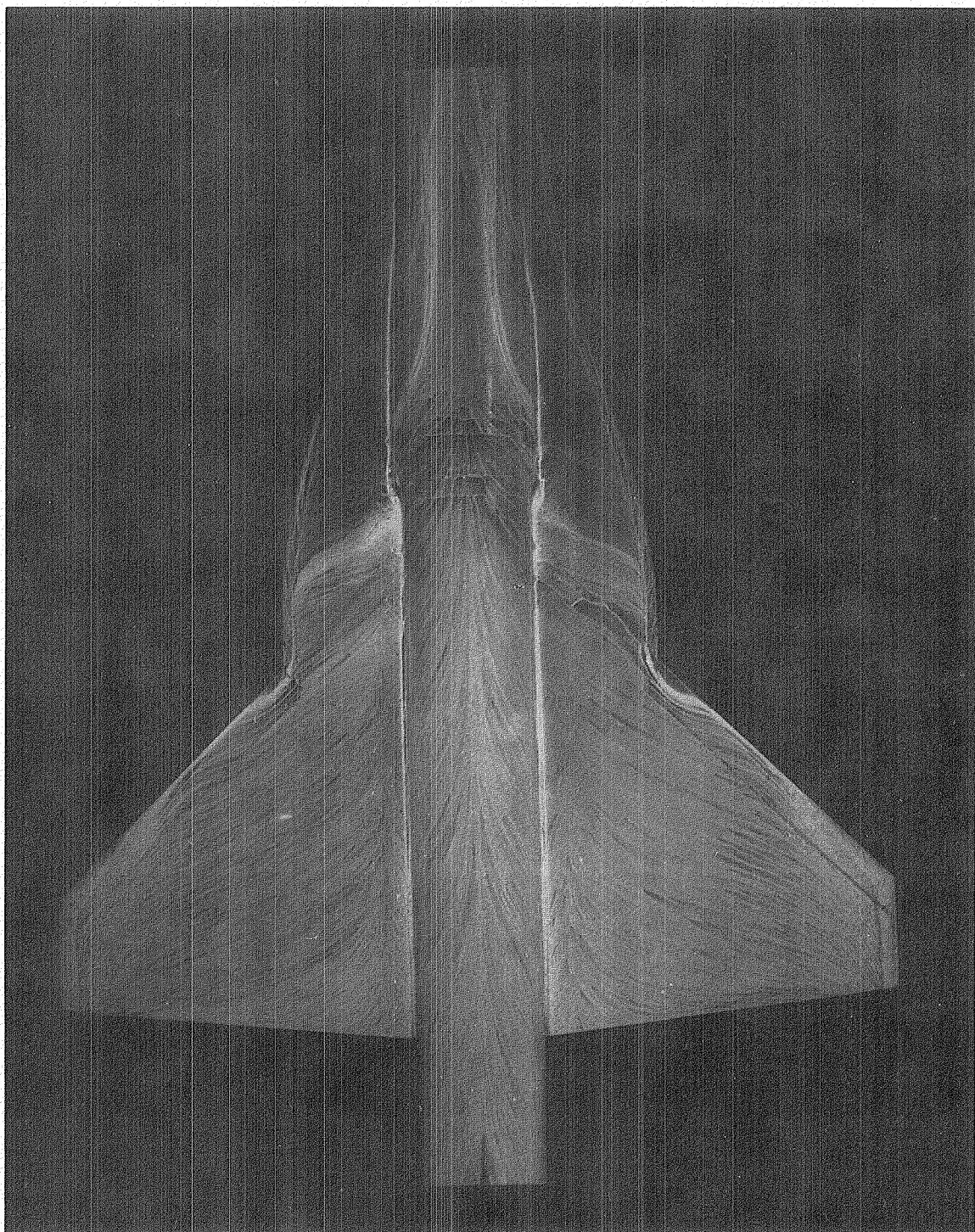
Figure 10.- Concluded.
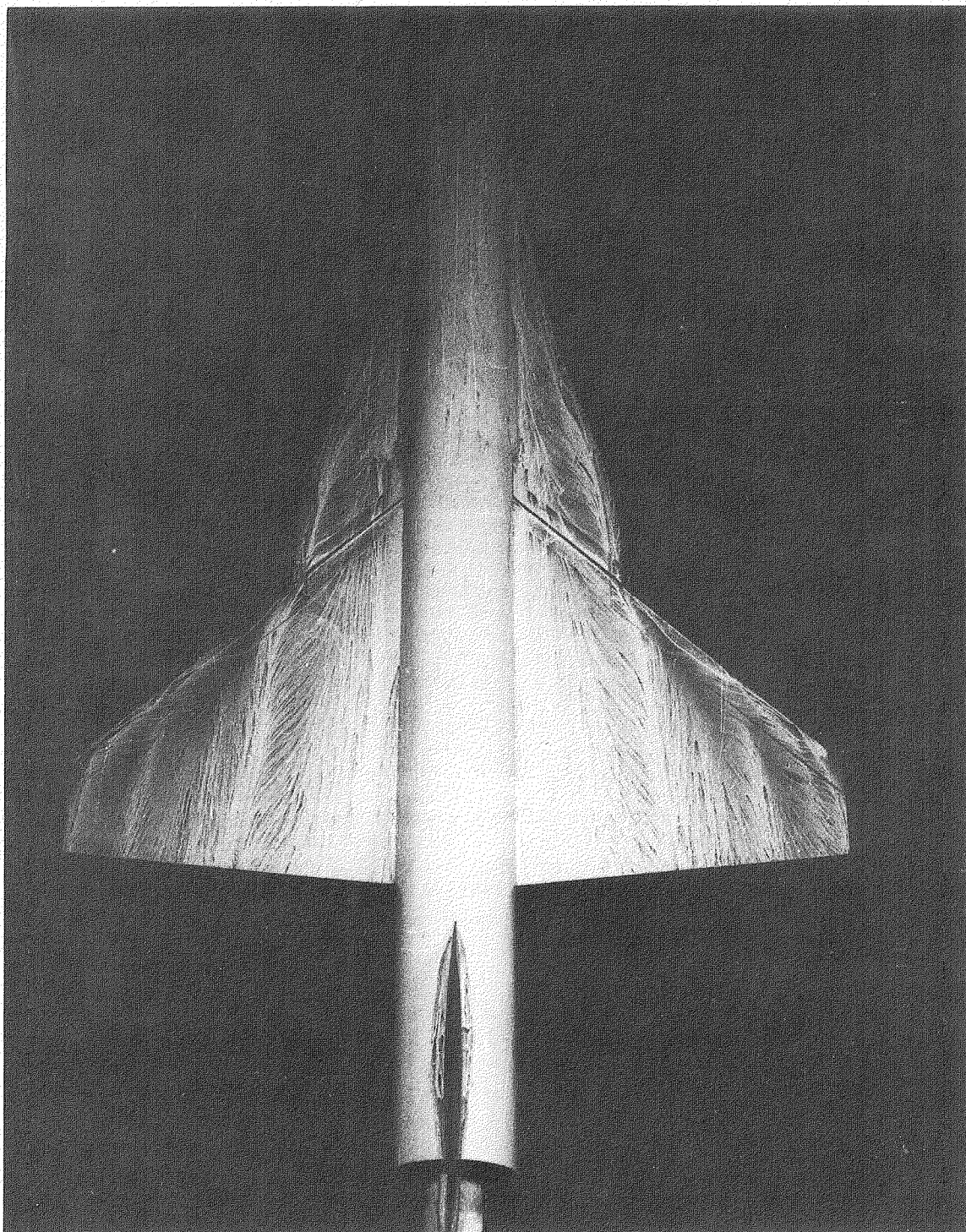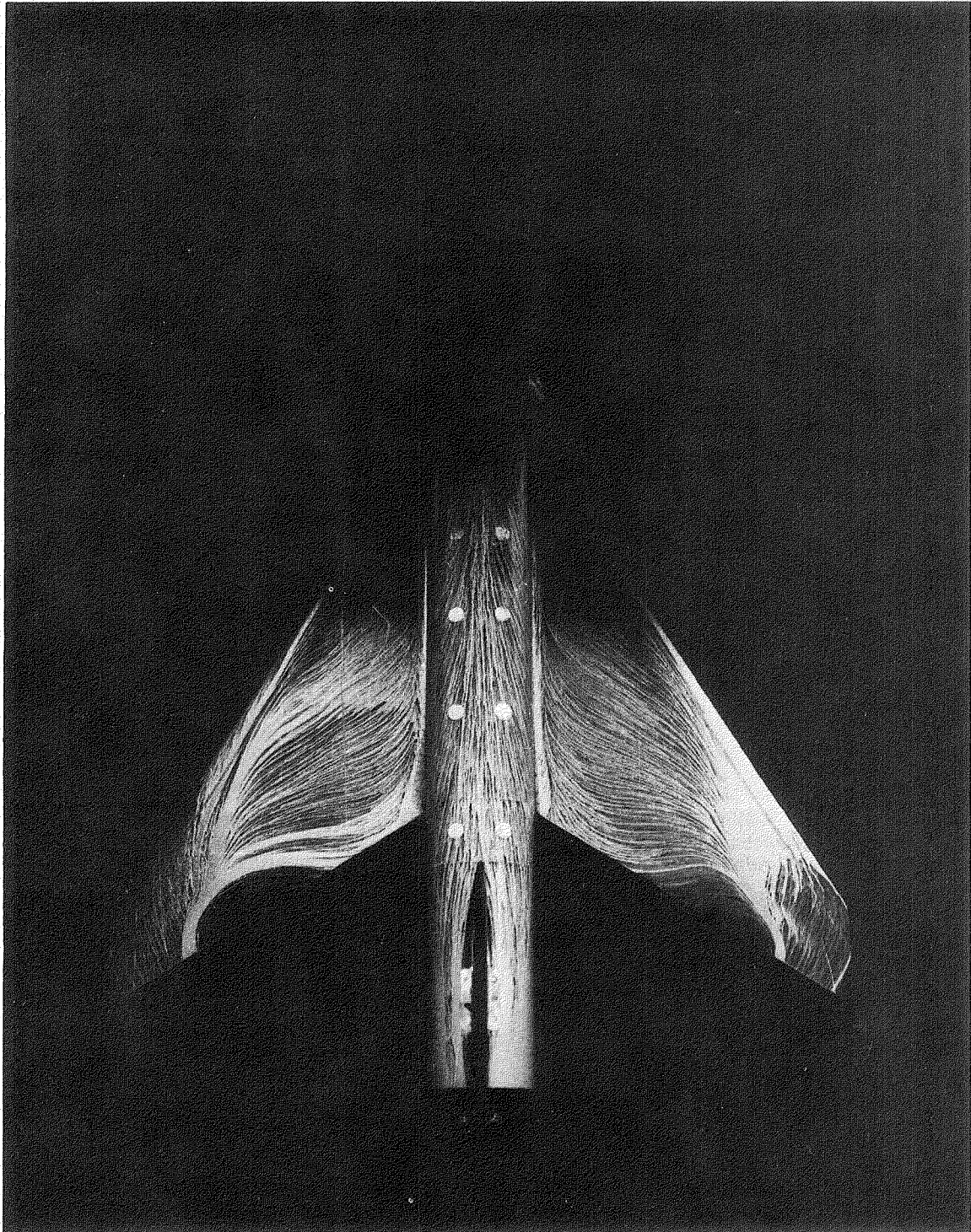
L-79-238

(a) $\alpha = 5^{\circ}$.

Figure 11.- Surface flow patterns for configuration 44-3, with gap open,
at $M_{\infty} = 0.3$.
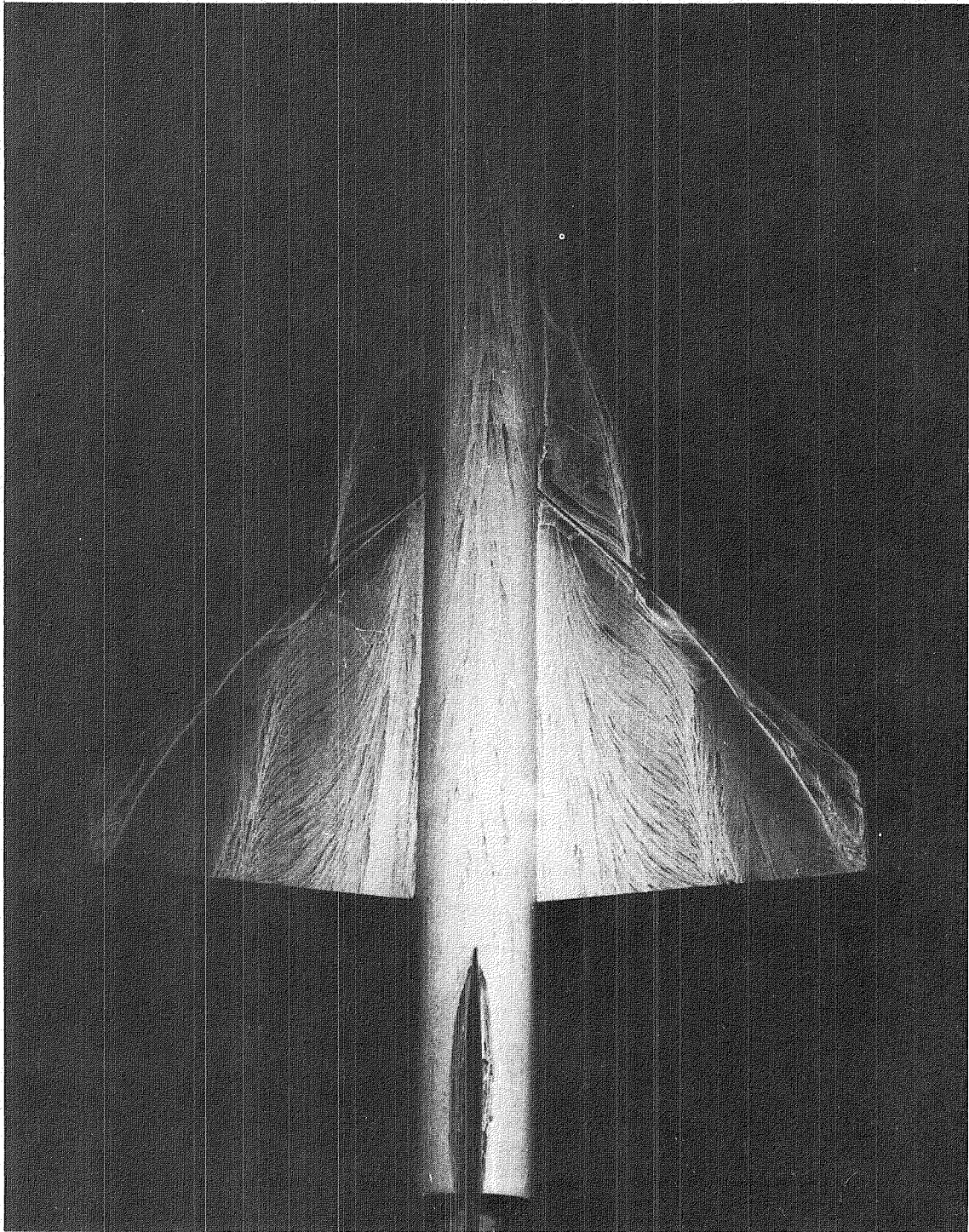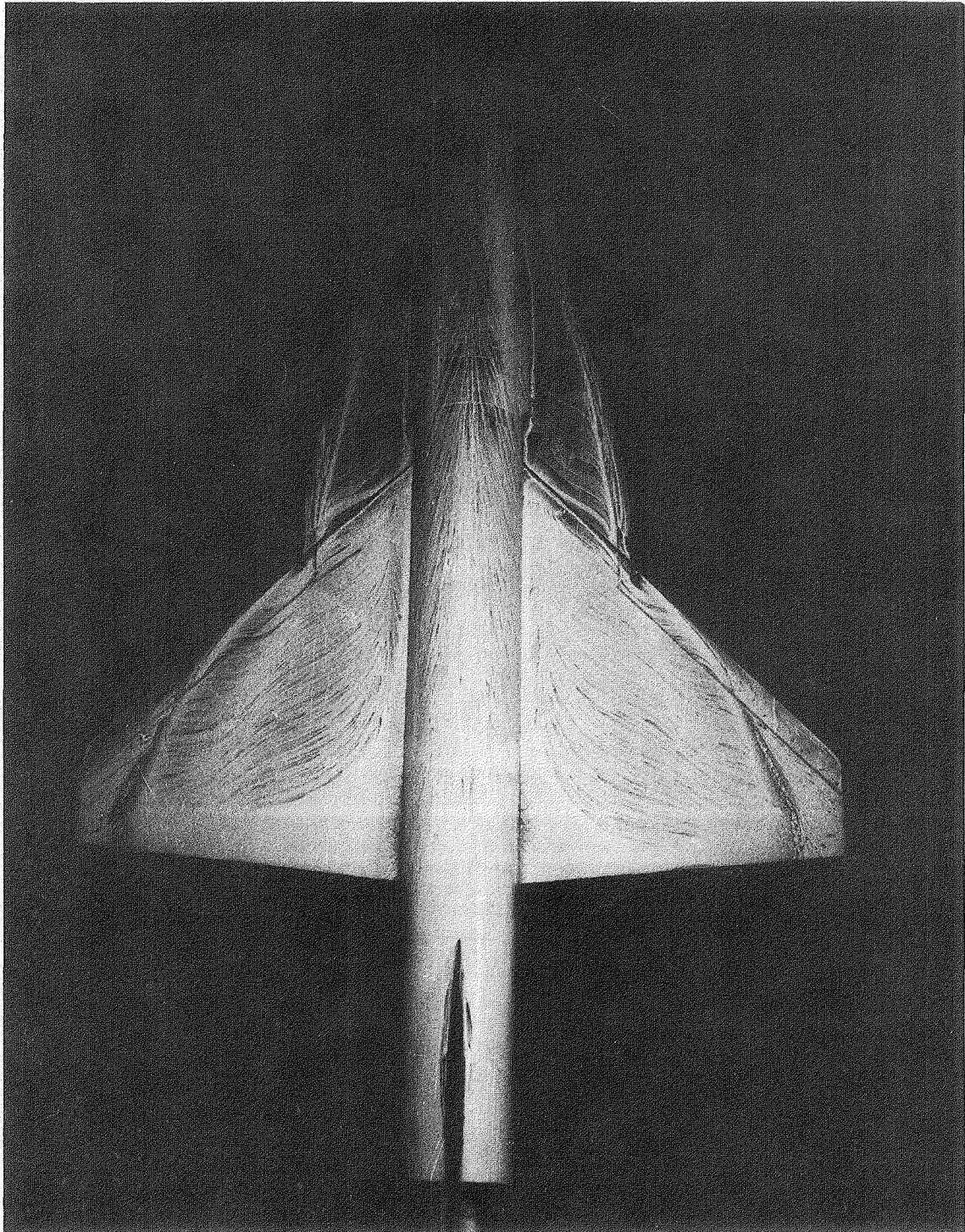
62
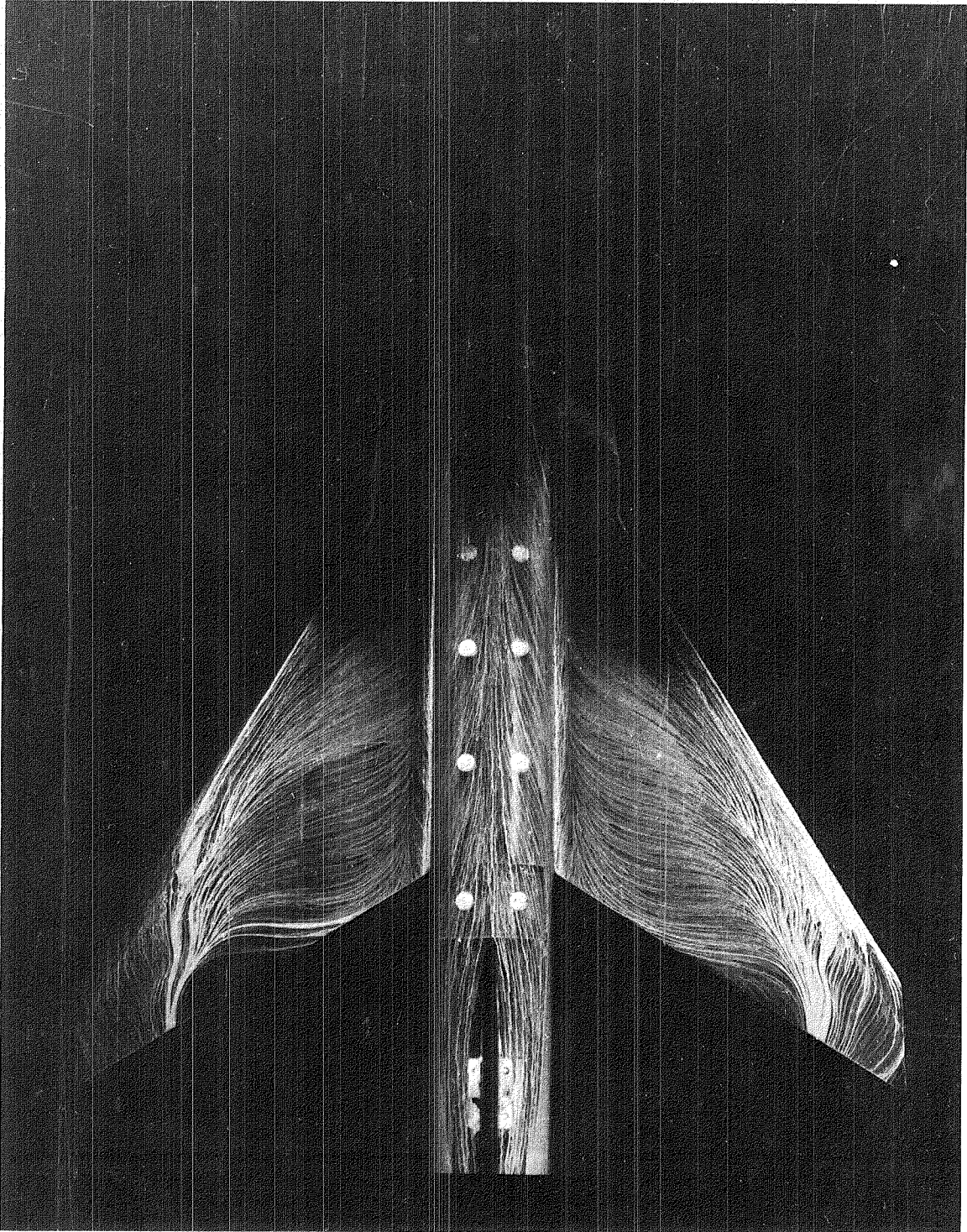
L-79-239

(b) $\alpha = 10^{\circ}$.

Figure 11.- Continued.

63

L-79-240

(c) $\alpha = 15^\circ$.

Figure 11.- Continued.

L-79-241

(d) $\alpha = 20°$.

Figure 11.- Continued.
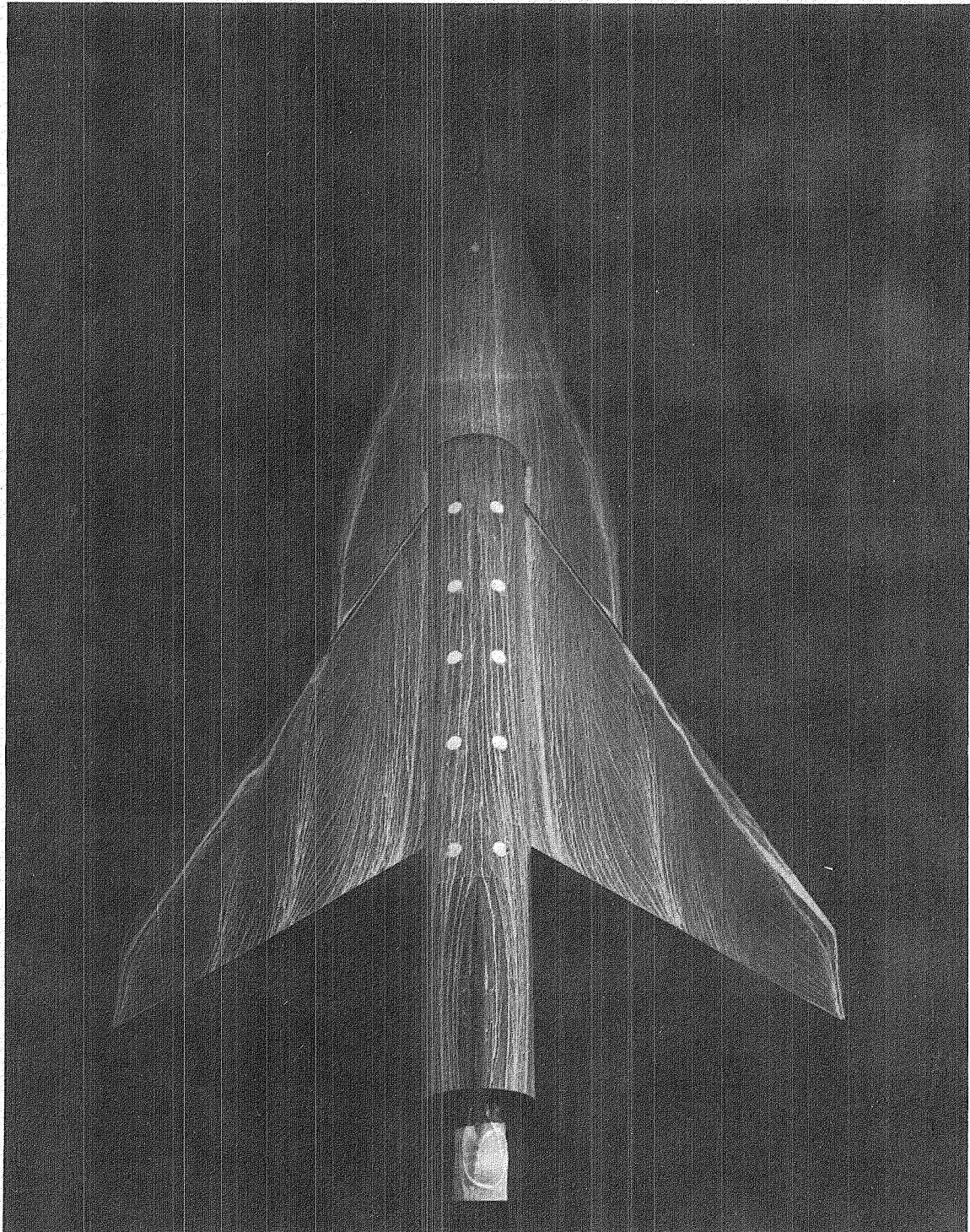
65

L-79-242

(e) $\alpha = 25^{\circ}$.
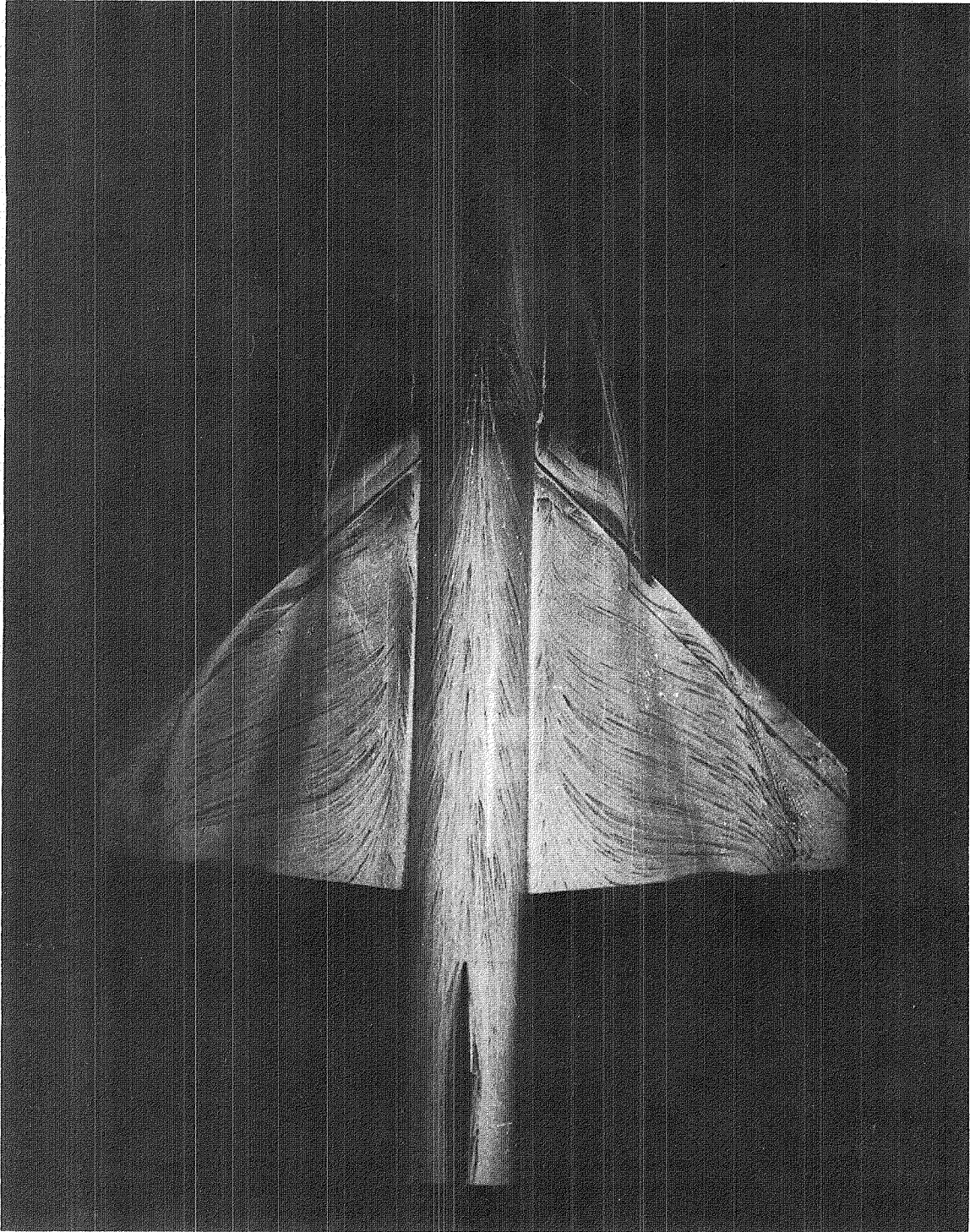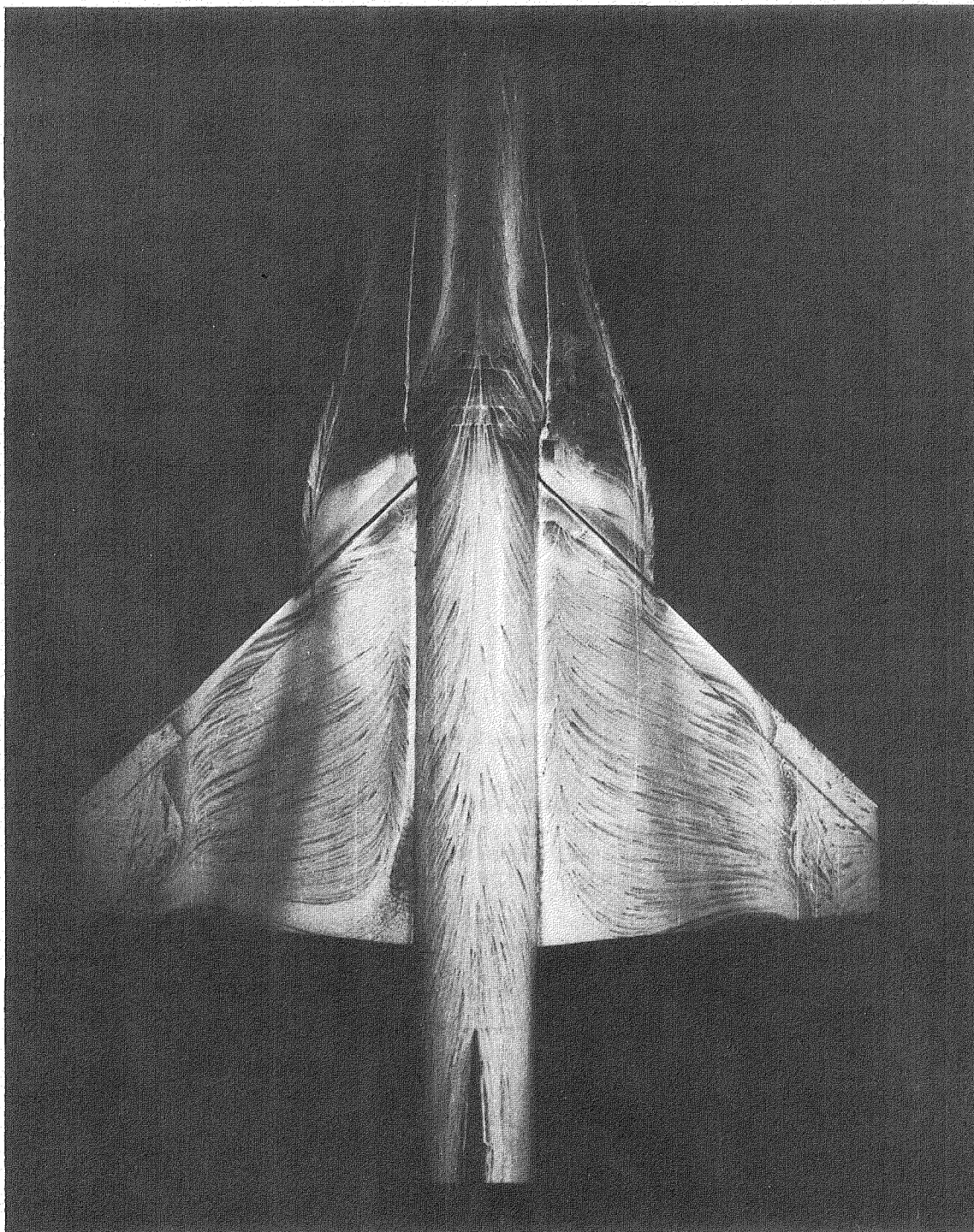
Figure 11.- Continued.

(f) $\alpha = 30^O$.
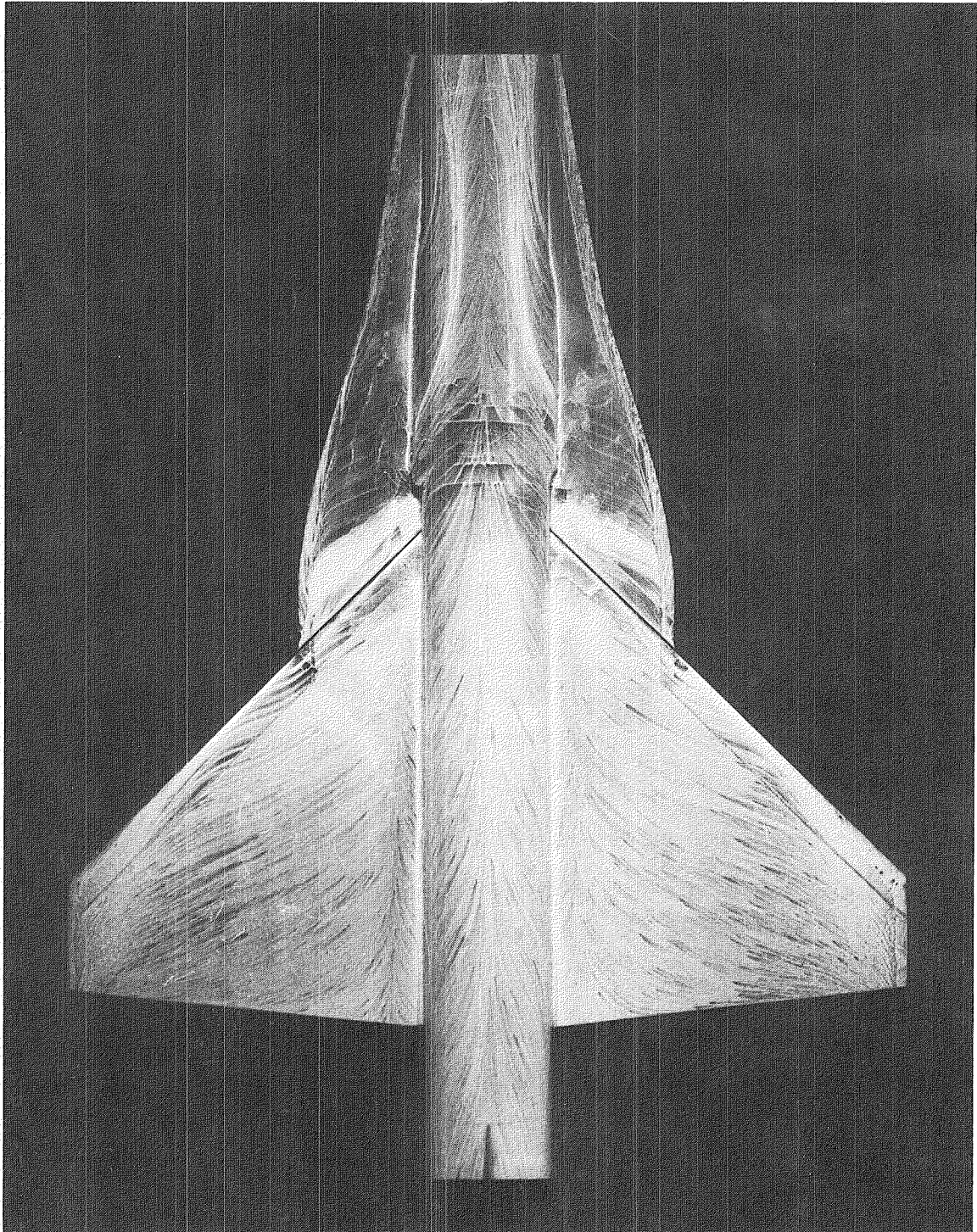
L-79-243

Figure 11.- Concluded.

L-79-244

(a) $\alpha = 5^{\circ}$.
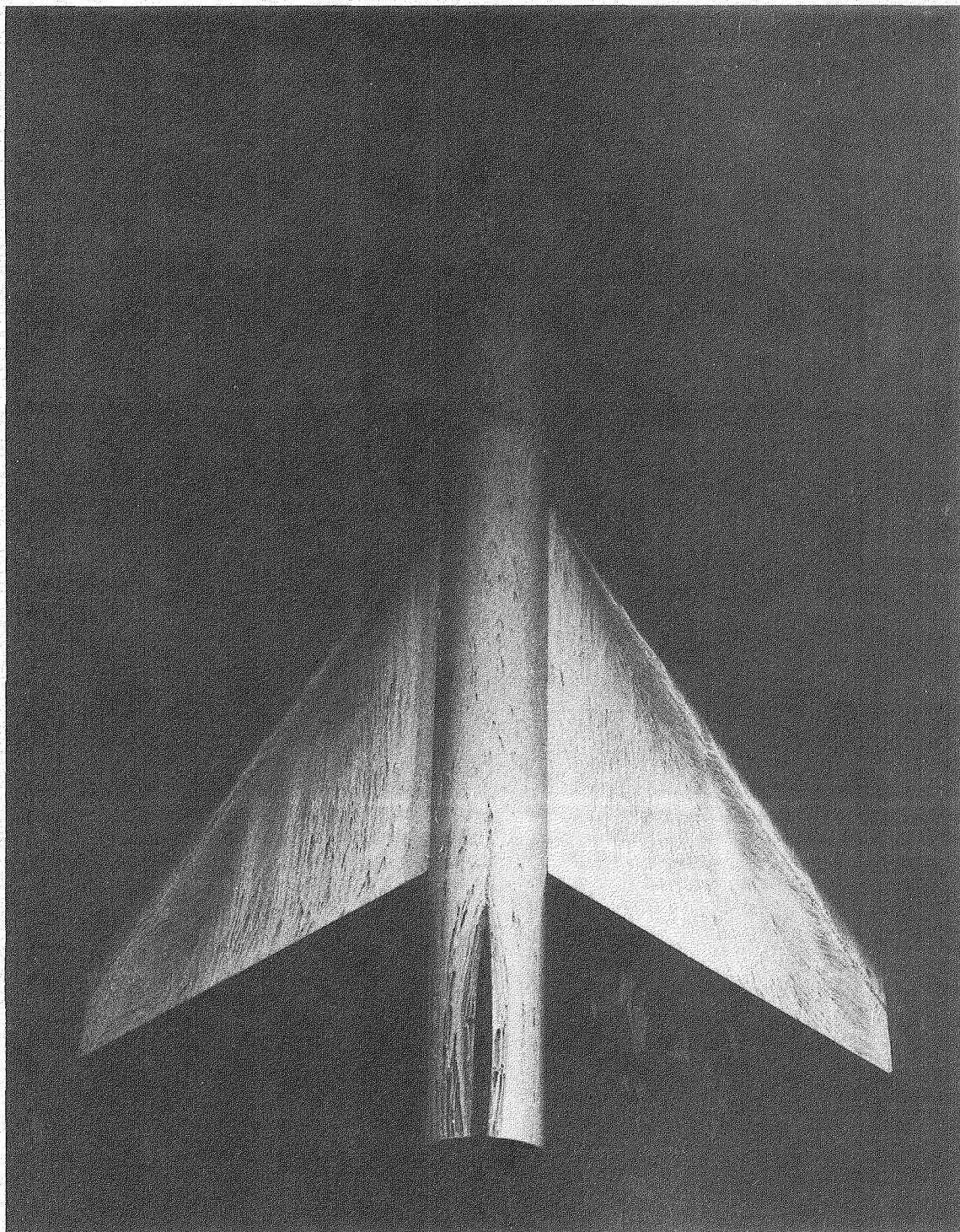
Figure 12.- Surface flow patterns for configuration 60-0, at $M_\infty = 0.3$.
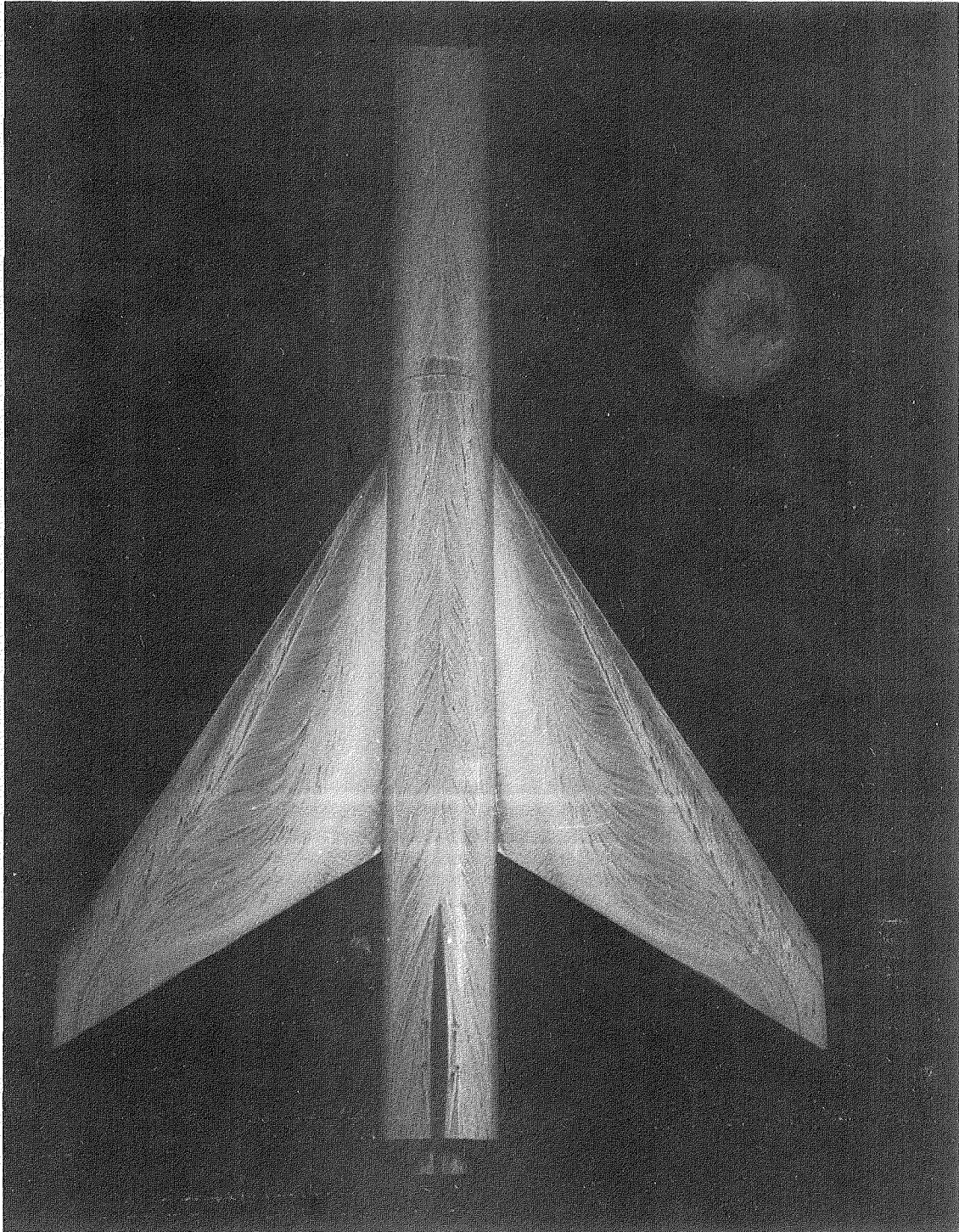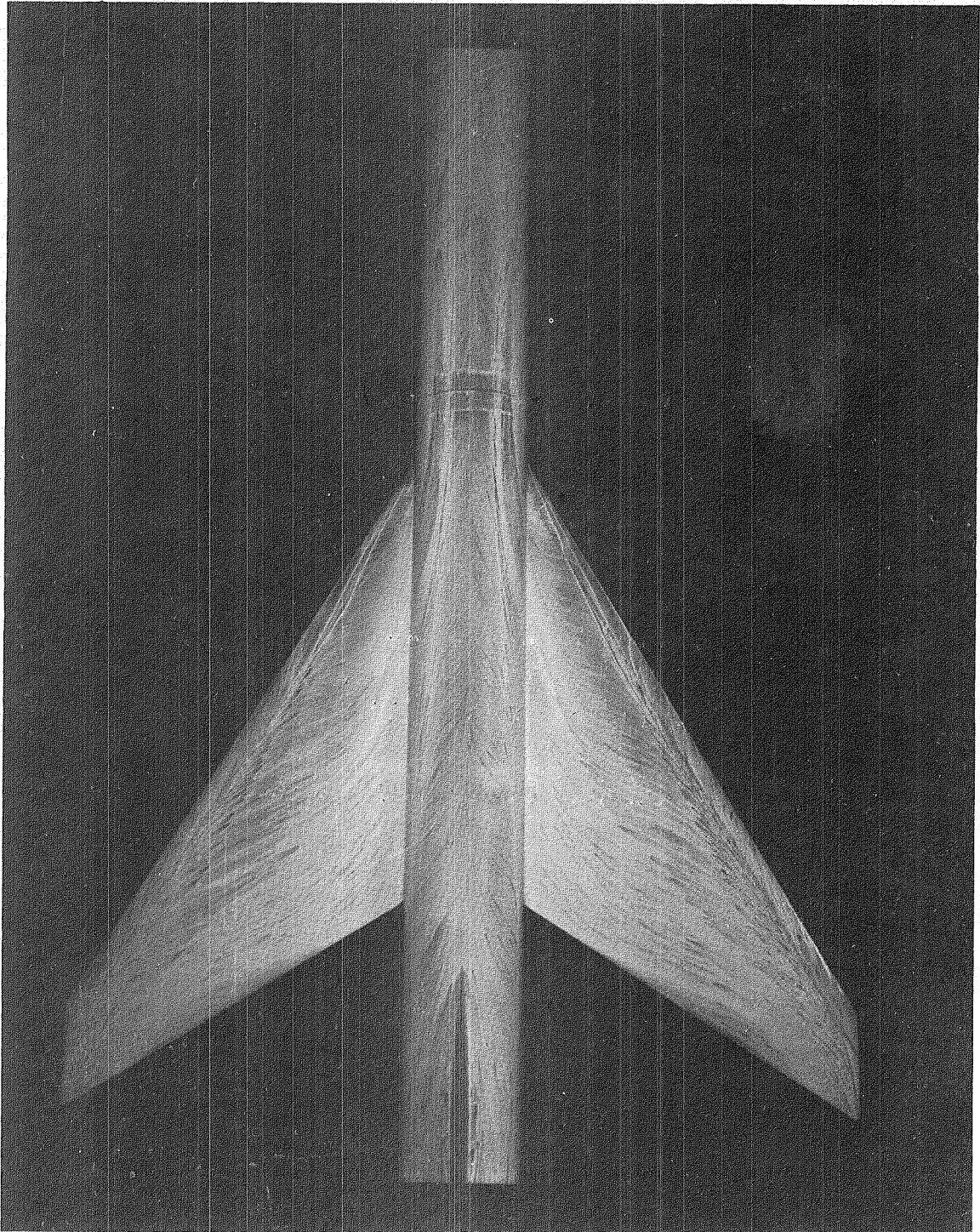
68

(b) $\alpha = 10^{\circ}$.

Figure 12.- Continued.

L-79-246

(c) $\alpha = 15^{\circ}$.

Figure 12.- Continued.

L-79-247

(d) $\alpha = 20^{\circ}$.

Figure 12.- Continued.

71

L-79-248

(e) $\alpha = 25^O$.

Figure 12.- Continued.

L-79-249

(f) $\alpha = 30^{\mathrm{o}}$.
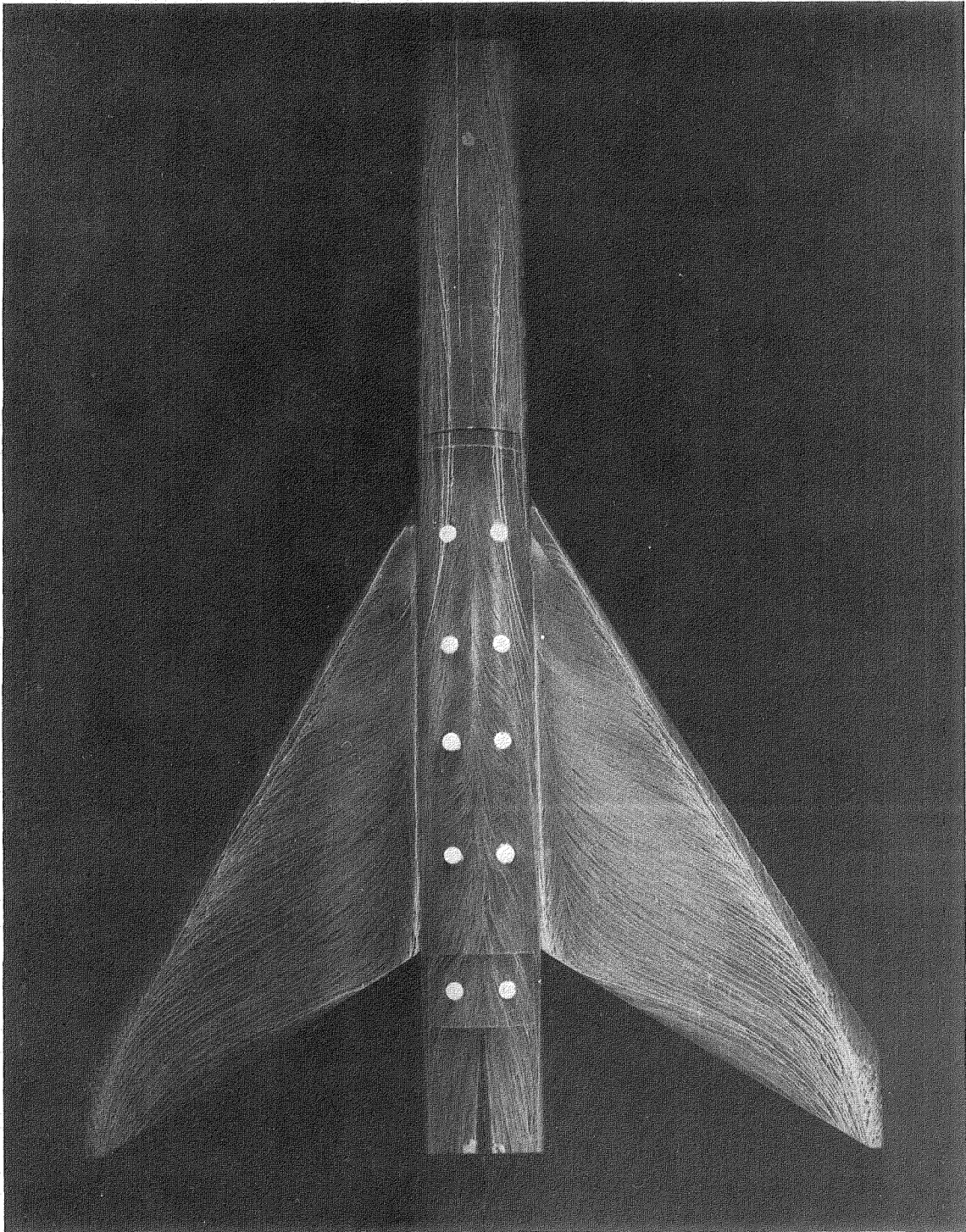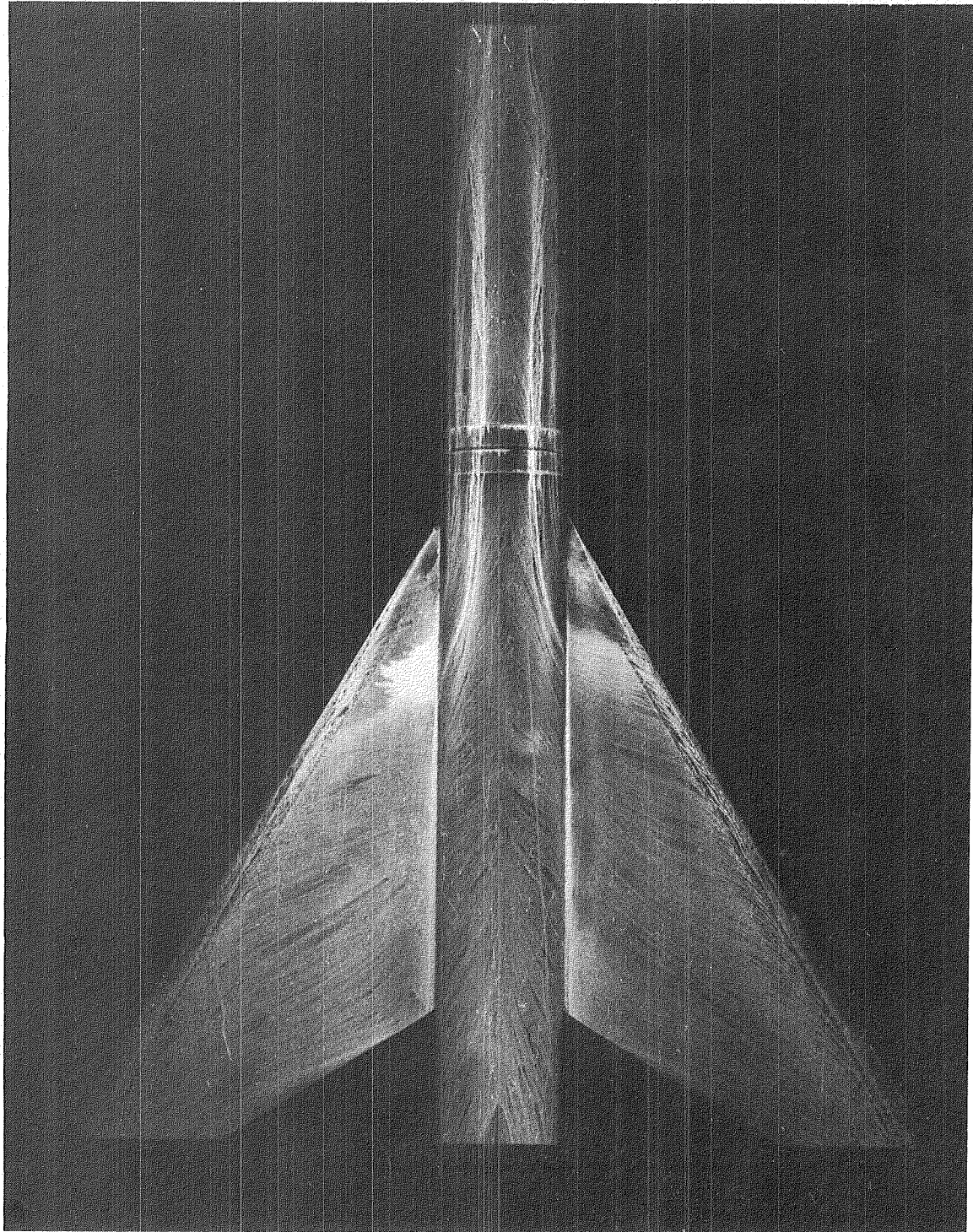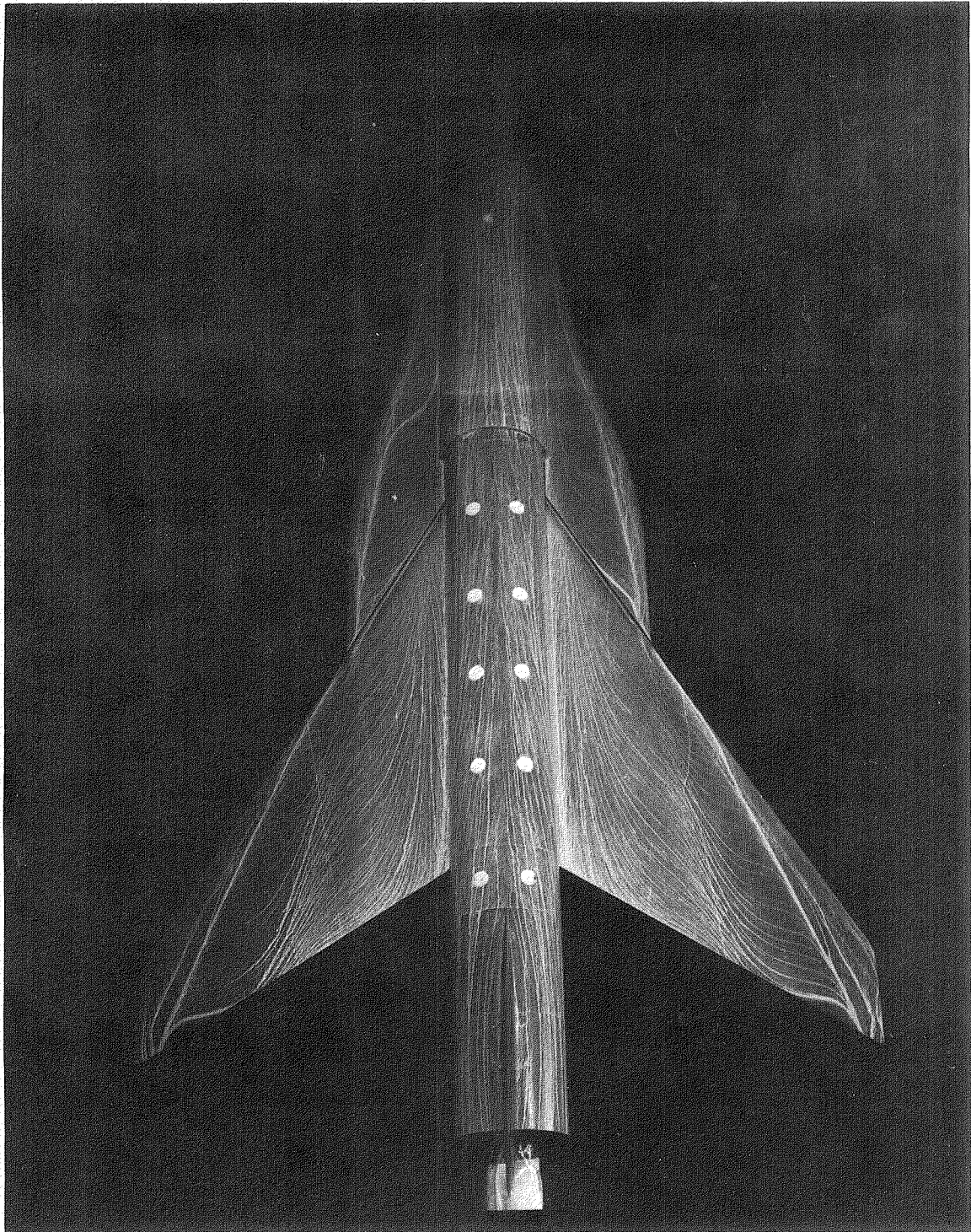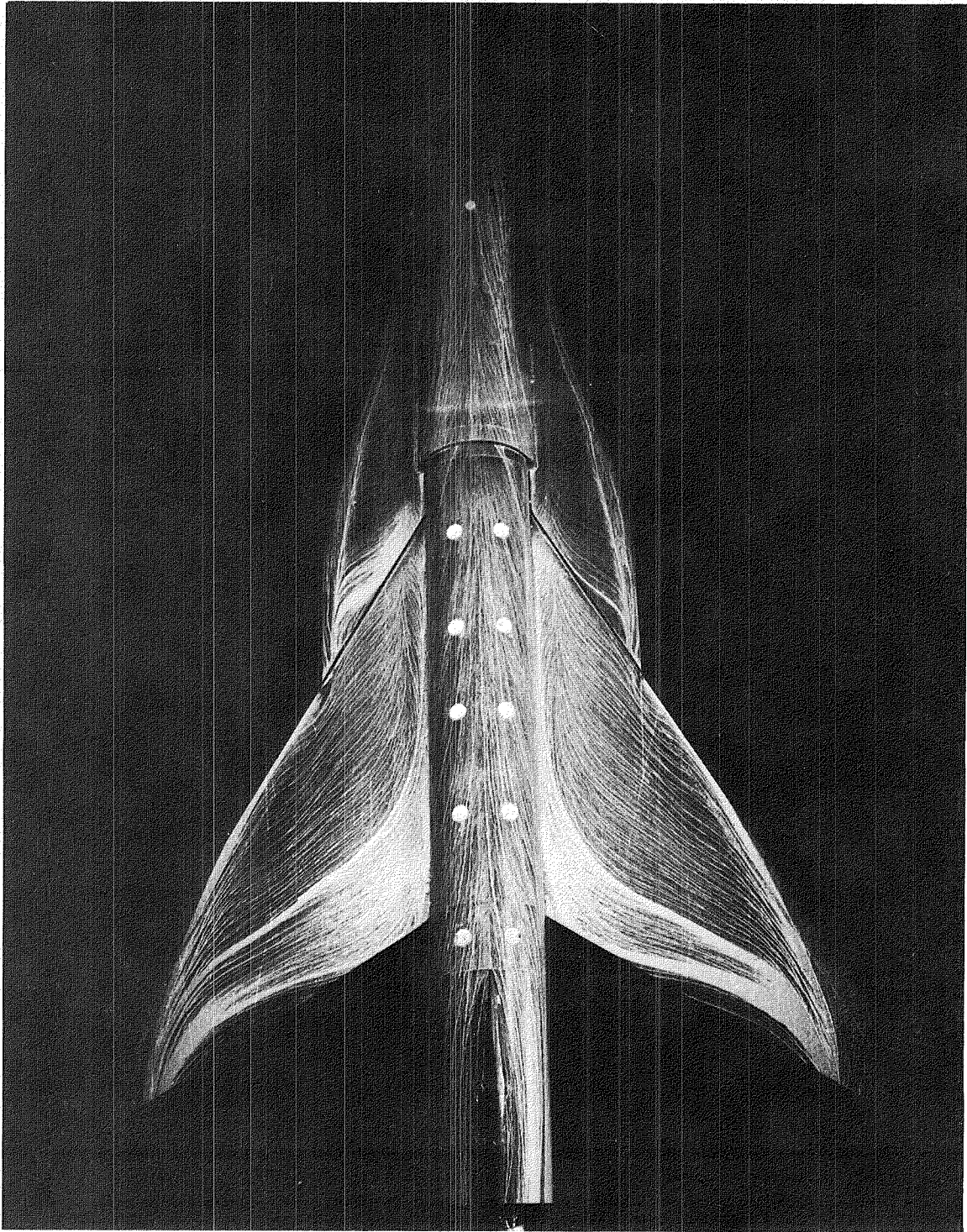
Figure 12.- Concluded.

L-79-250

(a) $\alpha = 5^{O}$.

Figure 13.- Surface flow patterns for configuration 60-1, with gap open, at $M_\infty = 0.3$.

74

(b) $\alpha = 10^\circ$.

Figure 13.- Continued.

L-79-251

L-79-252

(c) $\alpha = 15^{\circ}$.

Figure 13.- Continued.

(d) $\alpha = 20^{\circ}$.

L-79-253

Figure 13.- Concluded.

L-79-254

(a) $\alpha = 5^{\circ}$.
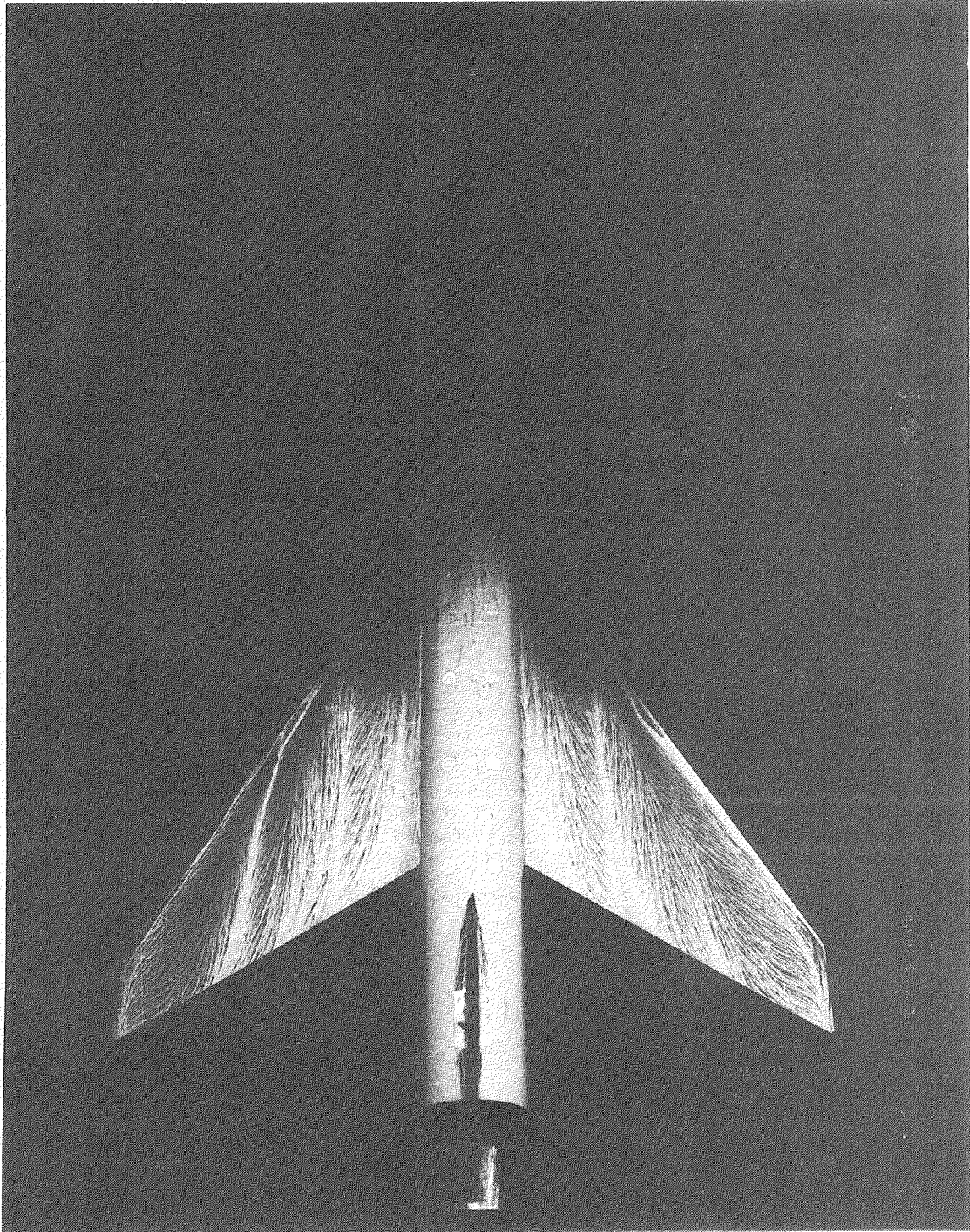
Figure 14.- Surface flow patterns for configuration 60-2, with gap open, at $M_{\infty} = 0.3$.

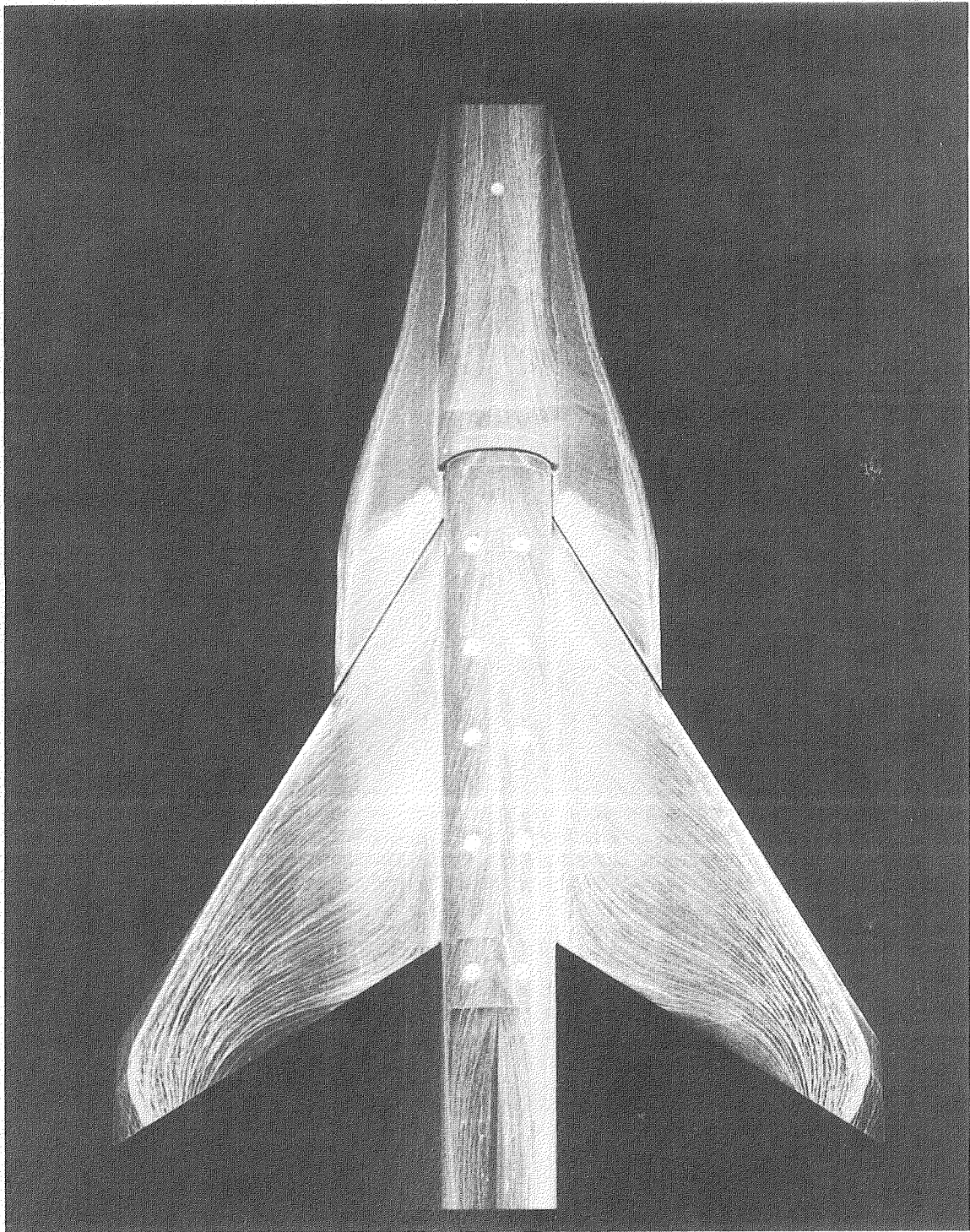78

L-79-255

(b) $\alpha = 10^{\circ}$.

Figure 14.- Continued.

L-79-256

(c) $\alpha = 15^{\circ}$.

Figure 14.- Continued.

L-79-257

(d) $\alpha = 20^O$.

Figure 14.- Continued.

L-79-258

(e) $\alpha = 25^O$.
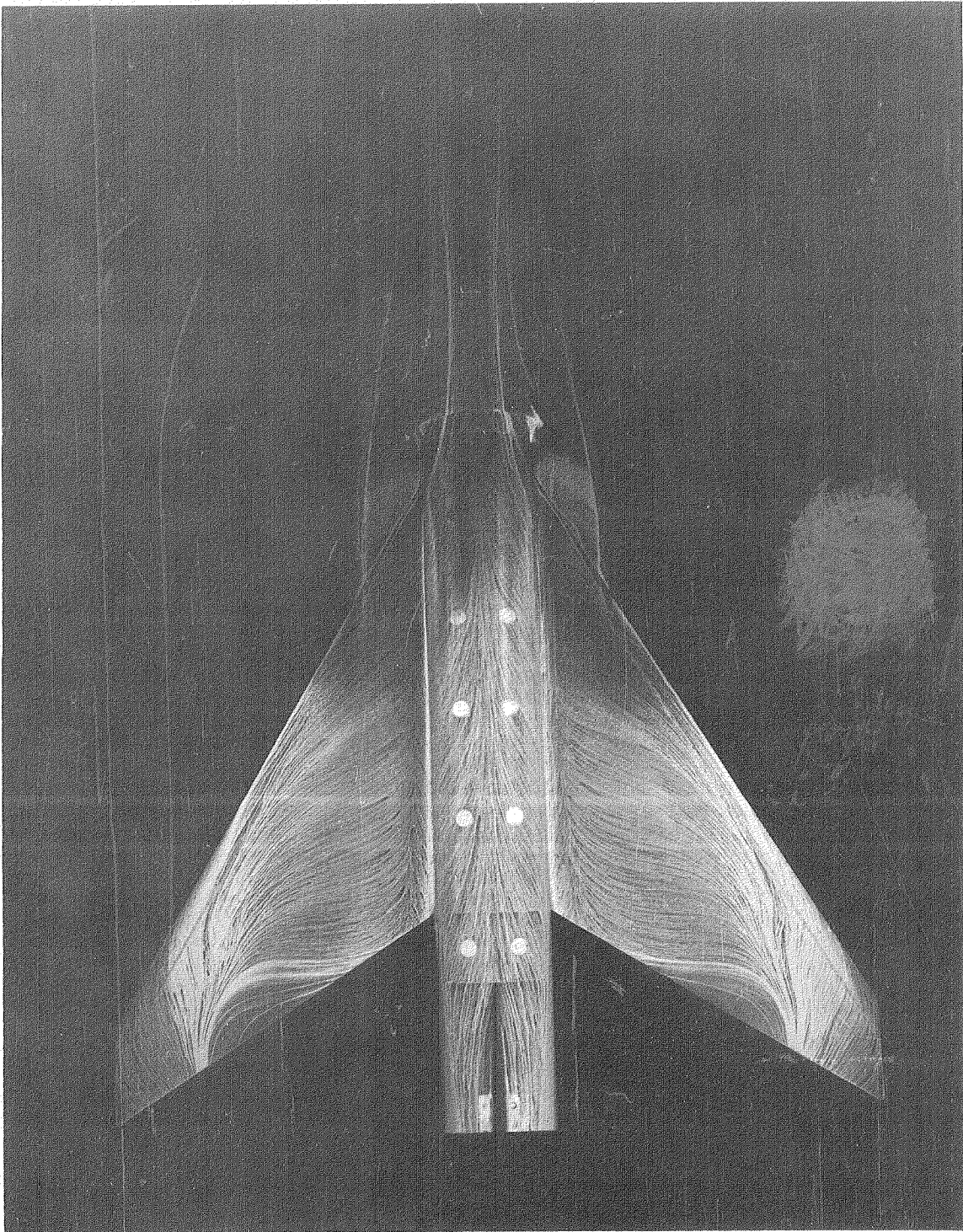
Figure 14.- Concluded.

82

L-79-259

(a) $\alpha = 5^O$.

Figure 15.- Surface flow patterns for configuration 60-3, with gap open,
at $M_\infty = 0.3$.

L-79-260

(b) $\alpha = 10^O$.
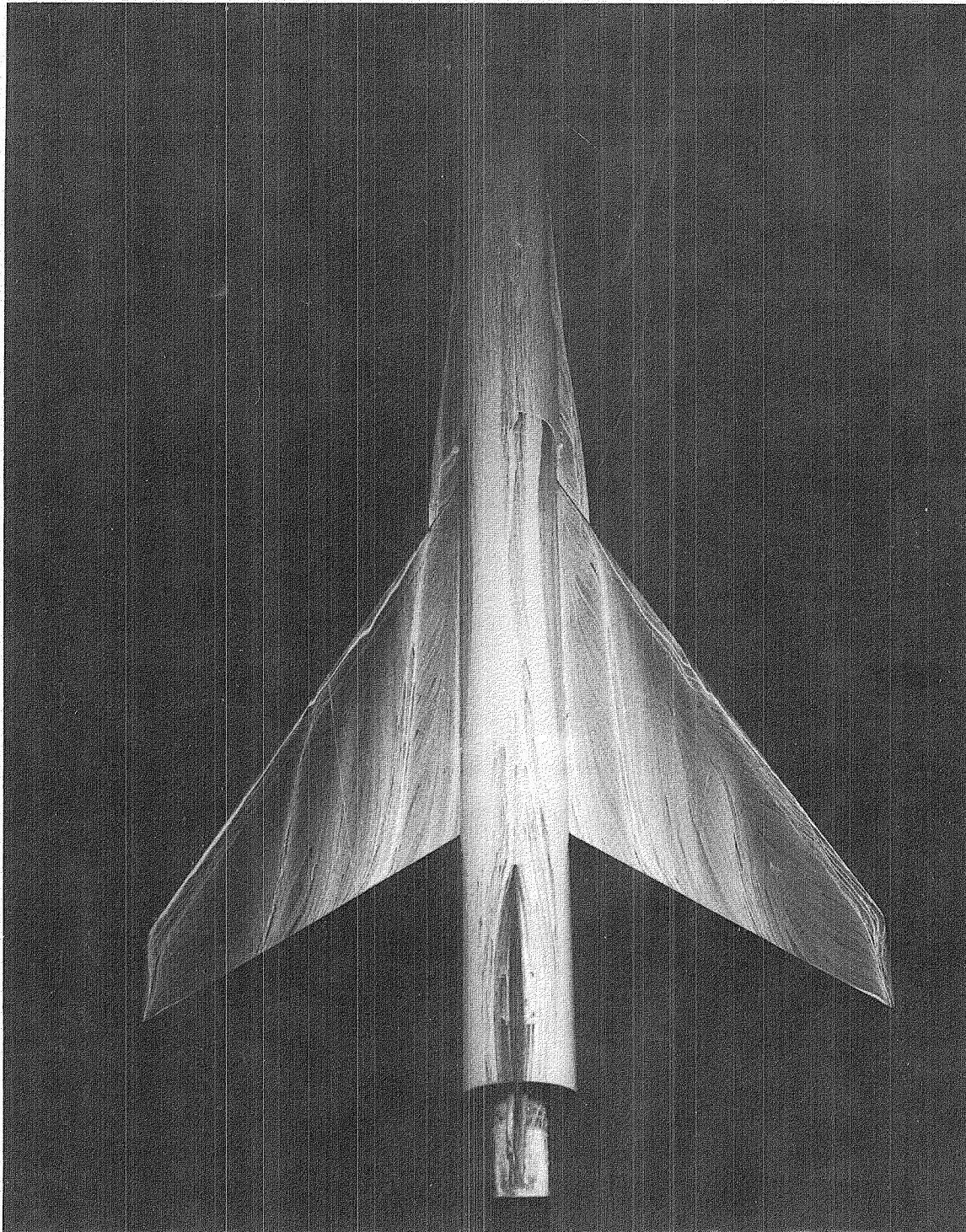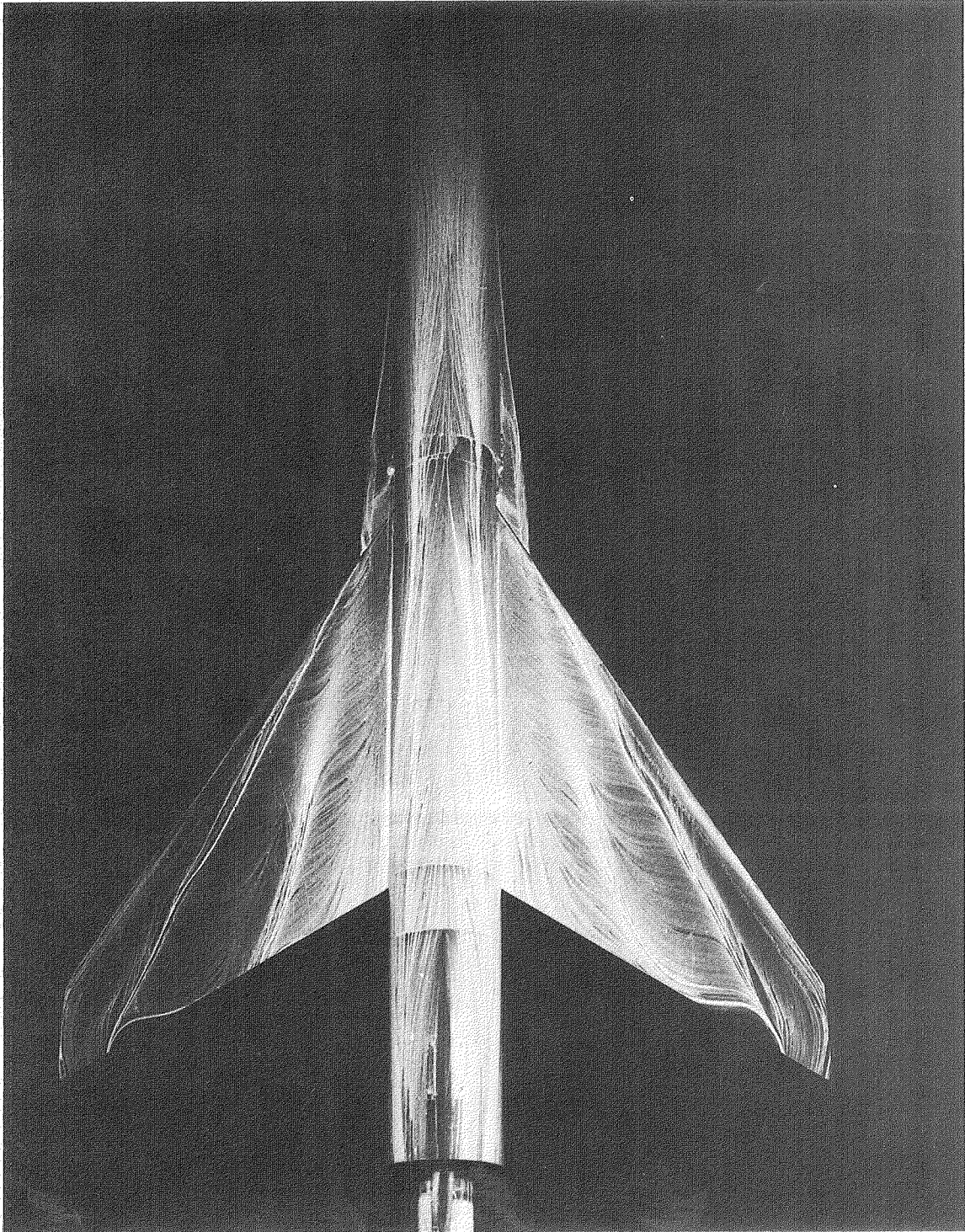
Figure 15.- Continued.

(c) $\alpha = 15^{\circ}$.

Figure 15.- Continued.

L-79-261

L-79-262

(d) $\alpha = 20^{\circ}$.
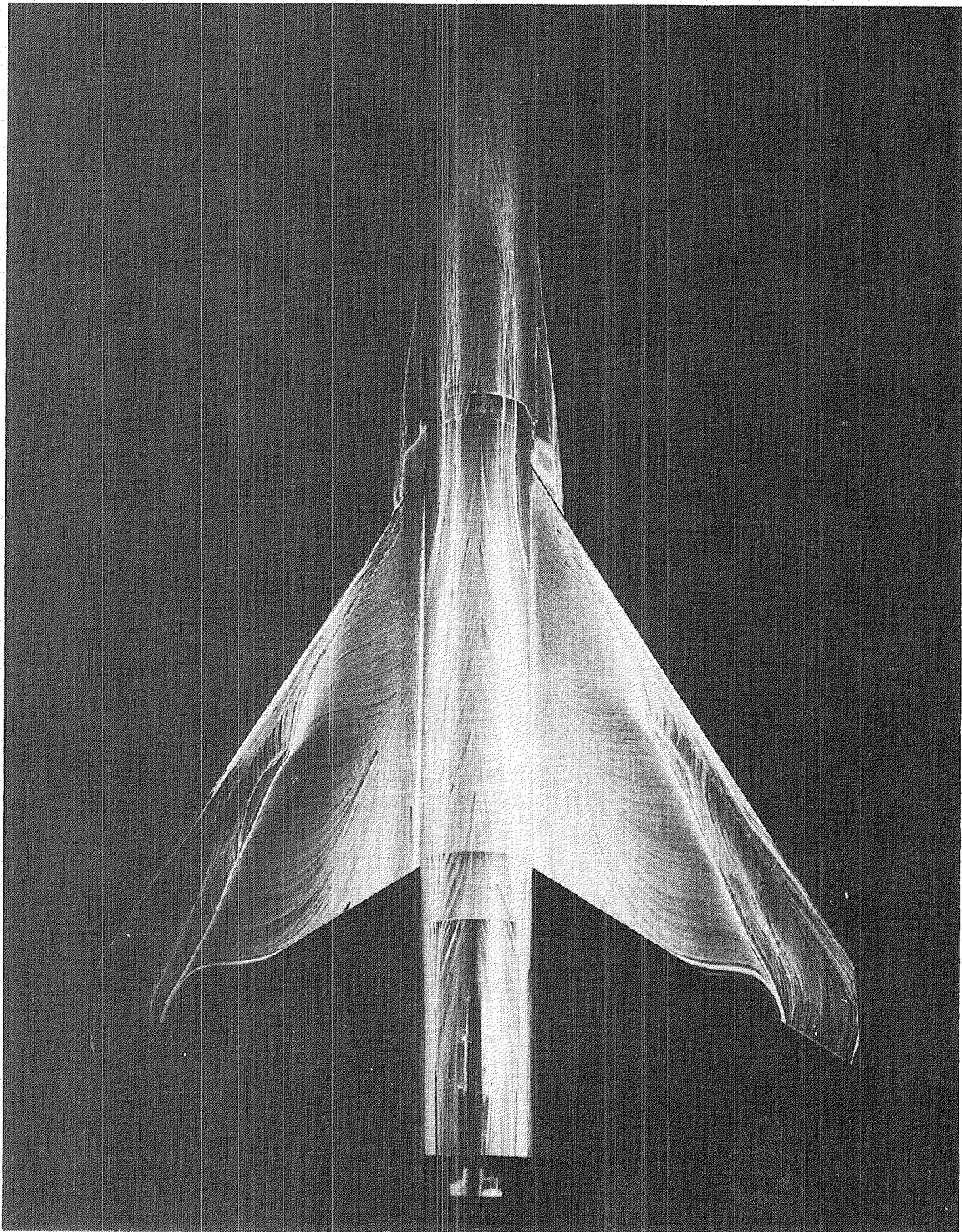
Figure 15.- Concluded.

86

(a) $\alpha = 5^o$.

Figure 16.- Surface flow patterns for configuration 60-1, with gap open,
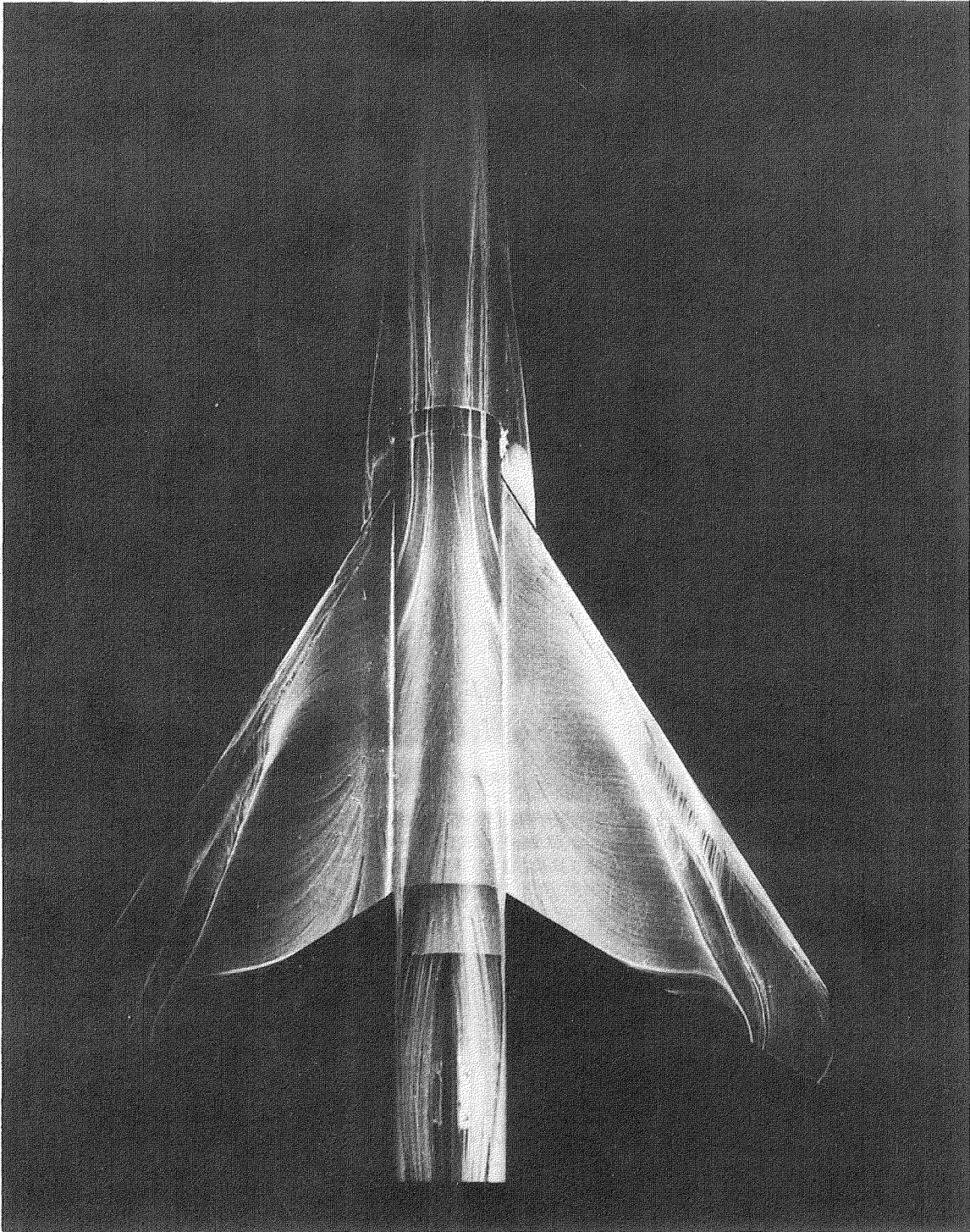at $M_\infty = 0.5$.

87

(b) $\alpha = 10^{\circ}$.

Figure 16.- Continued.

88

(c) $\alpha = 15^{\circ}$.

L-79-265

Figure 16.- Continued.

(d) $\alpha = 20^O$.

Figure 16.- Concluded.

End of Document